Ferromagnetic thin-films and nanostructures studied by spin-polarized scanning tunneling microscopy

Dissertation
zur Erlangung des Doktorgrades
des Fachbereichs Physik
der Universität Hamburg

vorgelegt von
Luis Berbil-Bautista
aus Madrid, Spanien

Hamburg
2006

Gutachter der Dissertation:
Prof. Dr. R. Wiesendanger
Prof. Dr. H. P. Oepen

Gutachter der Disputation:
Prof. Dr. R. Wiesendanger
Prof. Dr. R. L. Johnson

Datum der Disputation:
24.04.2006

Vorsitzender des Prüfungsausschusses:
Dr. A. Chudnovski

Vorsitzender des Promotionsausschusses:
Prof. Dr. G. Huber

Dekan des Fachbereichs Physik:
Prof. Dr. G. Huber

"Fue de casa en casa arrastrando dos lingotes metálicos, y todo el mundo se espantó al ver que los calderos, las pailas, las tenazas y los anafes se caían de su sitio, y las maderas crujían por la desesperación de los clavos y tornillos tratando de desenclavarse, y aun los objetos perdidos desde hacía mucho tiempo aparecían por donde más se les había buscado y se arrastraban en desbandada turbulenta detrás de los fierros mágicos de Melquíades."

Cien Años de Soledad
Gabriel García Márquez

Abstract

In this work spin-polarized scanning tunneling microscopy (SP-STM) is employed to investigate the magnetic structure of nanostructures and thin films. The high spatial and energy resolution of SP-STM allows the study of the interplay between structural, electronic, and magnetic properties. This thesis has two main subjects: SP-STM through an adsorbed layer in sulfur (S)-covered iron (Fe)-(110) islands and the magnetic structure of dysprosium (Dy) films grown on W(110).

SP-STM through an adsorbate layer is demonstrated for the first time by making use of the well-known magnetic structure of Fe(110) islands. Upon dosing with H_2S the island surface is covered with $\frac{1}{3}$ ML S leading to a c(3×1) reconstruction. The characteristic magnetic vortex structure is observable before and after dosing, even though the electronic structure of the surface is modified as shown by SP-STS.

A systematic study of the thickness-dependent morphology of Dy/W(110) films proves that the two possible stackings on the wetting layer result in perfect screw dislocations with $\vec{b} = [0001]$. Furthermore, the misfit with the wetting layer produces edge dislocations with $\vec{b} = \langle 2\bar{1}\bar{1}0 \rangle$. The investigation of the coverage-dependent domain structure reveals an increase in domain size and order with increasing film thickness. A detailed comparison of the magnetic structure and the film morphology demonstrates that these line defects are strong pinning centers for the domain walls. Furthermore, the high spatial resolution of SP-STM allows imaging of the magnetic structure at the pinning center. There, the magnetic structure resembles that of a vortex.

Inhaltsangabe

In dieser Arbeit wird die spinpolarisierte Rastertunnelmikroskopie (SP-STM) zur Untersuchung der magnetischen Struktur von Nanostrukturen und dünnen Filmen angewandt. Die hohe Orts- und Energieauflösung von SP-STM ermöglicht Studien des Wechselspiels zwischen strukturellen, elektronischen und magnetischen Eigenschaften. Diese Doktorarbeit besteht aus zwei Themen: SP-STM durch eine Adsorbatschicht auf Schwefel(S)-bedeckten Eisen(Fe)-Inseln und die magnetische Struktur von auf W(110) gewachsenen Dysprosium(Dy)-Filmen.

Erstmalig wird anhand der bekannten magnetischen Struktur von Fe(110)-Inseln die SP-STM durch eine Adsorbatschicht demonstriert. Nach Zugabe von H_2S wird eine Insel mit $\frac{1}{3}$ ML S bedeckt, entsprechend einer c(3×1) -Rekonstruktion. Die charakteristische magnetische Vortexstruktur ist sowohl vor als auch nach der Begasung beobachtbar, obwohl die elektronische Struktur der Oberfläche sich verändert, wie mittels SP-STS gezeigt wird.

Eine systematische Studie der dickenabhängigen Morphologie von Dy/W(110)-Filmen zeigt, daß die zwei möglichen Stapelfolgen auf der ersten Lage zu perfekten Schraubenversetzungen mit $\vec{b} = [0001]$ führen. Darüberhinaus entstehen durch den Misfit der ersten Lage Stufenversetzungen mit $\vec{b} = \langle 2\bar{1}\bar{1}0 \rangle$. Die Untersuchung der bedeckungsabhängigen Domänenstruktur offenbart bei steigender Filmdicke eine wachsende Domänengröße sowie zumehmende Ordnung. Ein detaillierter Vergleich der magnetischen Struktur mit der Filmmorphologie zeigt, daß die Liniendefekte starke Attraktoren für Domänenwände darstellen. Darüberhinaus erlaubt die hohe Ortsauflösung von SP-STM an den Attraktoren die Abbildung der magnetischen Struktur, die der eines Vortex gleicht.

Contents

Chapter 1

Introduction

The first computer equipped with a magnetic hard drive, the IBM System 305, was delivered 50 years ago. At that time a device with the size of a refrigerator was necessary for 5 MB of data. Ever since the capacity of magnetic hard drives has at least doubled every two years, faster even than the progress described by Moore's Law for semiconductor chips. Now, a 8 GB drive can fit in a cellular phone. In the future, it is expected that magnetic perpendicular recording combined with advanced patterning techniques will deliver data densities beyond 1 terabyte per square inch [1].

This miniaturization trend makes techniques with magnetic nanoscale resolution indispensable. SP-STM is a powerful tool to study magnetism down to the atomic scale [2, 3]. So far, however, it has been used successfully only under ultra-high vacuum (UHV) conditions. Circumventing this limitation would result in a new high resolution technique suitable for industrial application too. Furthermore, in the "nanoworld" surface properties are of great importance. "Clean" surfaces only exist under well controlled experimental conditions. Therefore, the possibility of understanding the electronic and magnetic properties on adsorbate-covered surfaces even under UHV conditions by SP-STM/STS is of fundamental importance.

The pinning of magnetic domains by atomic-scale structural defects is also of great relevance in magnetic data storage and magneto-electronic applications as it may lead to an undesirable enhancement of the switching field. Up to now magnetic domain wall pinning at the atomic scale is barely understood. Obviously, the thorough experimental investigation of pinning effects deserves a direct correlation of structural and magnetic data. Due to spatial resolution limitations past experimental studies have focussed on mesoscopic pinning sites [4–6] or on phenomenological investigations [7]. SP-STM enables the direct correlation of

structural and magnetic properties of conducting surfaces on the atomic scale.

In this thesis two model system for these problems have been studied. That is spin-polarized tunneling through a sulfur-layer on Fe(110) islands and the pinning of very narrow domain walls in Dy/W(110) films at line defects.

The thesis begins with a brief introduction to the basic theoretical aspects of STM (Chapter 2). Then a presentation of the instrumental setup and preparatory techniques is given (Chapter 3). The experimental results are divided into two sections. Chapter 4 treats SP-STM of sulfur-saturated Fe(110) islands. The chapter starts with a summary of the well-known morphological and magnetic properties of three-dimensional iron islands on Fe(110). Then a coverage dependent study of sulfur dosing confirms that the sulfur saturation is $\frac{1}{3}$ ML leading to a c(3×1) reconstruction. The core of the chapter is the SP-STM/STS results for sulfur-saturated Fe(110) islands. The characteristic magnetic vortex structure of Fe(110) islands [8] is observable before and after sulfur saturation, even though the electronic structure of the surface is modified as revealed by SP-STS. Finally, sulfur-saturated Fe(110) layers are exposed to O_2 inside the UHV system. The sulfur layer degrades resulting in a oxidized iron surface.

The morphological and magnetic properties of ferromagnetic Dy/W(110) films are discussed in Chapter 5. A very brief summary of the properties of bulk Dy opens the chapter. Then a coverage-dependent study of the film morphology is presented. It reveals that two kinds of defects are produced during the sample growth which are identified as screw and edge dislocations by atomically resolved STM images. The study of the domain structure of Dy films by SP-STM reveals pronounced domain wall pinning. The pinning sites correlate with the position of the dislocations. High resolution SP-STM images show a votex-like structure around these pinning centers. Finally, the results of the data discussed in this thesis are summarized in Chapter 6.

Chapter 2

Scanning tunneling microscopy

In the year of commemoration of the 25th anniversary of the invention of scanning tunneling microscopy (STM) by Binnig and Rohrer [9–12], it is certainly no exaggeration to say that STM has revolutionized surface science. Principally because STM allows to correlate structural, electronic, and magnetic properties even with atomic resolution.

In this chapter the general physics involved to understand the phenomenon of the tunneling process is summarized. A more detailed treatment of these topics can be found in the literature [13]. This section begins with a short summary of the experimental realization of STM measurements (Sec. 2.1). Then, the tunnel theory in one dimension is presented (Sec. 2.2). A deeper look into the tunnel theory for the STM geometry leads to the interpretation of STM topographs (Sec. 2.3). Beside the determination of the structure of surfaces, the STM allows the investigation of electronic and magnetic properties of samples. This is realized by the modes of scanning tunneling spectroscopy (STS) (Sec. 2.4) and spin-polarized (SP)-STM (Sec. 2.5) respectively, which are introduced at the end of this chapter.

2.1 Experimental realization

In STM an atomically sharp metallic tip is positioned by piezoelectric actuators above the surface of an electrically conducting sample. When the tip-sample distance is sufficiently small (typically 5-15 Å) the application of a small voltage leads to a quantum mechanical tunneling current. This tunneling current decays exponentially with increasing tip-sample distance by about a factor of 10 every Å. Therefore, the current is localized at the tip apex where tip and sample are closest. By keeping the tunneling current constant while scanning the tip laterally above the sample the surface topography can be imaged with atomic resolution [11].

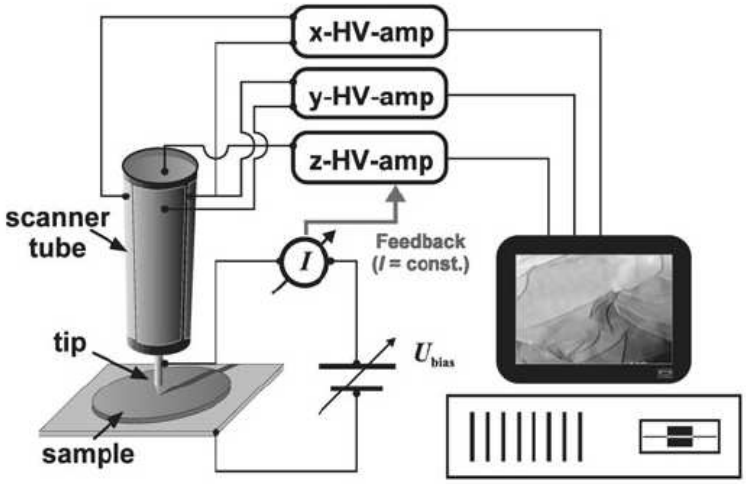

Figure 2.1: Schematic set-up of the STM taken from Ref. [14].

Fig. 2.1 shows a schematic set-up of an STM. The tip is mounted on a piezoelectric tube scanner, which is the most compact device for this application. When applying a voltage U_z to the z-electrode inside the scanner the piezoelectric material, and thus the whole tube, elongates or contracts depending on the polarity. While scanning, the tunneling current is kept constant by a feed-back loop. In this "topography mode", U_z is determined at every point and provides a measure of the surface contours.

2.2 The tunnel effect

In this section, the problem of tunneling in one dimension is discussed. In classical mechanics, an electron with energy E moving in a potential $U(z)$ can overcome a potential barrier U_0 only if $E > U_0$, otherwise it is reflected as sketched in Fig. 2.2 (a). In quantum mechanics, the electron is described by a wave function $\psi(z)$ and has a nonzero probability of tunneling through a potential barrier. This is sketched in Fig. 2.2 (b) for an electron approaching a potential barrier of height U_0 and width s. Three different regions can be distinguished:

region I:	$z < 0$,	$U(z) = 0$,	in front of the barrier,
region II:	$0 < z < s$,	$U(z) = U_0$,	inside the barrier,
region III:	$s < z$,	$U(z) = 0$,	behind the barrier.

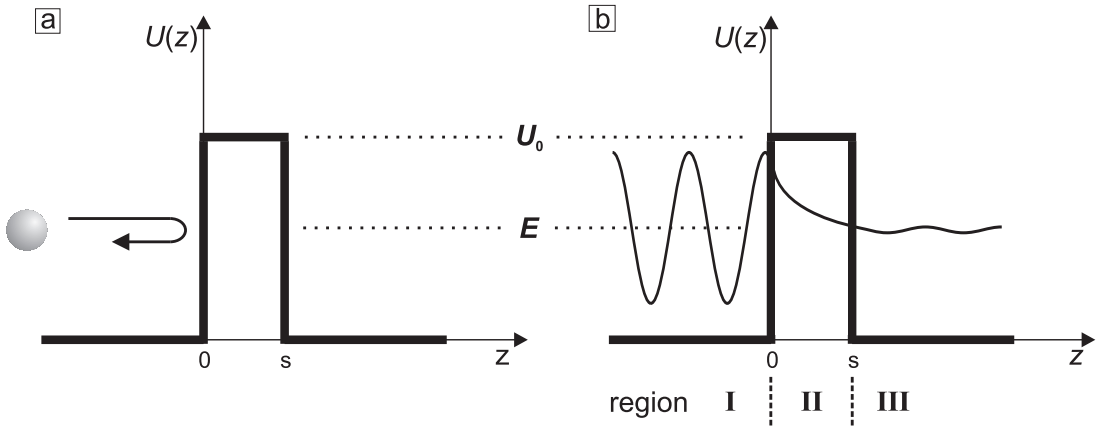

Figure 2.2: Tunnel effect in one dimension. (a) in classical mechanics an electron of energy E is reflected by a potential barrier U_0 if $E < U_0$; (b) in quantum mechanics, the probability of the electron of tunneling through a potential barrier is nonzero.

In each region the wave function of the electron satisfies the time-independent Schrödinger equation,

$$\left(-\frac{\hbar^2}{2m}\frac{\mathrm{d}^2}{\mathrm{d}z^2} + U(z)\right)\ \psi(z) \ = \ E\,\psi(z), \tag{2.1}$$

where m is the electron mass and $\hbar$ is Planck's constant over 2π. The solutions for the different regions are:

$$\begin{aligned} &\text{region I:} && \psi_1 = e^{ikz} + Ae^{-ikz}\,, \\ &\text{region II:} && \psi_2 = Be^{-\kappa z} + Ce^{\kappa z}\,, \\ &\text{region III:} && \psi_3 = De^{ikz}\,, \end{aligned}$$

where $k^2 = 2mE/\hbar^2$ and $\kappa^2 = 2m(U_0 - E)/\hbar^2$.

The incident current density j_i and the transmitted current density j_t can be described by

$$j_\mathrm{i} = \frac{\hbar k}{m} \tag{2.2}$$

$$j_\mathrm{t} = \frac{-\mathrm{i}\,\hbar}{2m}\left(\psi_3^*(z)\frac{\mathrm{d}\,\psi_3(z)}{\mathrm{d}\,z} - \psi_3(z)\frac{\mathrm{d}\,\psi_3^*(z)}{\mathrm{d}\,z}\right) = \frac{\hbar k}{m}|D|^2 \tag{2.3}$$

and the transmission coefficient T is given by the transmitted current density over the incident current density:

$$T = \frac{j_\mathrm{t}}{j_\mathrm{i}} = |D|^2\,. \tag{2.4}$$

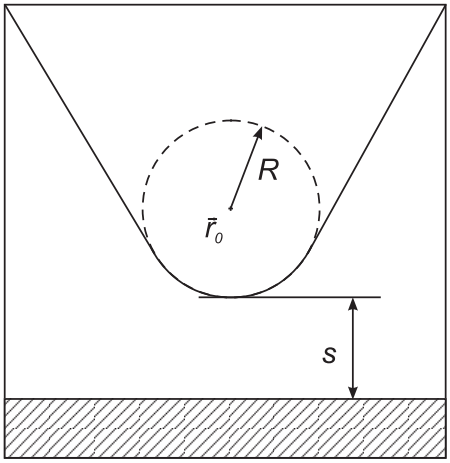

Figure 2.3: Schematic picture of the tunneling geometry in the Tersoff-Hamann model: s is the tip-sample distance, R the effective tip radius, and $\vec{r}_0$ the center of curvature of the tip.

The overall wave function is obtained by using the boundary conditions of the *wave-matching method*, i.e. the continuity of the wave function and its derivative at the discontinuities of the potential. The transmission coefficient is then

$$T = \frac{j_\mathrm{t}}{j_\mathrm{i}} = |D|^2 = \frac{1}{1 + (k^2+\kappa^2)^2/(4k^2\kappa^2)\sinh(\kappa s)}\,. \tag{2.5}$$

This is the exact expression for the transmission coefficient. In the limit of a strongly attenuating barrier ($\kappa s \gg 1$) the transmission coefficient can be approximated by

$$T \approx \frac{16k^2\kappa^2}{(k^2+\kappa^2)^2} \cdot \mathrm{e}^{-2\kappa s}. \tag{2.6}$$

The transmission coefficient is dominated by the exponential factor $\mathrm{e}^{-2\kappa s}$. Therefore, tunneling in this simple model depends exponentially on the barrier width s and on the square root of the effective barrier height $U_0 - E$. This explains the high sensitivity of the tunneling current to the tip-sample distance in STM.

2.3 Surface topography

Although the simple model introduced in Sec. 2.2 contains the inherent exponential dependence of the tunneling current on the tip-sample distance, it fails to explain any dependence of the current to the electronic structure of tip or sample.

Bardeen used fist-order time-dependent perturbation theory to explain the electron tunneling between two weakly coupled electrodes [15]. In order to appropriately describe the tunneling process in STM, Tersoff and Hamann applied Bardeen´s formalism to the STM geometry [16, 17]. They approximated the tip by

a local spherical symmetry and allowed only s-type wave functions to contribute to the tunnel matrix elements. The schematic picture of the tunneling geometry in the Tersoff-Hamann model is shown in Fig. 2.3 where R is the effective tip radius, $\vec{r}_0$ is the center of curvature of the tip, and s is the tip-sample distance. In the limit of low temperature and low bias voltage U ($\sim$ 10 meV for metals), the current can be described by

$$I \propto U \cdot n_{\mathrm{t}}(E_{\mathrm{F}}) \cdot \mathrm{e}^{2\kappa R} \cdot \sum_{\nu} |\psi_{\nu}(\vec{r}_0)|^2 \cdot \delta(E_{\nu} - E_{\mathrm{F}}) \tag{2.7}$$

where E_{F} is the Fermi energy and $n_{\mathrm{t}}(E_{\mathrm{F}})$ is the density of states at the Fermi level of the tip. The decay rate κ is proportional to the effective local potential barrier height $\overline{\phi}$, which is to a good approximation, equal to the average of the tip and sample work functions. The quantity

$$n_{\mathrm{s}} = \sum_{\nu} |\psi_{\nu}(\vec{r}_0)|^2 \cdot \delta(E_{\nu} - E_{\mathrm{F}}) \tag{2.8}$$

can be identified with the surface local density of states (LDOS) at the Fermi level, evaluated at $\vec{r}_0$. Since the tip wave functions ψ_{ν} decay exponentially into the vacuum one can derive that the current depends exponentially on the tip-sample distance:

$$I \propto \mathrm{e}^{-2\kappa s} \,. \tag{2.9}$$

In the framework of the discussed approximations the interpretation of topographic STM data is as follows: The area $z(x, y)|_{I=\mathrm{const}}$ is, according to Eq. 2.7, a trace of constant LDOS at the Fermi level of the surface at the location of the tip. For chemically homogeneous samples the LDOS follows the topography to a good approximation and the constant current images can be interpreted as the topography of the surface.

2.4 Electronic properties

Beside the capability of obtaining morphological information of a surface in the topography mode, the STM allows to gain information about the electronic properties of a sample.

In the previous section the tunneling process was described by the Tersoff-Hamann model in the limit of small bias voltage U. At larger bias voltage this model can be extended to a tunneling current weighted over a range of energies

$$I \propto \int_0^{eU} n_{\mathrm{s}}(E) \cdot n_{\mathrm{t}}(E, eU) \cdot \mathsf{T}(E, eU)\, \mathrm{d}E \tag{2.10}$$

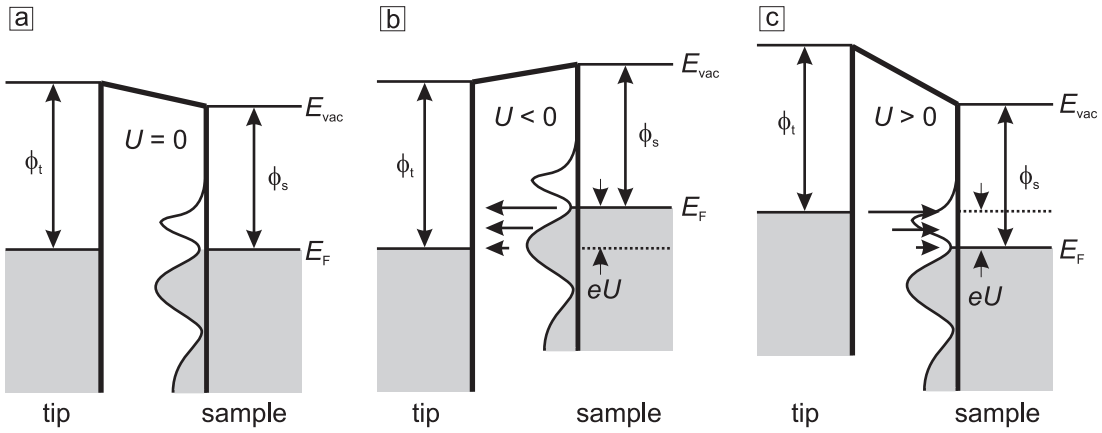

Figure 2.4: System of tip and sample in tunnel contact. (a) Equilibrium, no net tunneling current. (b) Negative sample bias, net tunneling current from sample to tip. (c) Positive sample bias, net tunneling current from tip to sample. The energy-dependent sample density of states is sketched by the curve inside the barrier.

with a transmission factor

$$T(E, eU) = \exp\left[-s \cdot \sqrt{\frac{4m}{\hbar^2}(\phi_\mathrm{t} + \phi_\mathrm{s} + eU - 2E)}\right], \tag{2.11}$$

where ϕ_t and ϕ_s are the work functions of tip and sample, respectively.

Fig. 2.4 shows a schematic representation of the tunneling process as introduced in Eq. 2.10. The left and right electrodes represent the tip and sample, respectively. The occupied states are indicated by the shaded region below the Fermi level. In the equilibrium state ($U = 0$) in Fig. 2.4 (a) the Fermi levels and the net tunneling current is zero. Applying a bias voltage U leads to a shift of the Fermi levels by $|eU|$. At negative sample bias voltage U electrons from the sample in the energy interval from $E_\mathrm{F} - eU$ to E_F tunnel into unoccupied states of the tip Fig. 2.4 (b). For positive U the situation is reversed and electrons tunnel from occupied tip states into unoccupied states of the sample Fig. 2.4 (c).

The differentiation of the tunneling current in Eq. 2.10 with the approximation that n_t is constant results in

$$\frac{\mathrm{d}I}{\mathrm{d}U}(U) \propto n_\mathrm{t}(0) \cdot n_\mathrm{s}(eU) \cdot T(E, eU) + \int_0^{eU} n_\mathrm{s}(E) \cdot n_\mathrm{t}(eU - E) \cdot \frac{\mathrm{d}\,T(E, eU)}{\mathrm{d}U} \mathrm{d}E. \tag{2.12}$$

Often the second term of Eq. 2.12 can be neglected. Then, assuming T varies

monotonically with U, the differential conductance $\mathrm{d}I/\mathrm{d}U$ is a good measure of n_s at an energy equal to eU [18].

Experimentally $\mathrm{d}I/\mathrm{d}U$ is measured by stabilizing the tip above the surface at I_stab and U_stab. Then the feedback loop is switched off, therefore the tip-sample distance is held constant. While the voltage is ramped from the initial voltage to a final voltage, the tunneling current is measured. The $\mathrm{d}I/\mathrm{d}U(U)$ can be obtained by numerical differentiation of $I(U)$ curves. However, in this work the lock-in technique was used. This technique improves significantly the signal-to-noise ratio by adding a small modulation voltage at a reference frequency to the bias voltage, and then amplifying the signal at the reference frequency.

To investigate the electronic structure of a sample with lateral resolution, full $\mathrm{d}I/\mathrm{d}U$ spectroscopy measurements are performed at different positions of the sample. This can be done at each pixel of a corresponding topographic image to obtain a spatially resolved energy-dependent $\mathrm{d}I/\mathrm{d}U$ signal map. This allows a direct correlation of topographic $z(x, y)$ and spectroscopic properties $\mathrm{d}I/\mathrm{d}U(x, y, U)$ of the sample.

A time-saving alternative to full $\mathrm{d}I/\mathrm{d}U$ spectroscopy is the acquisition of $\mathrm{d}I/\mathrm{d}U$-maps. There, the interest is focused on one particular energy. While $\mathrm{d}I/\mathrm{d}U$-spectra are acquired with an open feedback loop at the given stabilization parameters, for the measurement of $\mathrm{d}I/\mathrm{d}U$-maps the feedback loop is not switched off at any time but simultaneously to the topographic measurement a lock-in technique derives the $\mathrm{d}I/\mathrm{d}U$-signal at the corresponding voltage. Due to the reduction of measurement parameters, i.e. without energy resolution, the spatial resolution can be enhanced and measurements in even shorter time can be performed without the loss of correlation between topography $z(x, y)$ and differential tunneling conductance $\mathrm{d}I/\mathrm{d}U(x, y)$ at a given energy.

2.5 Spin-polarized STM

In the previous sections the spin of the tunneling electrons was neglected. This section deals with the dependence of the tunneling current on the spin. The problem of tunneling between two spin-polarized electrodes was treated theoretically by Slonczewski [19]. In the limit of a vanishing bias voltage U and under the assumption of a free-electron behaviour of the conduction electrons, the spin-polarized tunneling current I_SP between two spin-polarized electrodes can be described by

$$I_\mathrm{SP}(U_0) = I_0[1 + P_1 \cdot P_2 \cdot \cos(\vec{m}_1, \vec{m}_1)] \tag{2.13}$$

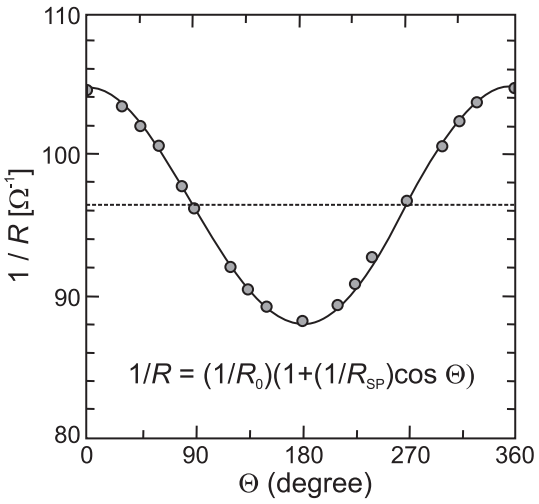

Figure 2.5: Demonstration of the $\cos\Theta$-dependence of the tunneling current in a Fe-Al_2O_3-Fe junction. (Taken from Ref. [20])

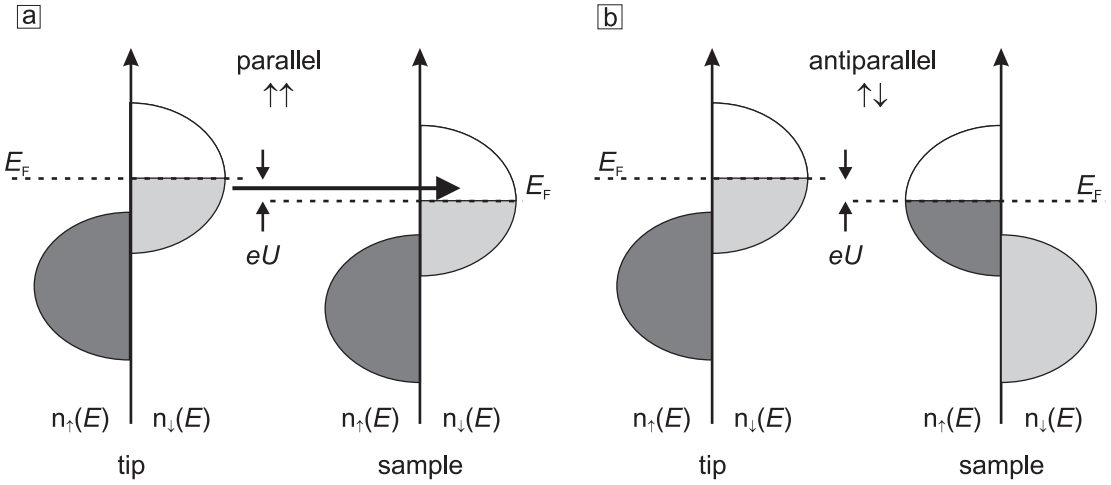

Figure 2.6: Spin-polarized tunneling with spin conservation at positive sample bias. (a) Electrons from the tip with spin $\downarrow$ can tunnel into unoccupied states of the sample with spin $\downarrow$, due to a large number of states the tunnel probability is high. (b) Reversed sample spin polarization with no unoccupied states $\downarrow$.

where I_0 is the spin-averaged current. P is the spin polarisation and $\vec{m}$ is the magnetisation of the electrodes. Fig. 2.5 shows the dependence of the tunneling conductance $1/R$ of a planar Fe-Al_2O_3-Fe junction on the angle Θ between the magnetization of both electrodes [20]. The $\cos\Theta$-behavior is in agreement with the theory in Ref. [19].

The basic assumption in electron tunneling between spin-polarized electrodes is the spin conservation. Considering this assumption, Fig. 2.6 schematically represents the spin-polarized tunneling on the basis of a spin-split density of states

in the case of perfect parallel (a) and antiparallel (b) magnetized electrodes. For positive bias voltage, an electron with spin $\downarrow$ only can tunnel in an unoccupied sample state with spin $\downarrow$ as indicated by the arrow in Fig. 2.6. Since the tunneling probability depends on the number of electronic states available the spin-polarized current will be larger in the example of Fig. 2.6 (a) than in Fig. 2.6 (b).

Furthermore, the Tersoff-Hamann theory has been generalized by Wortmann *et al.* [21] for the case of STM imaging with a spin-polarized tip:

$$\frac{\mathrm{d}I}{\mathrm{d}U}(\vec{r}_\mathrm{t}, U) \propto \underbrace{n_\mathrm{t} \cdot n_\mathrm{s}(\vec{r}_\mathrm{t}, E_\mathrm{F} + \mathrm{e}U)}_{\text{spin-averaged}} + \underbrace{\vec{m}_\mathrm{t} \cdot \vec{m}_\mathrm{s}(\vec{r}_\mathrm{t}, E_\mathrm{F} + \mathrm{e}U)}_{\text{spin-dependent}}, \tag{2.14}$$

where $\vec{m}_\mathrm{t}$ and $\vec{m}_\mathrm{s}$ are the vectors of the energy-integrated local DOS magnetization of tip and sample, respectively. To derive Eq. 2.14 it has been assumed the spin-up and spin-down tip density of states are constant in energy which, however, might not be fulfilled in a general case (see Sec. 5.5.5). In this framework, the differential conductance $\mathrm{d}I/\mathrm{d}U$ can be divided in a spin-averaged part and a spin-dependent part. In a similar way to the electronic $\mathrm{d}I/\mathrm{d}U$-map, a magnetic $\mathrm{d}I/\mathrm{d}U$-map of the sample can be acquired by choosing the appropriate bias voltage.

Chapter 3

Instrumental setup

The aim of this work is the study of clean and well-ordered magnetic films and magnetic nanostructures by means of SP-STM/STS. Therefore, the instrumental setup should ensure the cleanliness and repeatability of the experiments. For this reason the studies are performed in a multichamber ultra-high vacuum (UHV) system that is introduced in the present chapter. This chapter also includes a description of the preparation of magnetic tip and samples.

3.1 The UHV system

In order to prepare and study clean and well-defined metallic thin films and nanostructures, it is necessary to work under UHV conditions (defined as a pressure below 10^{-9} Torr). Otherwise, surfaces are rapidly contaminated by adsorbates from the residual gas. For example, one atomic layer will be adsorbed on a clean surface, with a sticking coefficient of one, within one second at a pressure of 10^{-6} mbar [22].

The experiments are performed in a UHV system based on a commercial system [23] shown in Fig. 3.1. The system consists of three chambers separated by UHV valves and connected by linear manipulators: (i) the analysis chamber where SP-STM/STS, low energy electron diffraction (LEED), and Auger electron spectroscopy (AES) experiments are performed and the Dy films are prepared, (ii) the preparation chamber where tips and Fe samples are prepared, and (iii) a small satellite chamber dedicated to H_2S adsorption. Each chamber is equipped with an ion-pump. The base pressure in the analysis and preparation chamber is $p < 1 \cdot 10^{-10}$ mbar, and in the low 10^{-9} mbar range for the H_2S dosing chamber. The preparation chamber is connected to a fast-entry lock that allows tip and sample transfer into the UHV system from outside the chamber within several

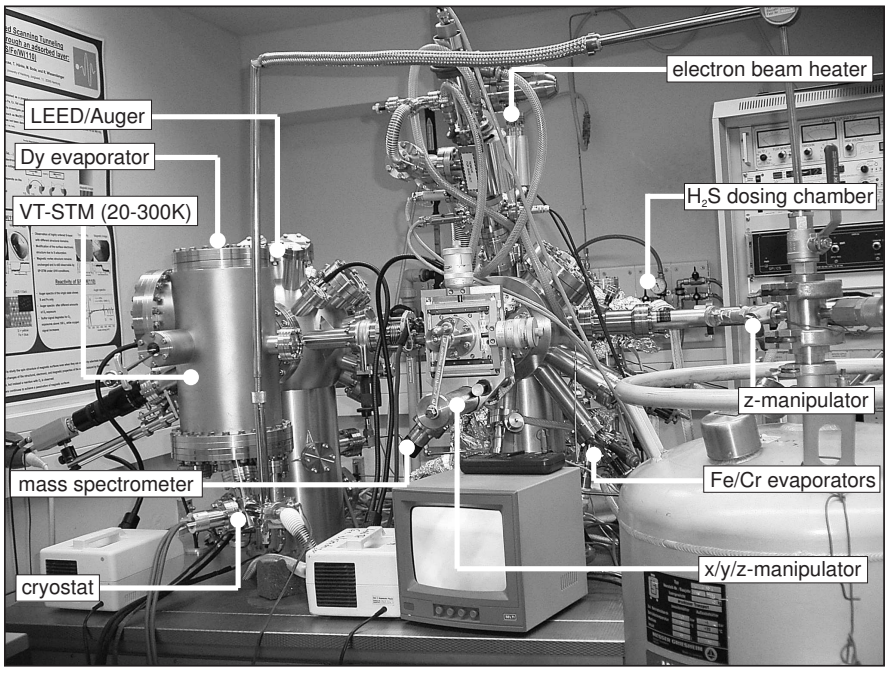

Figure 3.1: Photograph of the UHV-system. On the right the preparation chamber with the tip/sample preparation facilities is shown. The H_2S dosing chamber is barely visible behind the z-manipulator. On the left the analysis chamber with the variable-temperature-STM can be recognized.

hours.

3.1.1 Preparation chamber

The main facilities present in the preparation chamber relevant for this project are an electron beam heater, Cr and Fe evaporators, a (x,y,z)-manipulator equipped with a resistive heater, and an O_2 leak valve.

The home-built electron beam heater allows heating of tips and samples up to $T = 2400$ K. It consists of two parallel tungsten wires that can be connected to a high voltage, $U_{\mathrm{HV}} < 2000$ V, and a tungsten filament powered by a constant current $I_{\mathrm{fil}} \approx 3.5$ A, that acts as a cathode. The sample is suspended by the tungsten wires. As the filament is heated it emits electrons, which are accelerated by the high voltage thereby heating the sample. The sample temperature is measured with an optical pyrometer. The electron beam heater is used for the preparation of W tips and W(110) substrates, where temperatures of up to $T = 2400$ K are required.

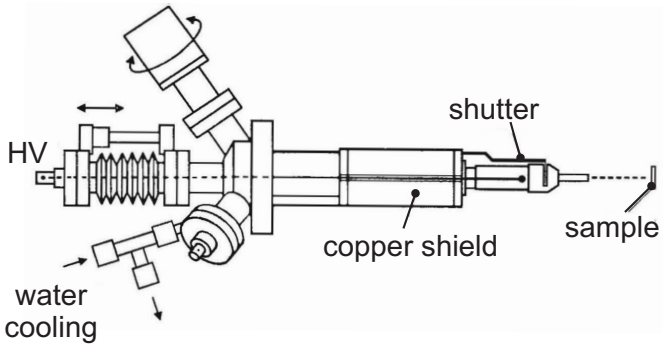

Figure 3.2: Schematic drawing of the Cr/Fe evaporator (taken from Ref. [24]).

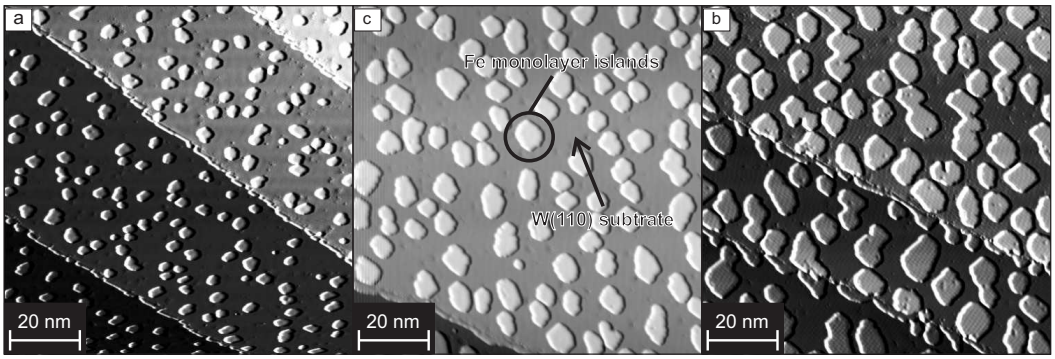

Figure 3.3: Determination of the Fe evaporation rate. STM topographs obtained after Fe evaporation onto W(110) at constant evaporation parameters with evaporation times of (a) 5 s, (b) 9 s, and (c) 15 s.

Cr and Fe are evaporated using electron beam evaporators equipped with flux monitors (see Fig. 3.2). The evaporated material is heated through electron bombardment. The evaporator has a thorium-coated tungsten filament, which has a rather low work function facilitating the emission of electrons. A water cooled copper shield avoids unwanted heating of the surroundings which could cause desorption of adsorbates resulting in a lower film quality. Depending on the properties of the material to be evaporated two types of targets are mounted into the evaporator, crucibles or wires. In the case of Cr the target is a tungsten crucible filled with Cr, while Fe is evaporated from a wire. For the precise calibration of the evaporation rate, submonolayer amounts of the respective metals are evaporated onto a W(110) crystal, the coverage is then determined by STM.

Fig. 3.3 shows an example of such an STM topograph series used for the calibration of the Fe evaporation rate. The Cr and Fe evaporation rates used in

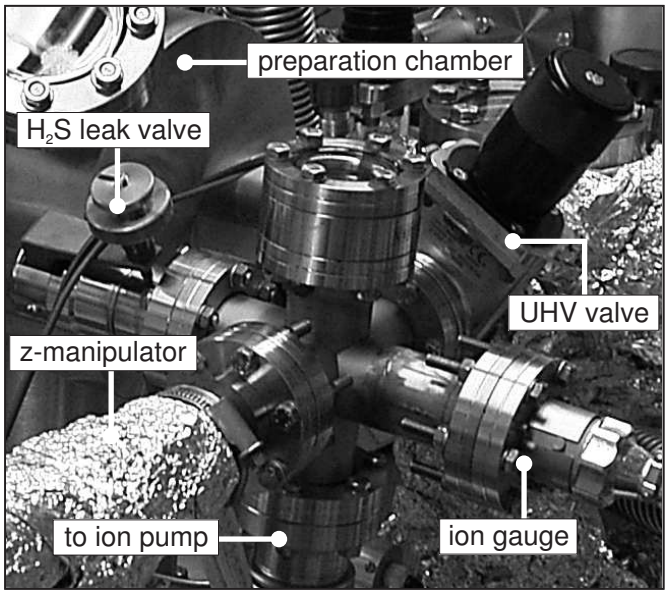

Figure 3.4: Photograph of the H_2S dosing chamber.

this work are $r_{\mathrm{Cr}} = 9 \pm 1$ ML/min and $r_{\mathrm{Fe}} = 1.6 \pm 0.2$ ML/min, respectively.

The (x,y,z)-manipulator present in the preparation chamber allows the positioning of the sample in front of the metal evaporators. It is equipped with a resistive heater that reaches a maximum temperature $T = 1150$ K, which is measured indirectly by a chromel/alumel thermocouple. This heater is used for the annealing of Fe samples and of thin film coated tips.

Furthermore, the preparation chamber is equipped with a leak valve [25] fed by O_2 that allows the introduction of a controlled O_2 flux into the UHV system. This O_2 flux is needed for cleaning the W(110) crystal and to study the reactivity of sulfur saturated Fe(110) samples.

3.1.2 H_2S dosing chamber

H_2S is highly corrosive and may result in an irreversible contamination of the UHV system. To protect the filaments and evaporation material, and to keep a good vacuum in the preparation chamber a satellite H_2S dosing chamber was built.

Fig. 3.4 shows a photograph of this H_2S dosing chamber. A simple and compact design is used. The chamber is physically separated from the preparation chamber by a gate valve. Therefore it is equipped with a dedicated ion pump. Samples can be introduced by means of a manipulator. H_2S was dosed by a leak valve [25]

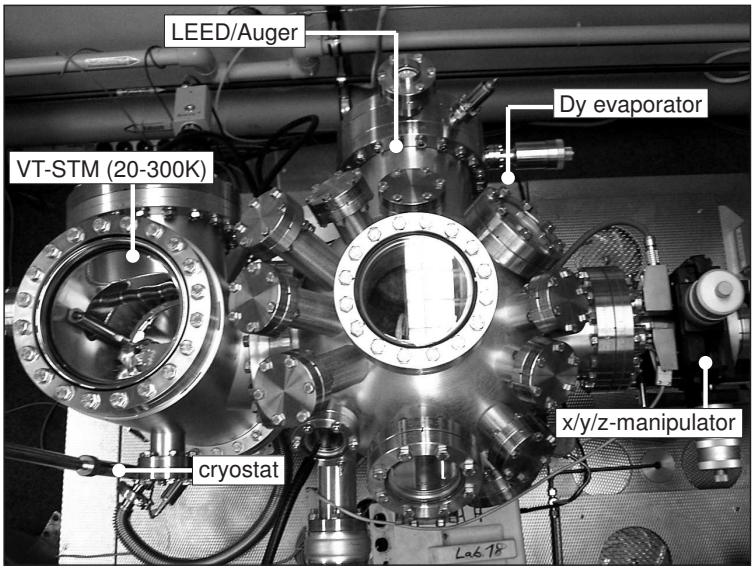

Figure 3.5: Top view of the analysis chamber. On the left the VT-STM is located .

that is fed by a safety bottle containing H_2S with a purity of 99.5%. Since H_2S inhalation is fatal [26] several safety measures are taken, the safety bottle is the smallest available and only filled at $p = 2.5$ bar, and a H_2S sensor is mounted in the proximity of the system.

3.1.3 Analysis chamber

The main analysis instrument, the variable-temperature (VT)-STM, is located in the analysis chamber. The VT-STM is extensively discussed in Sec 3.2. Along with the VT-STM, the analysis chamber also houses the standard surface characterization methods LEED and AES [27]. LEED is a standard technique to check the crystallographic quality of surfaces. AES is predominantly used to check the chemical composition of surfaces.

Along with the surface analysis techniques, a Dy evaporator is mounted in the analysis chamber. Fig. 3.7 shows the Dy evaporator. Although the Dy evaporator also works by electron bombardment, like the Cr/Fe evaporators, its design is much simpler. Namely, the water cooled shield is substituted by a tantalum (Ta) foil shield that simultaneously acts as a radiation shield and an aperture. The Ta shield is connected to one of the four electrical contacts of the corresponding UHV feedthrough. This allows thorough degasing of the Ta shield by electron bombardment prior to Dy evaporation.

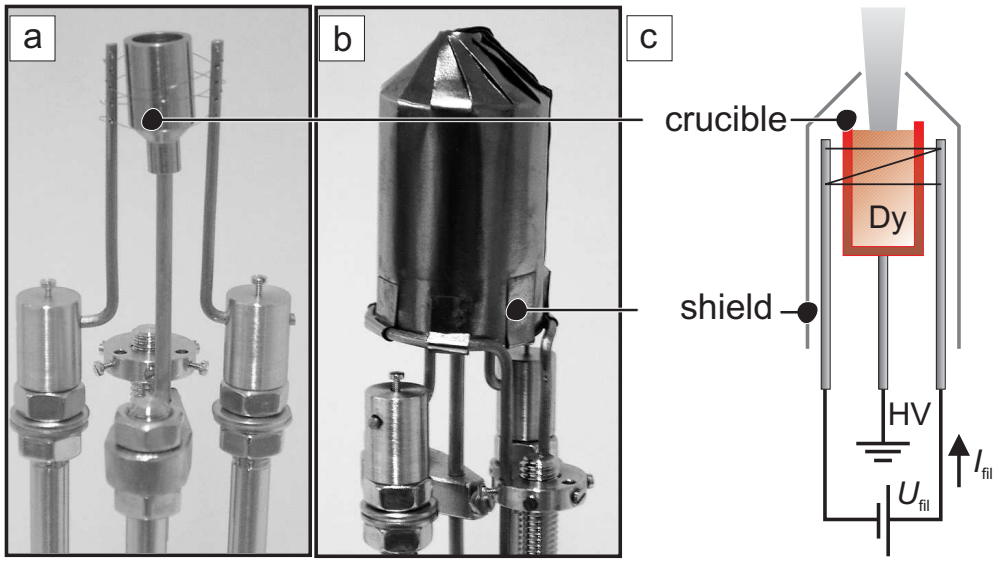

Figure 3.6: Schematic drawing of the Dy evaporator.

Dy metal is delivered as dendritic pieces with a purity of 99.99% and is placed in a tungsten crucible. It is important to notice that Dy has a relatively large vapor pressure at its melting point, i.e. $p = 2 \cdot 10^{-1}$ mbar at $T_S = 1680$ K [28], therefore, it is extremely difficult to melt Dy under UHV conditions. Instead, the evaporator is degassed by extended operation in UHV conditions at a lower temperature. Eventually, at a evaporation rate $r_{Dy} = 9 \pm 1$ ML/min, the pressure in the chamber is lower than $2 \cdot 10^{-10}$ mbar.

Since heavy rare earth metals do not grow as monolayer islands on W(110) [29], the Dy evaporation rate cannot be calibrated by evaporation in the submonolayer regime. To measure the Dy evaporation rate, Dy is evaporated onto a slightly heated W(110) substrate leading to the formation of three-dimensional Dy islands. The volume of the islands is determined by STM. In this work, Dy is always evaporated at $r_{Dy} = 9 \pm 1$ ML/min. Fig. 3.7 shows the STM topograph of a three-dimensional island network used to determine the Dy evaporation rate.

The analysis chamber is equipped with an (x, y, z)-manipulator with an integrated resistive heater, similar to the one introduced in Sec. 3.1.1. It allows the positioning of the sample in front of the LEED/Auger optics and the Dy evaporator, and the annealing of Dy films.

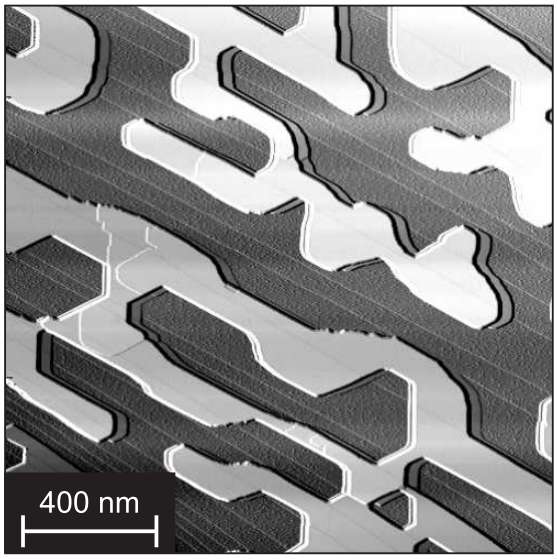

Figure 3.7: Three-dimensional Dy island network formed by evaporation onto a slightly heated W(110) crystal. This data was used for the determination of the evaporation rate of the Dy evaporator.

3.2 The variable-temperature STM

The core of the analysis chamber is the variable-temperature (VT)-STM that was specifically designed for the study of temperature-dependent magnetic phenomena by SP-STM. A more detailed description of the VT-STM can be found in the Ph. D. thesis of Torben Hänke [30].

The STM works at temperatures between 20 K and 300 K and has an easy tip exchange mechanism. In order to allow high energy resolution STS at low temperatures the whole microscope including tip and sample are cooled, in contrast to the commercially available VT-STMs where only the sample is cooled [31]. A cooled tip also allows a larger choice of magnetic materials to coat SP-STM tips. Since ultra-thin magnetic films are often paramagnetic at room temperature (RT), they are not useful in a VT-STM where the tip is left uncooled.

The STM itself is based on the STM design with an *in-situ* tip exchange mechanism developed by D. Haude [32]. This design has an easy and fast tip exchange mechanism combined with being well-isolated from mechanical, acoustical, or electronic noise sources. It has a high resonance frequency which, together with a low resonance frequency external damping system, results in an effective filter against mechanical noise. The damping stage consists of a massive copper plate that is suspended from four metal springs. The STM is placed on top of the copper plate.

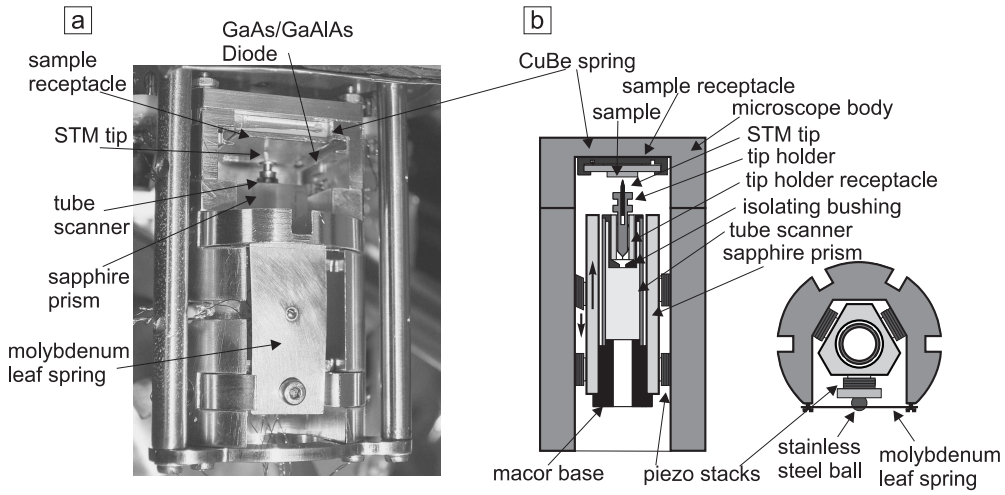

Figure 3.8: (a) Image of the VT-STM. (b) Schematic drawing of the VT-STM in the vertical section (on the left) and the horizontal section (on the right).

The coarse approach mechanism is a piezoelectrically driven stepper motor, built in the "walker" design [33] but operated in the slip-stick mode.

Fig. 3.8 (a) shows a photograph of the STM. Vertical and horizontal cross sections are shown in Fig. 3.8 (b). The sample is mounted face down in the sample holder. The STM tip is mechanically clamped inside the piezoelectric tube scanner which is glued to the sapphire prism of the coarse approach mechanism. A GaAs/GaAlAs diode sensor fixed to the STM-body close to the sample receptacle is used to measure the sample temperature.

The VT-STM is cooled by a liquid He flow cryostat from Cryovac [34], where the temperature is controlled by adjusting the amount of liquid He that flows through the cryostat. The cryostat has an integrated heater regulated by a PID-temperature controller to stabilize the temperature at the heat exchanger. The thermal connection between the STM and the flow cryostat is through highly flexible copper braids with a high thermal conductivity. Their flexibility avoids the transmission of vibrations from the cryostat into the microscope. The STM is surrounded by a radiation shield, which is cooled by the flow cryostat exhaust. Fig. 3.9 shows a photograph of the STM inside the radiation shield as seen through the viewports. The STM-body has a slightly higher temperature than the heat exchanger, measured by the additional temperature sensor on the STM-body. The cooling performance is demonstrated in Fig. 3.10. The STM-body reaches the lowest base temperature after approximately 2 hours. Fig. 3.10 (a) shows that the final temperature of the heat exchanger $T_{\mathrm{ex}} = 6$ K is reached rather quickly

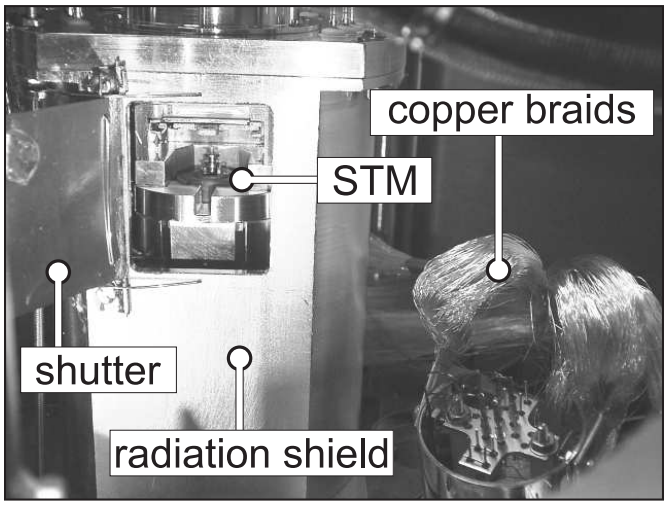

Figure 3.9: View of the VT-STM inside the radiation shield. The microscope can be seen through the open shutter. The copper braids on the right thermally connect the heat exchanger of the cryostat with the microscope.

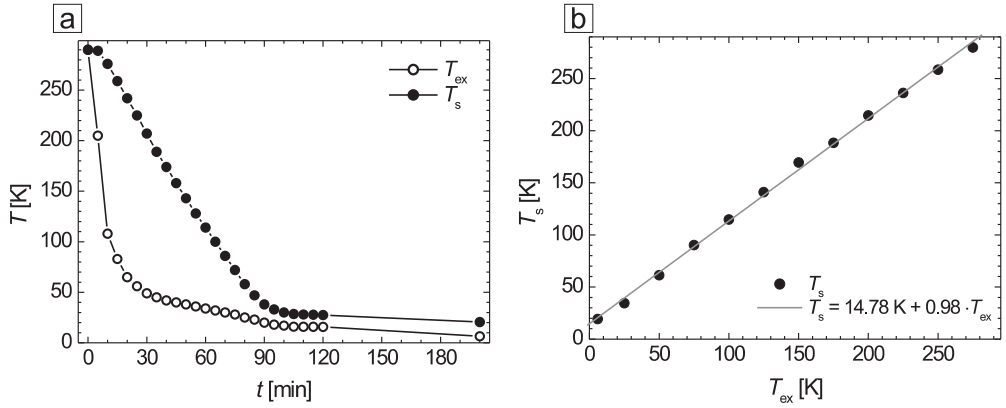

Figure 3.10: Cooling response curves of the cryostat and STM-body. (a) Variation of the temperature of the heat exchanger (T_{ex}) and the microscope (T_{S}) during cool down. After about 2 hours the heat exchanger and the microscope temperatures start to stabilize. (b) Microscope final temperature as a function of the final heat exchanger temperature.

while the sample follows with some delay. Fig. 3.10 (b) shows the dependence of the microscope temperature on the temperature of the heat exchanger. The microscope temperature stays approximately 15 K above the temperature at the heat exchanger.

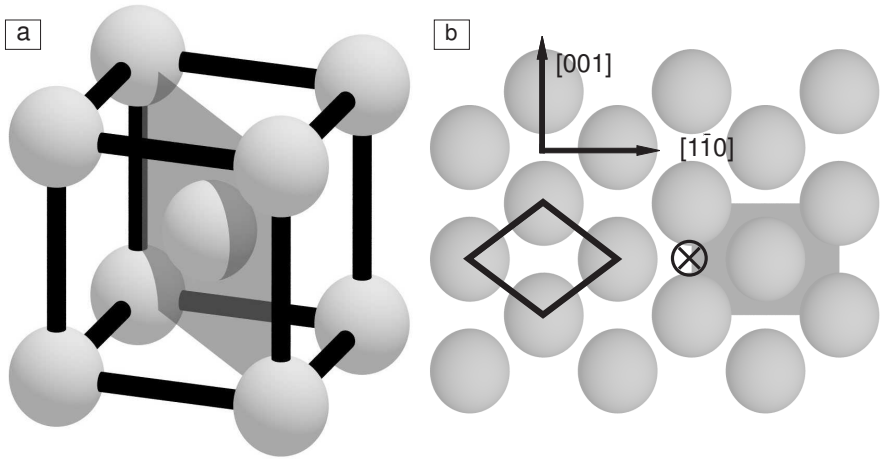

Figure 3.11: (a) Body center cubic (bcc) structure. The (110) plane appear shaded. (b) Atomic distribution of the bcc (110) plane, with its unit cell and crystalline directions. $\otimes$ indicates the 4-fold hollow adsorption site on the bcc(110) surface.

3.3 Preparation

In this section the preparation of the different samples and magnetic sensitive tips used for this work is discussed extensively.

3.3.1 Substrate preparation: W(110) single crystal

The (110) surface of a tungsten single crystal is used to evaporate Dy films and Fe nanostructures. W(110) is known to be an ideal substrate for heteroepitaxy of both Fe and rare earth metals due to its low miscibility and easy cleaning after metal evaporation. Tungsten crystallizes in a body center cubic (bcc) structure with the lattice parameter $a = 316.52$ pm at RT. Fig. 3.11 shows a model of the bcc structure and the bcc(110) plane.

The surface of the W(110) crystal is divided into atomically flat terraces which are separated by monoatomic steps with a height of 223.81 pm at RT. The origin of these steps is the misorientation from the ideal (110) surface, often called miscut. The steps play a crucial role in the epitaxial growth of thin films and nanostructures since they are preferential nucleation sites. In this work two different W(110) single crystals with miscuts of 0.10° and 2° were used. These miscuts result in an average terrace width of 128 nm and 7 nm, respectively.

The cleanliness of the substrate plays a crucial role in the final film quality. W(110) single crystals are relatively simple to prepare *in-situ* with a high degree

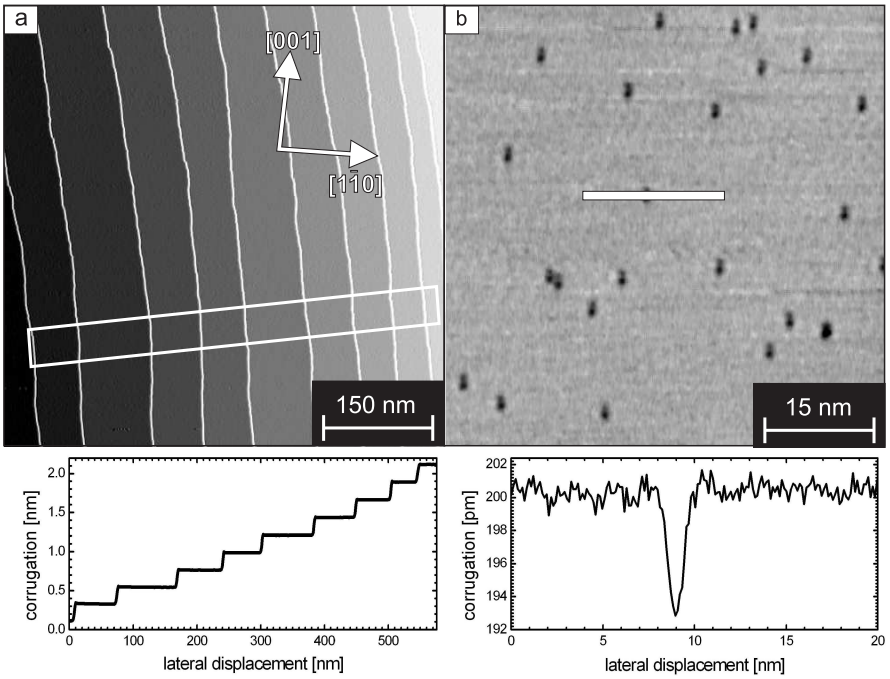

Figure 3.12: (a) STM topograph (upper panel) of a freshly prepared W(110) single crystal. The surface shows atomically flat terraces separated by monoatomic steps, as seen in the line profile (lower panel) (tunneling parameters: $U = -100$ V and $I = 1$ nA). (b) Closer view of a terrace showing only 23 adsorbates. That corresponds to an adsorbate concentration of 1‰. The adsorbates appear 8 pm deep at this stabilization voltage as can be seen in the line profile (lower panel) (tunneling parameters: $U = -200$ mV and $I = 1$ nA).

of cleanliness by cycles of annealing ($T = 1500$ K) in an O_2 atmosphere and a subsequent short high temperature flash ($T = 2300$ K). An improved surface quality was obtained by decreasing the oxygen partial pressure from $2 \cdot 10^{-6}$ mbar at the beginning of the process down to $8 \cdot 10^{-9}$ mbar in the final cycle. During the annealing process carbon impurities segregate to the surface, where they react with the O_2 gas to form CO that desorbs. This process results in a carbon depletion layer below the surface. The flashing of the surface desorbs the rest of the adsorbed oxygen.

Fig. 3.12 shows STM topographs of a freshly prepared W(110) single crystal. In Fig. 3.12 (a) (upper panel), the overview of the crystal reveals a surface divided into terraces by parallel steps. The lower panel shows an averaged line profile taken perpendicular to the steps revealing a step high of 222 ± 10 pm in good agreement with the literature. The STM topograph in Fig. 3.12 (b) is taken on the surface of

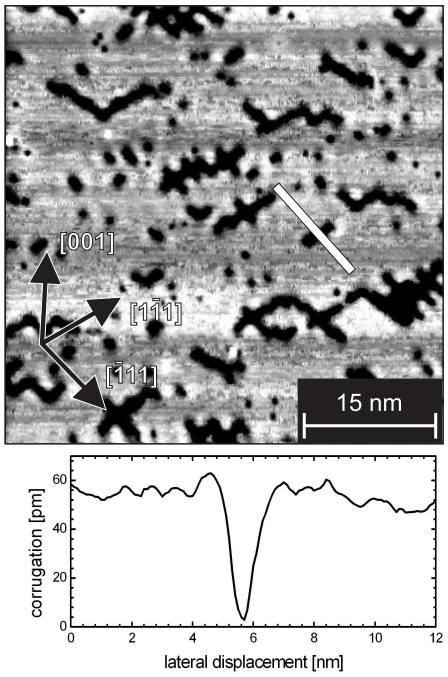

Figure 3.13: STM topograph of a W(110) surface where several Fe films have been deposited and desorbed by flashing. The surface shows line depresions along the close-packed crystallographic directions [1$\bar{1}$0] and the [$\bar{1}$10] probably caused by an incipient carbon reconstruction. The line profile (lower panel) shows that at the chosen stabilization voltage the depression has a depth of approximately 60 pm (tunneling parameters: $U = -1$ V and $I = 30$ nA).

a terrace. The terrace is atomically flat, and several adsorbates can be observed. At the bias voltage used, the adsorbates appear as 8 pm deep depressions. The adsorbate concentration is as low as 1‰.

Once the crystal has been cleaned, it is usually sufficient to flash the crystal between two sample preparations. However, after a number of metal deposition-flashing cycles the substrate begins to accumulate impurities, probably carbon. It is not clear whether these impurities originate from segregation or from the evaporated material. When the amount of adsorbates is too high, the whole cleaning process in O_2 atmosphere has to be repeated. Fig. 3.13 shows an "old" crystal that has been used for several metal deposition experiments. The STM topograph of the surface reveals the formation of carbon reconstructions, as previously studied by LEED and STM [35]. The regions contaminated with carbon appear as trenches, with a depth of 60 pm along the closed-packed directions of the surface.

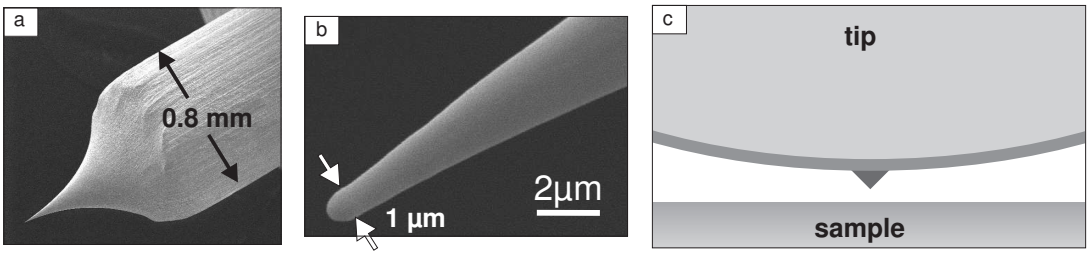

Figure 3.14: SEM-micrographs of an electrochemically etched, polycrystalline W tip after a high temperature flash at $T > 2200$ K. (a) The overview shows the shaft of the tip which exhibits a diameter of 0.8 mm. (b) High-resolution SEM image of the very end of the tip. The tip apex has an angle of about 15° and the tip diameter amounts to approximately 1 μm. (c) Schematic representation of the tip apex. The magnetic film is very thin compared to the curvature of the tip. Probably, a small magnetic cluster protrudes from the tip, which is responsible for the high lateral resolution of SP-STM.

3.3.2 Tip preparation

The preparation of electronically and magnetically stable tips is a crucial requirement for SP-STM/STS. For the *in-situ* preparation of magnetic sensitive tips two different methods are applied in this work: (i) Cr and Fe coating, where the metals are evaporated onto a W tip and post-annealed as explained extensively in Ref. [14]; (ii) Dy coating, where the tip is brought into mechanical contact with a Dy surface, following the procedure described in Ref. [36].

The tips are sharpened from a 0.8 mm diameter polycrystalline W wire by electrochemical etching. The wire is ac-etched in a solution of NaOH in distilled water (8 g NaOH per 100 ml H_2O). After etching, the tips have a typical diameter of 20 nm to 30 nm at the tip apex. Fig. 3.14 (a) shows a scanning electron microscopy (SEM) image of such an etched tip (data from Ref. [37]). Prior to magnetic coating, the tip is flashed to at least $T = 1500$ K. This procedure removes the oxide layer at the tip and results in increased adhesion of the magnetic films, but the heating melts the tip apex leading to tip radius of about 500 nm. A high-resolution SEM image of the very end of a flashed tip is shown in Fig. 3.14 (b).

The tips prepared by magnetic film evaporation, are coated with a thin film of several monolayers followed by annealing at $T = 550$ K for $t = 4$ min. The annealing of the coated tips results in a stable magnetic film at the tip apex. By choosing which and how much magnetic material is evaporated onto the tips, it is possible to determine the in-plane or out-of-plane sensitivity of the magnetic tip, and the presence or absence of stray fields from the tip. In this work mainly tips

coated with at least 100 ML Cr are used. These tips have in-plane sensitivity and are stray-field free. Antiferromagnetic tips are more suitable for detailed studies of ferromagnetic samples as the stray field of a ferromagnetically coated tip could affect the sample‘s domain structure [38].

Flashed W tips that are brought in contact with a Dy layer exhibit a strong in-plane magnetic contrast. This Dy coating is accomplished either by gently touching the Dy surface with the tip or by dipping the tip several nanometers into the film. The origin of the magnetic sensitive tips is probably the presence of Dy clusters that attach to the tips upon contact. The Dy cluster should be large enough to be ferromagnetic at the measurement temperature, since a superparamagnetic cluster would result in a vanishing or unstable contrast. This tip preparation method is highly flexible but uncontrolled. Although there is no control of the final tip state, it is always possible to repeat the tip preparation to obtain a different tip magnetization orientation or polarization. The flexibility obtained by dipping the tip into the Dy film is comparable to the procedure of transferring magnetic material from the surface to the tip by field evaporation [39]. Stable, highly polarized tips are prepared and used at temperatures as high as $T = 65$ K.

Chapter 4

SP-STM through an adsorbate layer: sulfur-covered Fe/W(110)

4.1 Introduction

SP-STM/STS is a powerful technique for studying the magnetic properties of surfaces down to the atomic scale [2, 3]. So far it has been used successfully only under UHV conditions because SP-STM requires clean sample surfaces and well–defined magnetic thin film tips which are destroyed when exposed to ambient conditions, mainly due to oxidation. Extending this technique to operation under ambient conditions would be of great importance, allowing the study of industrial relevant sample and devices. One possibility to make surfaces inert against oxidation is passivation. Several reactive metallic surfaces such as Mo(001) [40, 41] (see Fig. 4.1) or Re(0001) [42], have been imaged with non–spin-resolved STM under ambient conditions upon passivation of the surface with a single layer of adsorbed sulfur. Beyond application aspects there is also a fundamental interest in SP-STM experiments through adsorbate layers since they allow the investigation of spin transport properties under well–defined surface conditions. So far, SP-STM through an adsorbed layer has not been demonstrated. In this work SP-STM through an adsorbate layer is studied.

Obviously, the ideal test sample for spin transport studies through adsorbate-layers should exhibit a magnetic domain structure that does not critically depend on the surface anisotropy but is instead determined by bulk properties. In the past the spin structures of numerous iron nanostructures grown on W(110) have been studied with SP-STM [8, 43–46]. Most of them, such as iron double-layer nanowires or islands on W(110) [43–45], are very sensitive to surface impurities [47, 48]. One exception are three–dimensional Fe(110) islands on W(110).

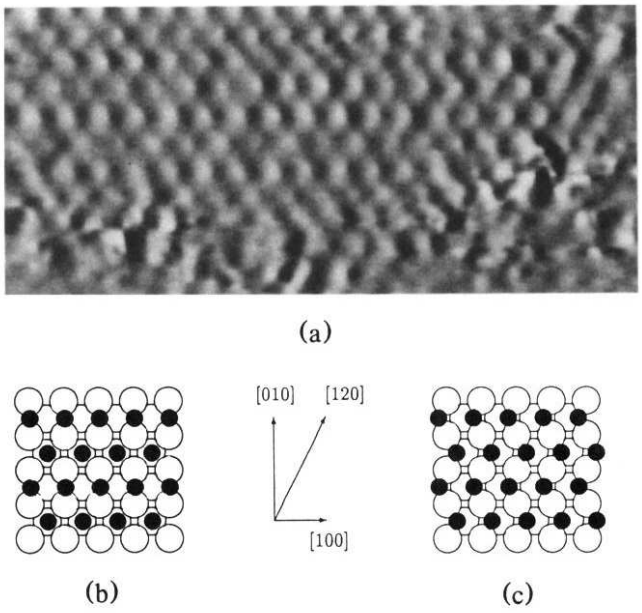

FIG. 1. (a) STM image, recorded in the barrier-height mode, of a 55×25-Å^2 region of a Mo(001)-S(100%)$p(1\times2)$ surface. (b),(c) Possible models for the $p(1\times2)$ sulfur superlattice on Mo(001).

Figure 4.1: Atomically resolved STM topograph on S/Mo(001) (1×2) S reconstruction under ambient conditions taken from Ref. [40].

At suitable dimensions they exhibit a magnetic vortex structure which has recently been observed by SP-STM [8, 46]. Micromagnetic calculations showed that even the surface spin structure of these islands is governed by bulk properties [8], making them particularly suitable for spin-transport studies through a single molecular layer adsorbed on a magnetic surface. Therefore, the test samples for SP-STM through an adsorbate layer selected for this project are sulfur-covered three-dimensional iron islands showing vortex structures.

4.2 Magnetic properties of iron islands grown on W(110)

The domain structure of nanoscale elements has been shown to depend on the morphology of the element. Specially, the lateral size and the thickness determine the spin structure of the elements. For this reason the preparation of suitable samples exhibiting the required domain structure has played a crucial role in

studying the possibility of SP-STM through an adsorbate layer. In this section the growth of iron islands on the W(110) substrate as well as the magnetic properties of these islands are introduced.

4.2.1 Growth of iron islands on W(110)

The epitaxial growth of iron on W(110) has been studied extensively [46–50] in the past. It is known that due to the considerably lower surface energy of Fe(110) ($\gamma_{\mathrm{Fe(110)}} = 2.9$ J·m^2) compared to W(110) ($\gamma_{\mathrm{W(110)}} = 3.5$ J·m^2), iron first forms a closed monoatomic pseudomorphic layer even though the misfit is 9.4%. Depending on the annealing temperature, further iron deposition results either in layer-by-layer growth or three-dimensional island formation.

When amounts of iron higher than 1 ML are deposited, and the sample is sufficiently annealed, the Stranski-Kranstanov growth mode is achieved, i.e., three-dimensional iron islands are formed on top of the perfectly closed monolayer. These islands exhibit a Fe(110) surface. In this work, crystalline three-dimensional iron islands are grown on W(110) by *in-situ* evaporation and subsequent post-annealing. Between 3 ML and 15 ML Fe are evaporated onto the substrate held at RT, and then annealed to a temperature between 490 K and 780 K.

The morphology of the three-dimensional islands depends on the amount of evaporated iron, the annealing temperature, and the local terrace width. Fig. 4.2 (a) shows an overview of a sample with a coverage of 3 ML Fe annealed at $T = 540$ K for 5 min. This particular W(110) substrate has an average miscut of less than 0.1° which corresponds to an average terrace width of approximately 128 nm. Nevertheless, the terrace width varies strongly between 20 nm at the position marked with a black arrow to 600 nm at the position marked with a white arrow, affecting the shape and thickness of the islands. The islands grown on larger terraces are elongated along the [001] crystalline direction, while the ones grown at the edge of step-bunches are compact. Fig. 4.2 (b) shows a model of the depth profile of a three-dimensional island on W(110). The island grows on top of the closed pseudomorphic monolayer. At the position where W(110) step edges occur below the island, lines appear on the island surface due to the different heights of the W(110) and Fe(110) steps. Fig. 4.2 (c) shows a closer view of a compact island. The island has a diamond shape, it is elongated along [001] and the island‘s shorter ends preferentially run along the close-packed directions, $[1\bar{1}1]$ and $[\bar{1}11]$. The lines observed at the surface of the island correspond to the underlying step edges [see Fig. 4.2 (b)]. The surface of the islands is atomically smooth and only a few adsorbates are observed [see Fig. 4.2 (d)].

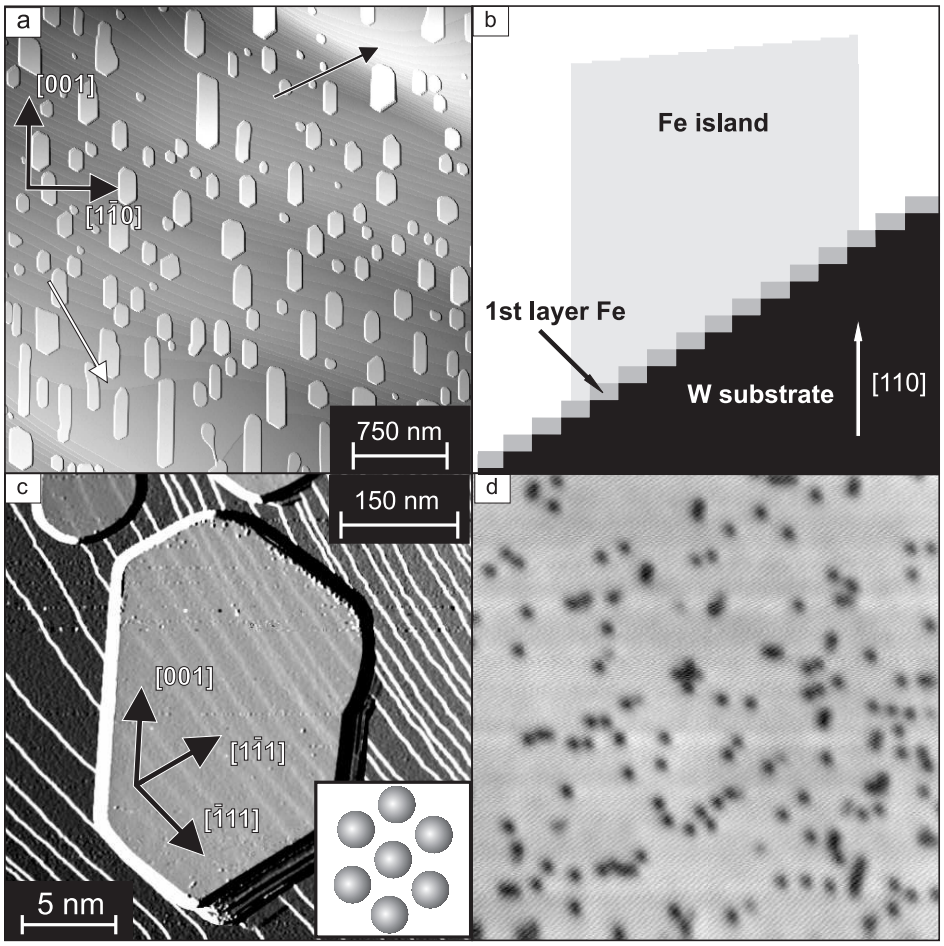

Figure 4.2: (a) STM topograph of 3 ML iron grown on a W(110) crystal and then annealed at 590 K for 5 min. (b) Schematic drawing of the depth profile of an iron island on W(110). The islands grow on top of the pseudomorphic monolayer. As a result of the different step height of Fe(110) and W(110), there are lines corresponding to the underlaying W(110) step edges on the surface of the island. (c) STM topograph of a compact island. (d) The surface of the island is smooth, only showing a few isolated adsorbates (tunneling parameters: $U = -1.0$ V and $I = 0.5$ nA).

4.2.2 SP-STM of iron islands grown on W(110)

The magnetic structure as a function of the morphology of metallic nanodots in general [51–55] and iron islands on W(110) in particular [8, 46] has previously been studied extensively. Crystalline iron islands epitaxially grown on W(110) possess a considerable in-plane uniaxial anisotropy, and are formed on an in-plane ferromagnetic, pseudomorphic iron monolayer [56]. For compact islands, where

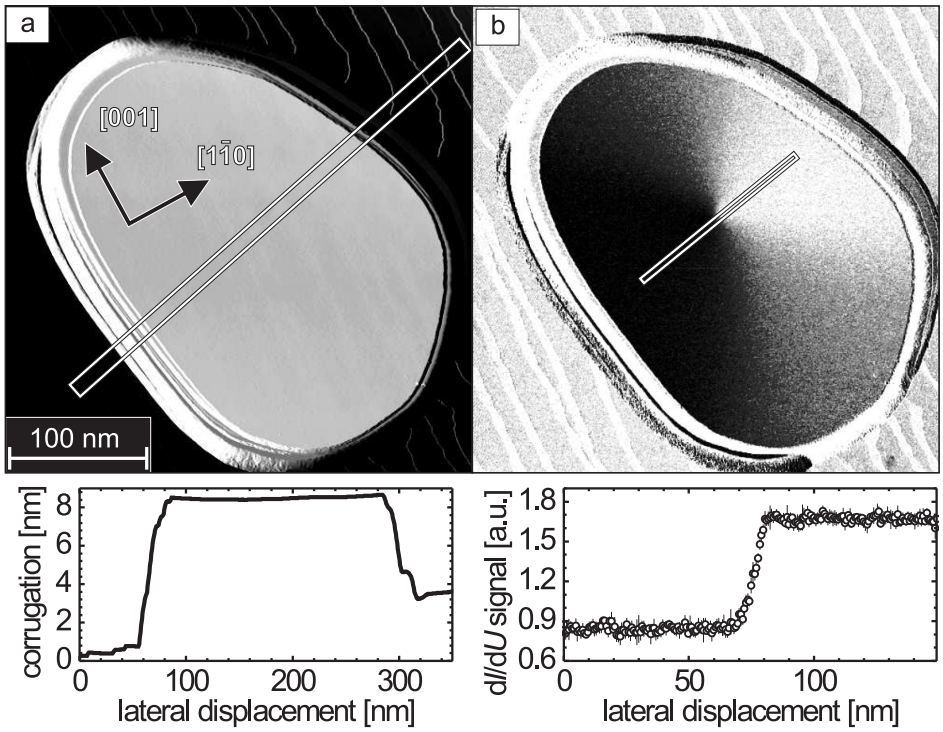

Figure 4.3: (a) STM topograph (top panel) and line profile (bottom) of a clean Fe(110) island. (b) The spin sensitive dI/dU-map (top panel) shows the characteristic pattern of a magnetic vortex. The line profile across the vortex (bottom) reveals that its diameter is $d \approx 10$ nm ($T = 34$ K, tunneling parameters: $U = -500$ mV and $I = 25$ nA).

the lateral dimensions are in the range of 250 nm × 500 nm, the thickness plays a crucial role for the magnetic structure [46]. At a thickness below 5 nm the islands are in a monodomain state, while for thicker islands a series of double-domain, vortex, and double-vortex structures are formed.

Figure 4.3 (a) shows the topography (top panel) and a line section (bottom) of a typical compact three-dimensional iron island. As can be seen in Fig. 4.3 (b) the spin-resolved dI/dU-map exhibits the characteristic pattern of a magnetic vortex [8]. The dimensions of the island are too large to form a single-domain state, because it would cost a relatively high stray field (or dipolar) energy, but they are also too small to form domains like those found in macroscopic pieces of magnetic material because the additional cost of domain wall energy cannot be compensated by the reduction of stray field energy. In this case, the magnetization continuously curls around the island center, drastically reducing the stray field energy and avoiding domain wall energy. As predicted a long time ago [57] and

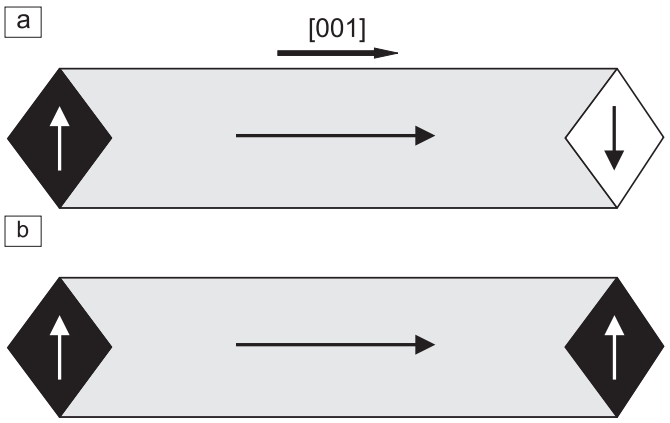

Figure 4.4: Schematic representation of the two possible magnetic states in elongated iron islands depending on the magnetization orientation of the closure domains. (a) S-state corresponding to antiparallel magnetization of the closure domains. (b) C-state corresponding to parallel magnetization of the closure domains.

recently confirmed experimentally [58] the magnetization turns into the surface normal in the middle of the island where the different magnetic signals intersect, forming the so–called vortex core. When using a magnetic tip the differential conductance $\mathrm{d}I/\mathrm{d}U$ depends on the cosine of the angle between the magnetization of the tip and the sample [21]. Therefore, the spin-sensitive $\mathrm{d}I/\mathrm{d}U$ signal changes abruptly at the position of the vortex core when using an in-plane sensitive tip as shown in Fig. 4.3 (b) (bottom panel). The vortex core diameter is 10 ± 2 nm, and is in good agreement with the experimental value reported in Ref. [8] and the predicted diameter in Ref. [57]. The magnetic asymmetry is defined by

$$A(U)_{\max} \equiv \frac{\frac{\mathrm{d}I}{\mathrm{d}U}_{\uparrow\uparrow}(U) - \frac{\mathrm{d}I}{\mathrm{d}U}_{\uparrow\downarrow}(U)}{\frac{\mathrm{d}I}{\mathrm{d}U}_{\uparrow\uparrow}(U) + \frac{\mathrm{d}I}{\mathrm{d}U}_{\uparrow\downarrow}(U)} \ , \tag{4.1}$$

where $\mathrm{d}I/\mathrm{d}U_{\uparrow\uparrow}$ and $\mathrm{d}I/\mathrm{d}U_{\uparrow\downarrow}$ are the differential conductance $\mathrm{d}I/\mathrm{d}U$ measured with the tip and sample in parallel ($\uparrow\uparrow$) and antiparallel ($\uparrow\downarrow$) magnetic orientation, respectively. In the line profile of Fig. 4.3 (b) the asymmetry is $A = 35\%$.

For islands which are strongly elongated along the [001] direction the magnetostatic energy plays a more important role and its minimization forces the island to be magnetized mainly along its long axis. However, at the island´s ends, closure domains are formed to avoid the stray field. The two possibilities depending on the orientation of the magnetization in the closure domains are sketched in Fig. 4.4. Fig. 4.4 (a) shows the so-called S-state where the magnetization of the closure domains is antiparallel. Fig. 4.4 (b) represents the C-state where the

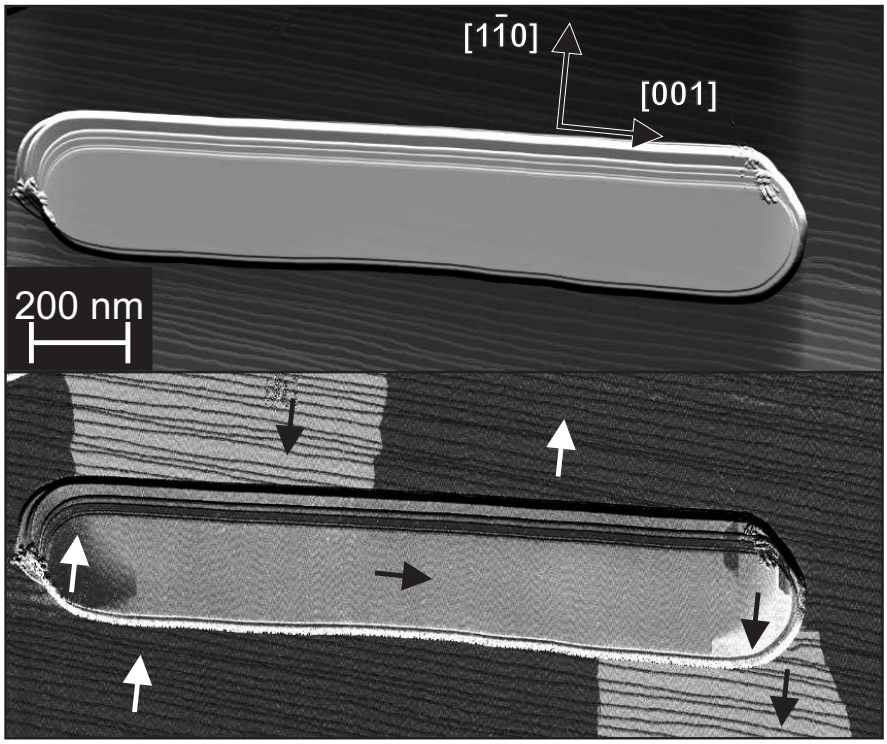

Figure 4.5: STM topograph (top panel) and magnetic dI/dU-map (bottom) of an elongated iron island grown on W(110). The arrows indicate the directions of the magnetization. ($T = 25$ K, tunneling parameters: $U = -200$ mV and $I = 10$ nA).

magnetization of the closure domain is parallel.

Fig. 4.5 shows the topograph (top panel) and the dI/dU-map (bottom) of an elongated iron island. The island is approximately 1500 nm along the [001] direction, and only 300 nm along the [1$\bar{1}$0] direction. Due to uniaxial anisotropy along the [1$\bar{1}$0] direction [59], the monolayer shows two contrast levels. Magnetic contrast is also present in the island. The island shows three contrast levels: dark, grey, and bright. The dark contrast and bright contrast of the island and the monolayer are coupled. The magnetic dI/dU-map can be interpreted as an island in a magnetic S-state, as in Fig. 4.4 (a), where the island is magnetized along [001] to minimize the dipolar energy, and has closure domains which are magnetized in opposite directions and coupled to the monolayer. The arrows in Fig. 4.5 (b) indicate a possible magnetic orientation of every domain in both the island and the monolayer. A domain structure where all the magnetization directions were rotated by 180° is also compatible with the observations.

In order to test the possibility of spin-polarized tunneling through an adsorbate

layer the ideal system is an iron island with a magnetic vortex structure similar to the one shown in Fig. 4.3.

4.3 Sulfur adsorption on Fe(110)

There are two main experimental procedures which have been used in the past to coat Fe(110) surfaces with sulfur: (i) annealing-induced segregation of bulk sulfur impurities onto the surface [60–62], and (ii) dosing with H_2S [61, 63] or atomic sulfur [64]. Depending on the temperature and amount of sulfur, segregation leads to a p(3×1) [60, 62] or to a (1×1) reconstruction [62]. RT dissociation of H_2S on Fe(110) [63] produces an adsorbed layer of atomic sulfur and H_2 gas. At low dosing the adsorbed sulfur forms a p(2×2) reconstruction [61, 64], while a c(3×1) sulfur reconstruction is formed at higher dosing [61]. Obviously, the sticking coefficient abruptly drops to zero at this coverage and any further H_2S exposure cannot increase the amount of adsorbed sulfur on Fe(110).

In order to prepare a closed adsorption layer on the Fe(110) surface, the samples are dosed with H_2S in the satellite dosing chamber (see Sec. 3.1.2). Samples are always dosed with H_2S at RT at a pressure between 1.0×10^{-8} mbar and 5.0×10^{-7} mbar. To study the dependence of the sulfur reconstruction on the total H_2S dose, we perform a series of dosing experiments with exposures between 5 L[1] and 1000 L. In general, we find two dosing regimes: (i) the regime where the resulting sulfur coverage depends on the dosing (Sec. 4.3.1) and (ii) the regime where the sulfur coverage saturates at $\frac{1}{3}$ ML (Sec. 4.3.2).

4.3.1 Low H_2S dosing regime

In this section the dissociation of H_2S on Fe(110) at RT and the resulting reconstructions are studied. It has been reported previously that H_2S dissociates on Fe(110) at RT resulting in adsorbed sulfur and desorbed H_2 gas [61]. Furthermore, the authors report that at low H_2S dosing a $\frac{1}{4}$ ML p(2×2) sulfur reconstruction is formed. Saturation with H_2S leads to a $\frac{1}{3}$ ML sulfur c(3×1) reconstruction. A coexistence of both reconstructions was also reported at intermediated sulfur coverage. The dissociative adsorption of H_2S on Fe(110) can be represented by the following reaction:

$$H_2S_{(g)} + Fe_{(s)} \rightarrow S\text{-}Fe_{(s)} + H_{2(g)} - E_{ads}, \tag{4.2}$$

[1] 1 L is defined as an exposure to a partial pressure of $p = 1.0 \times 10^{-6}$ mbar for the duration $t = 1$ s.

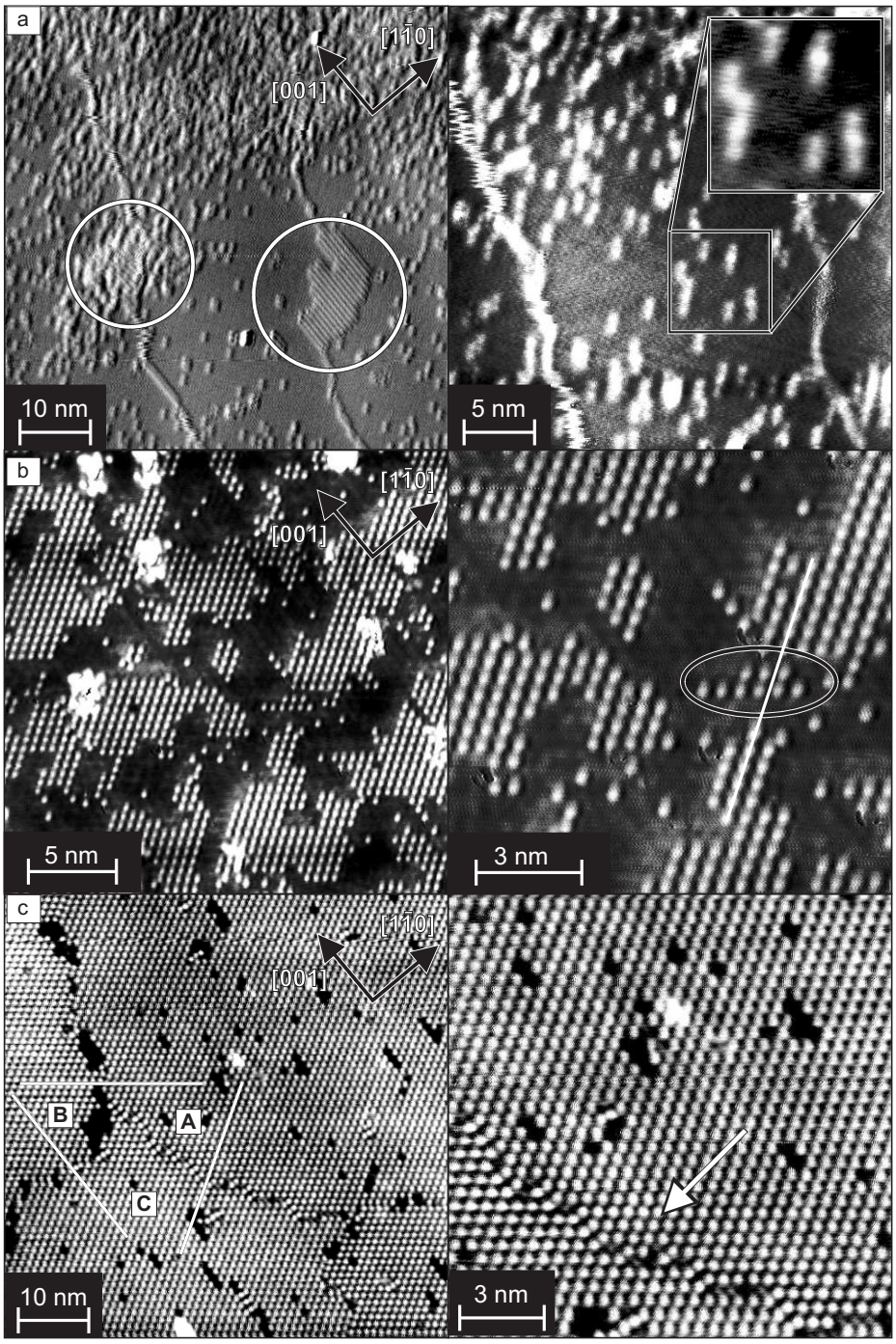

Figure 4.6: STM topograph of Fe(110) islands after H_2S dosing with a sulfur coverage of: (a) 0.02 ML, (b) 0.12 ML, and (c) 0.25 ML.

where the adsorption energy is represented by the difference in the total energy of the product minus the reactants. A positive E_{ads} indicates that adsorption is unfavorable, while a negative value indicates adsorption is likely. E_{ads} depends on the final adsorption site, coverage, and reconstruction.

Fig. 4.6 shows the surface of three-dimensional iron islands after H_2S dosing. At very low dosing [5 L in Fig. 4.6 (a)], only small patches of the surface (circles) show a sulfur reconstruction. Most of the surface is covered by elongated adsorbates (inset). These adsorbates are highly mobile and are pushed away by the STM tip to the upper part of the scanned area. They are probably physisorbed H_2S molecules. The area covered by the sulfur reconstruction increases with increasing H_2S dosing. Fig. 4.6 (b) and Fig. 4.6 (c) show a half-covered surface and an almost closed reconstruction, respectively. The reconstruction is characterized by different structural domains. In Fig. 4.6 (c) three different structural domains are labelled with **A** to **C**. The lines traced across the structural domain boundaries that separate the domains reveal their relative displacement. The structural domain boundaries are atomically disordered [see Fig. 4.6 (c) arrow]. Fig. 4.6 (c) also shows numerous sulfur vacancies in the reconstruction. The lattice parameters along the [001] and $[1\bar{1}0]$ directions are 5.8 ± 0.5 Å and 8.5 ± 0.5 Å, respectively, which are in good agrement with the lattice parameters of the $\mathrm{p}(2 \times 2)$ reconstruction, 5.73 Å and 8.11 Å.

Fig. 4.7 shows a comparison between the sulfur reconstruction obtained in the low H_2S dosing regime (a) and an atomic model (b) of the p(2×2) reconstruction. It is clear that this is the reconstruction present at low dosing as previously reported [61]. In the atomic model, the sulfur atoms occupy the 4-fold hollow adsorption sites [see Fig. 3.11 (b)] as calculated in Ref. [65] and determined by LEED intensity analysis in Ref. [64]. From the STM data is not possible to determine the adsorption site. Two kinds of surface iron atoms can be distinguished, labelled with **A** and **B** in Fig. 4.7 (b) (inset), with short and long Fe-S bonds respectively. This reconstruction exists in four translationally invariant structural domains [see Fig. 4.7 (c)]. These domain can be recognized in Fig. 4.6.

The magnetic properties of the p(2×2)-Fe(110) sulfur reconstruction has been studied using density functional theory (DFT) [65]. According to these calculations, the iron atoms at the clean Fe(110) surface exhibit an enhanced magnetic moment from a bulk value of 2 μ_B to a surface value of 2.5 μ_B. However, the calculated magnetic moments depart considerably from the experimental bulk magnetic moment 2.22 μ_B [66] and experimental surface magnetic moment $2.7 \pm .2$ μ_B [67, 68]. In the calculations, the sulfur adsorption results in a reduction of the enhancement of magnetic moment for the iron surface atoms to 2.03 μ_B

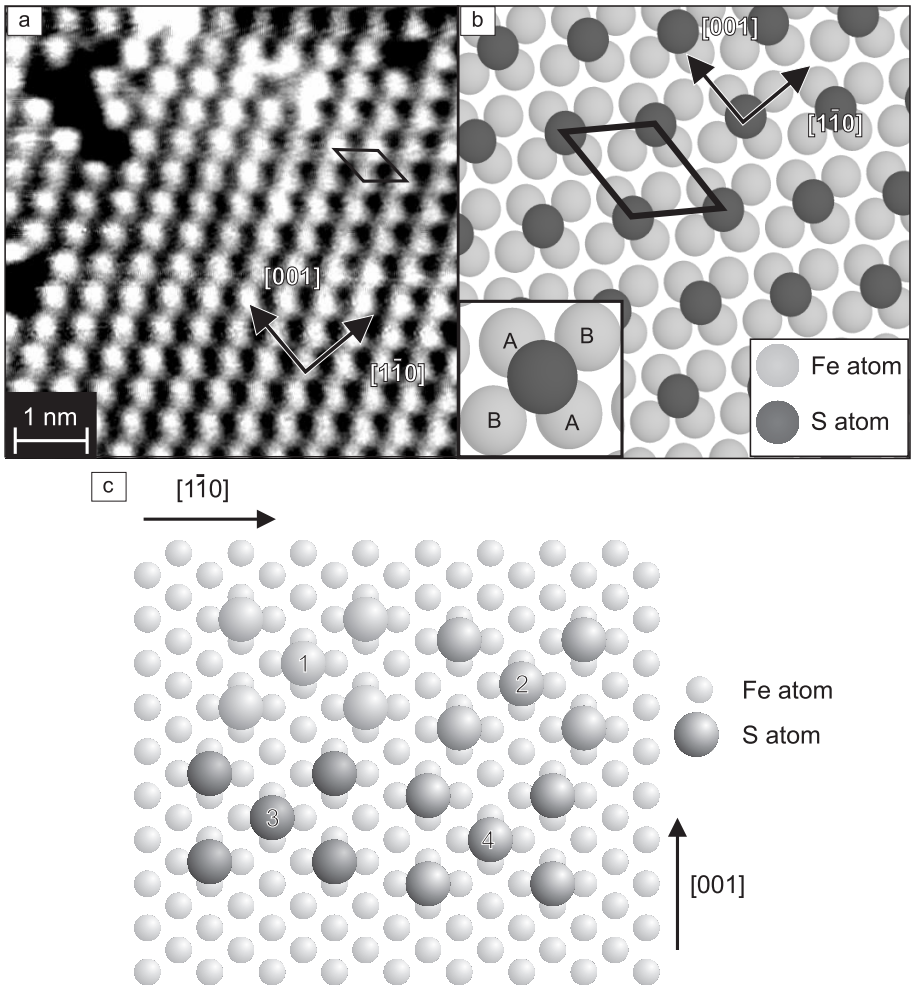

Figure 4.7: (a) STM topograph on the surface of Fe(110) island after H_2S dosing ($T = 28$ K, tunneling parameter: $U = -25$ mV and $I = 20$ nA). (b) Atomic model of a p(2×2) reconstruction. (c) Four possible translationally invariant structural domains of the p(2×2) reconstruction.

for type **A** and 2.41 μ_B for type **B** iron atoms. The sulfur atoms are also found to carry 0.1 μ_B of magnetic moment. The calculation includes also information about the reconstruction stability. The E_{ads} for the 4-fold hollow site amounts to $E_{ads} = -219.9$ kJ/mol [65, 69]. The binding energy defined as:

$$BE = [nE_S + E(\text{Fe}(110)) - E(\text{Fe}(110) + n\text{S})]/n \tag{4.3}$$

where $E(\text{Fe}(110) + n\text{S})$ is the total energy of the surface with the adsorbed sulfur, $E(\text{Fe}(110))$ is the energy of the clean surface, and E_S is the energy of the isolated sulfur atom, is calculated as ≈ 5.8 eV/atom.

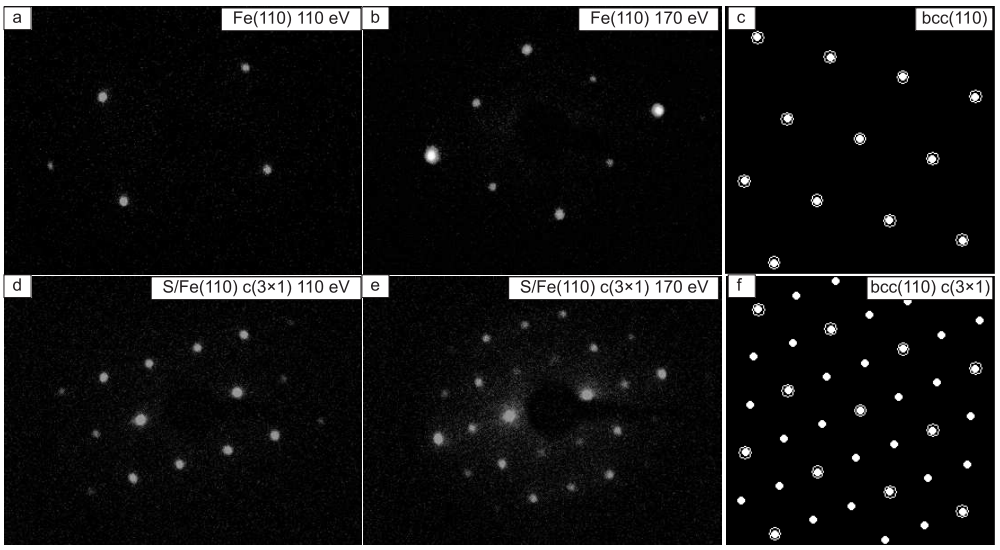

Figure 4.8: LEED patterns of a clean Fe(110) thick film with primary energy (a) E_K = 110 eV and (b) E_K = 170 eV . (c) LEED pattern of the bcc(110) surface obtained with LEEDpat [70]. LEED patterns of sulfur-saturated Fe(110) film with primary energy (d) E_K = 110 eV and (e) E_K = 170 eV. (f) LEED pattern of the bcc(110) c(3×1) surface obtained with LEEDpat. In the simulated LEED patterns the concentric circles represent the bcc(110) spots while the full circles represent the superstructure spots.

Sulfur coverage between $\Theta = \frac{1}{4}$ ML, corresponding to a p(2×2) reconstruction, and $\Theta = \frac{1}{3}$ ML, corresponding to a c(3×1) reconstruction, was not studied in detail but no evidence for the coexistence of different reconstructions was observed.

4.3.2 High H_2S dosing regime.

At H_2S dosings larger than 40 L and as high as 1000 L, the sulfur coverage on the Fe(110) surface saturates at a coverage of $\Theta = \frac{1}{3}$ ML and the surface reconstruction does not depend on the dosing. To compare the saturation reconstruction with the LEED studies from the literature [61, 63], which were performed using Fe(110) single crystals, we prepared continuous thick films of iron on W(110). The samples are obtained by RT deposition of $\Theta > 100$ ML iron and subsequent annealing (T = 450 K). This process results in (110) terminated iron films that completely cover the W(110) substrate. Since the film thickness is much larger than the inelastic mean free path of electrons in the relevant kinetic energy range no LEED or AES signal from the W(110) substrate can be detected.

Fig. 4.8 shows a comparison between the LEED pattern of a clean Fe(110)

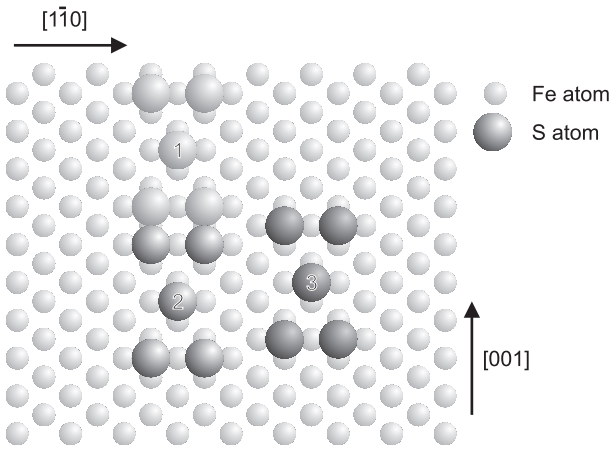

Figure 4.9: Schematic representation of the three translationally invariant structural domains for the c(3×1) sulfur reconstruction. The sulfur atoms are adsorbed at the four-fold hollow site, the favorable adsorption site [75].

film (top row) and a sulfur-saturated Fe(110) film (bottom row). The LEED patterns for clean films show a (1×1) bcc(110) pattern. The LEED pattern for the sulfur-saturated surface reveals reconstruction spots that have been simulated with LEEDpat [70]. This reconstruction was classified as $c(3 \times 1)$ in several adsorbate/bcc(001) systems [61, 71–73]. Using matrix notation it can also be referred to as $\left(\begin{smallmatrix} 1 & -2 \\ 2 & -1 \end{smallmatrix}\right)$ [70, 74]. This reconstruction can exist in three translationally invariant domains on the clean surface, that are schematically represented in Fig. 4.9.

Fig. 4.10 shows an atomically resolved STM topograph of the surface of a sulfur-saturated iron island with line profiles along the [1$\bar{1}$0] and [001] directions. The lattice parameters of the reconstruction are 4.0 ± 0.4 Å and 7.5 ± 0.8 Å, respectively. These values are in good agreement with the theoretical values of 4.05 Å and 8.60 Å for the $c(3 \times 1)$ reconstruction. The observed maximum corrugation is about 10 pm.

Fig. 4.11 (a) shows a STM topograph of a sample that has been saturated with sulfur. Lines are present along the [1$\bar{1}$0] and [001] directions of the surface of the island. In the spin-averaged $\mathrm{d}I/\mathrm{d}U$-map on the islands, Fig. 4.11 (b), these lines appear darker that the rest of the island surface indicating a reduced LDOS. The atomically resolved STM topographs of the island´s surface in Fig. 4.11 (c)-(d) reveal that these lines correspond to structural domain boundaries between perfectly ordered $c(3 \times 1)$ domains. Two types of structural domain boundaries are present, along the [1$\bar{1}$0] (c) and [1$\bar{1}$3] (d) directions. While the structural domain boundaries along the [1$\bar{1}$0] direction run completely undisturbed for more

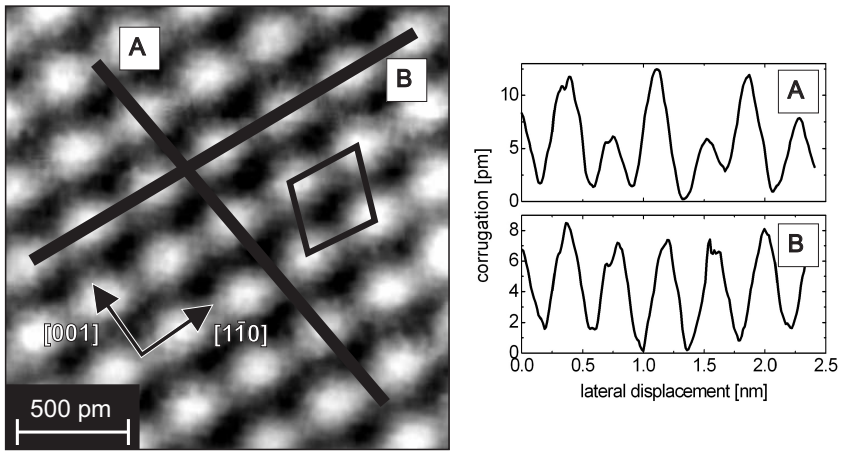

Figure 4.10: STM topograph (left panel) on the c(3×1) reconstruction. The right panel shows the line profile along the [1$\bar{1}$0] and [001] directions. The lattice parameters of the reconstruction are 4.0 ± 0.4 Å and 7.5 ± 0.8 Å, respectively ($T = 31$ K, tunneling parameters: $U = -20$ mV and $I = 25$ nA).

than 100 nm on the surface, the structural domain boundaries along the [1$\bar{1}$3] are characterized by kinks (circles) every couple of nm. These boundary regions may be relevant to the sulfur layer reactivity, since adsorbates preferentially nucleates at the kin sites. To understand the difference between the two types of domain boundaries, atomic models of the structural domain boundaries along the the [1$\bar{1}$0] (e) and [1$\bar{1}$3] (f) directions are shown. In the models, the sulfur atoms are located on the Fe(110) 4-fold hollow site [see Fig. 3.11 (b)] that have been found to be the most favorable adsorption site for the c(3×1) reconstruction [75]. It is clear that the two types of structural domain boundaries are not equivalent.

Fig. 4.12 shows a study of H_2S adsorption on Fe(110) by AES. In Fig. 4.12 (a) the spectrum of a clean Fe(110) film is plotted. The main Fe peaks are clearly developed at 598 eV, 651 eV, and 703 eV. The peaks at 272 eV and 215 eV, reveal the presence of some carbon and argon, respectively, on the surface, while the peaks for nitrogen at 379 eV and oxygen at 503 eV are below the sensitivity of our AES apparatus (approximately 1% of surface atomic density). The main W peaks at 159 eV and 179 eV are not visible either, indicating that the film is continuous and thick enough so that there is no signal from the W(110) substrate. Fig. 4.12 (b) shows the AES spectrum after dosing the film with 50 L H_2S. A sulfur peak appears at 152 eV along with the iron peaks. No further adsorbate peaks appear apart from the argon and carbon peaks already present in the spectrum of the clean surface. A subsequent dosing with 1000 L H_2S does not alter the AES

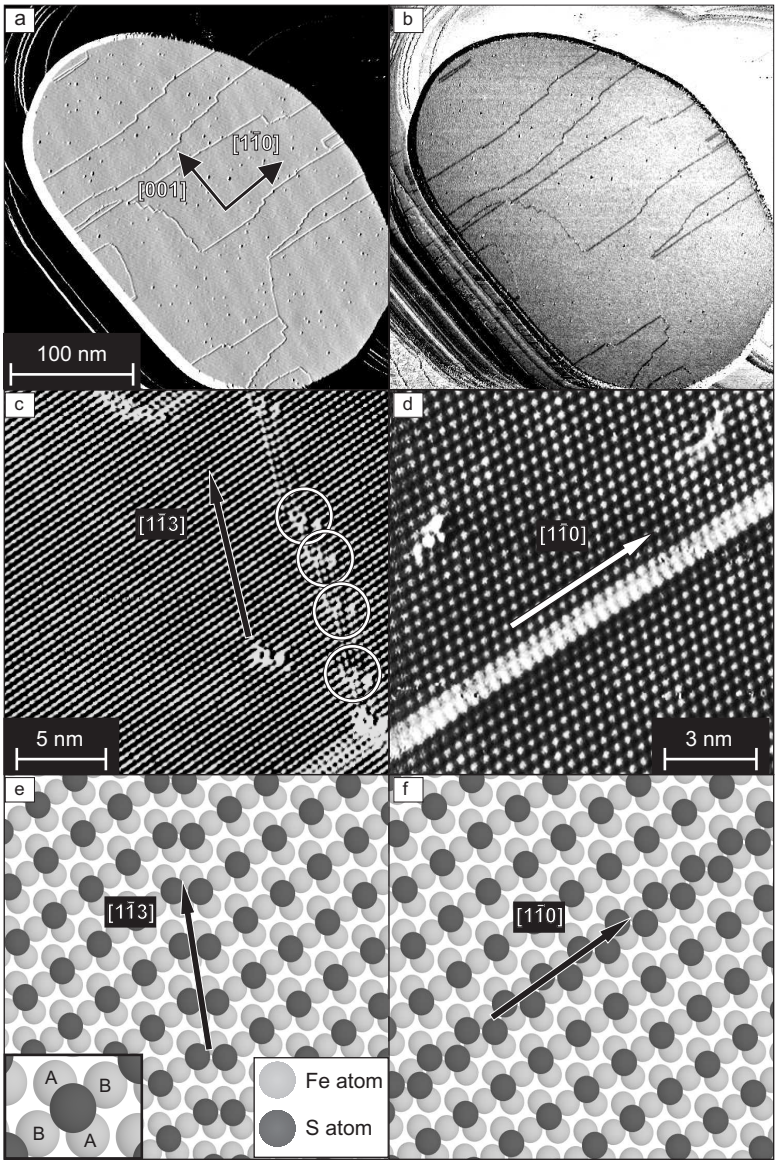

Figure 4.11: STM topograph (a) and dI/dU-map (b) of an iron island dosed with 45 L H_2S. Structural domain boundaries appear as lines ($T = 31$ K, tunneling parameters: $U = -0.5$ V and $I = 25$ nA). Atomically resolved STM topographs of structural domain boundary along the [1$\bar{1}$0] (c) and [1$\bar{1}\bar{3}$] (d) directions (tunneling parameters: $U = -20$ mV and $I = 25$ nA). Atomic models of the c(3×1) reconstruction with structural domain boundaries along the the [1$\bar{1}$0] (e) and [1$\bar{1}\bar{3}$] (f) directions. The inset in (e) shows that two types of iron surface atoms can be distinguished with respect to the Fe-S bond length , i.e., type **A** with a short and type **B** with a long Fe-S bond.

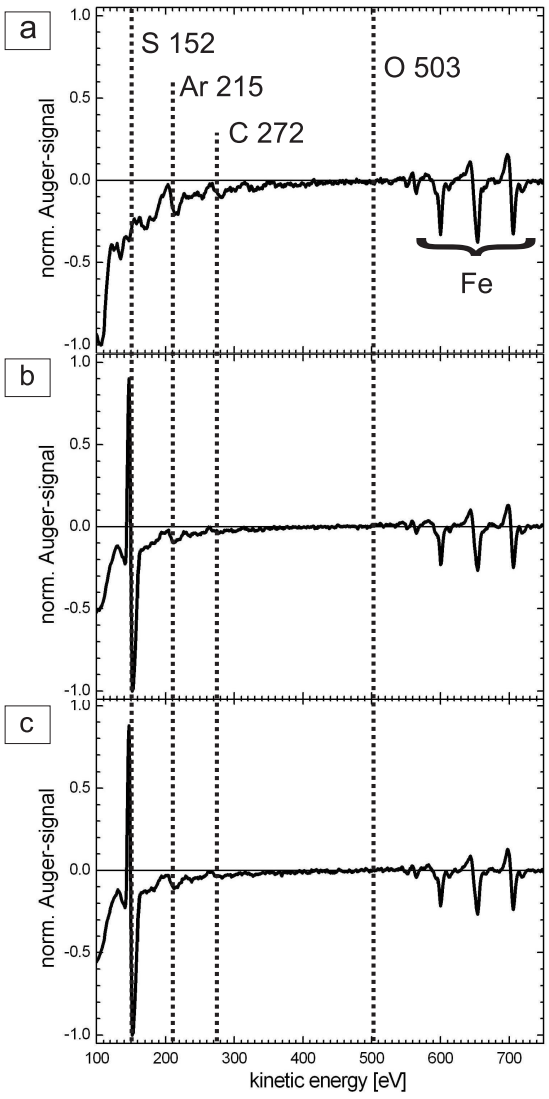

Figure 4.12: AES spectra of a Fe(110) film. (a) A clean 150 ML Fe(110) film on W(110), (b) after exposure to 50 L H_2S, and (c) after saturation with 1000 L H_2S.

spectrum [Fig. 4.12 (c)]. This clearly indicates that after saturation with $\frac{1}{3}$ ML of sulfur no further increase of the sulfur coverage is possible by dosing of H_2S at RT.

Recent DFT calculations [75] showed that the c(3×1) reconstruction with sulfut adsorption at the 4-fold Fe(110) hollow site is more stable than the p(2×2) reconstruction. The c(3×1) reconstruction has a calculated binding energy of 6.00 eV/atom, 3% larger than that of the p(2×2) reconstruction [69]. Since the coverage is also larger, it is clear that c(3×1) will be preferred at high dosing. Furthermore, the authors find a bulk magnetic moment of 2.4 μ_B that changes at the surface to 2.25 μ_B and 2.66 μ_B for atoms of type **A** and **B** (see Fig. 4.11), respectively. The effect of sulfur adsorption on the magnetic moment of surface

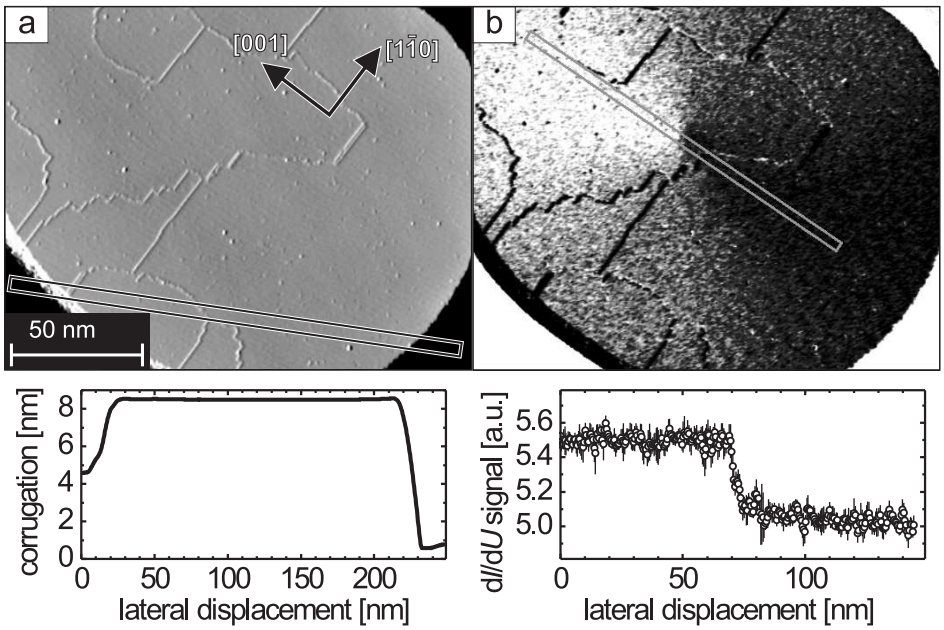

Figure 4.13: (a) STM topograph (top panel) and line section (bottom) of a Fe(110) island after sulfur saturation by 50 L H_2S dosing. Numerous structural domain boundaries appear as straight sections mainly along [1$\bar{1}$0] . (b) Magnetic dI/U (top) of the island´s vortex configuration imaged through the sulfur layer. Due to their different spin-averaged electronic properties, structural domain boundaries are visible as dark lines. The measured vortex core diameter is identical to that of clean islands. ($T = 30$ K, tunneling parameters: $U = -400$ mV and $I = 20$ nA)

iron atoms is larger for the c(3×1) reconstruction than for the p(2×2) reconstruction. Sulfur atoms carry almost no magnetic moment. The quenching of the iron surface magnetic moment and the absence of a magnetic moment in the adsorbed sulfur indicates that a covalent bond is formed between the adsorbed sulfur and the iron surface atoms.

4.4 SP-STM/STS of sulfur-saturated Fe(110) islands

As mentioned above the vortex structure of Fe(110) islands is determined by their bulk properties. Therefore, the spin structure does not change upon sulfur adsorption. Indeed, the magnetic d$I/$dU-map of the sulfur covered islands (Fig. 4.13) qualitatively shows the same vortex structure as the clean islands. Due to differ-

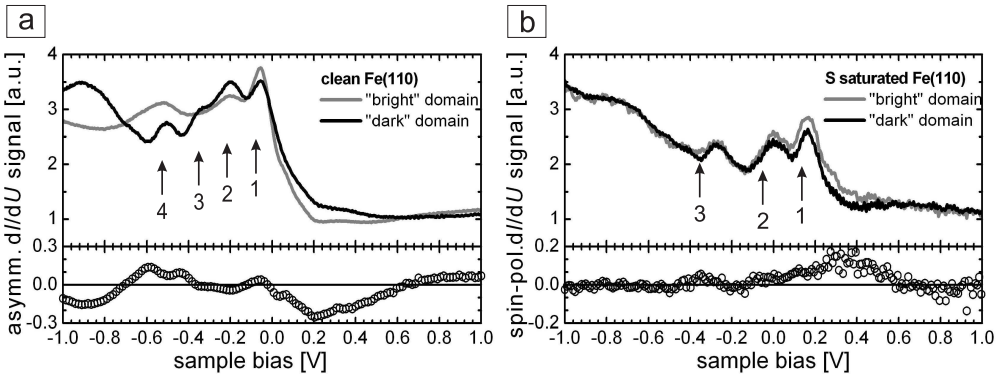

Figure 4.14: (a) Spin-resolved dI/dU spectra of clean Fe(110) (stabilized at $I = 25$ nA and $U = -1$ V) (b) Spin-resolved dI/dU spectra of sulfur-saturated Fe(110) (stabilized at $I = 20$ nA and $U = -1$ V)

ent spin-averaged electronic properties, the structural domain boundaries appear as dark lines in the dI/dU-map of Fig. 4.13 (b). The asymmetry A (Eq. 4.1) is typically a factor of 2 lower than on the clean islands and never exceeds 20-30%. This is not unexpected since the adsorbed sulfur layers carry almost no magnetic moment and the sulfur adsorption in the c(3×1) geometry results in a slight quenching of the magnetic moment of iron surface atoms [75]. However, a finite spin polarization of the tunneling current remains which allows magnetic imaging through the sulfur layer. The observed vortex core diameter of 10 ± 2 nm is identical to that of clean islands.

An important question is how the sulfur adsorption influences the electronic properties of the surface. To answer this question we have performed SP-STM of clean and sulfur covered Fe(110). Fig. 4.14 (a) displays spin-resolved dI/dU spectra of the clean Fe(110) surface which exhibit four peaks labelled 1–4 (top panel). They appear at negative bias ($U \simeq -50, -200, -350, -500$ meV) and may be identified with a $3d$ minority ($\Gamma'^{\downarrow}_{2,5}$) surface resonance [76]. The measured asymmetry amounts to $A = 30\%$ at $U = -200$ mV. In some cases – probably due to tips with a particularly high polarization – values up to $A = 70\%$ were found. Spin-resolved dI/dU spectra of sulfur-saturated Fe(110) are plotted in Fig. 4.14 (b). The electronic properties are different from clean Fe(110) with only three peaks at $U \simeq -270$ meV, $U \simeq 0$ meV (E_{F}), and at $U \simeq +160$ meV but with a notably high spin-polarization $A = 20\%$ at $U = 300$ meV. DFT calculations of the c(3×1) sulfur reconstruction [75] consistently indicate a shift of the DOS toward empty states. Furthermore, the authors find a p-like peak at $U \simeq +200$ meV in the DOS of the sulfur atom which roughly coincides with the observed feature.

However, the vacuum DOS is not calculated. Further calculations are necessary to interpret the measured SP-STS spectra after sulfur saturation.

4.5 Reactivity of sulfur-saturated Fe(110)

Oxidation is expected to be the main degradation process in air for both the clean and the sulfur covered Fe(110) surface. It is known, that the Fe-O bond is more chemically stable than the Fe-S bond., e.g., the reaction of pyrite FeS_2 in air:

$$2FeS_2 + \frac{11}{2}O_2 \rightarrow Fe_2O_3 + 4SO_2 + 1655 \text{ kJ} \tag{4.4}$$

where Fe-S bonds are substituted by Fe-O bonds producing a highly exothermic reaction, with the energy of the reaction $\Delta E = -1655$ kJ [77]. It is expected that the oxygen adsorption would be favored on Fe(110). A plausible reaction on a sulfur-saturated Fe(110) surface with O_2 would be:

$$\text{S-Fe}_{(s)} + \frac{3}{2}O_{2(g)} \rightarrow \text{O-Fe}_{(s)} + SO_{2(g)} + \Delta E \tag{4.5}$$

Although energetically favorable, the oxygen reaction with the Fe(110) surface could be avoided or delayed, if a sulfur adsorbate layer physically impede the contact of the O_2 gas with the iron atoms. This process is known as passivation. The more densely packed the more efficiently an adsorbate layer acts as a physical passivation barrier. Also defects, e.g. vacancies or structural domain boundaries, are important for this process, since they represent weak points for the nucleation of the undesired reaction. The c(3×1) sulfur reconstruction is denser than the p(2×2) reconstruction. Furthermore, we have seen that the structural domain boundaries are more ordered for the c(3×1) sulfur reconstruction. Therefore, it is a better candidate for surface passivation.

To study the degree of passivation of sulfur-saturated Fe(110) films, they were exposed to O_2 inside the UHV system. As a first step a sample was kept under UHV condition at RT for a period of approximately one week. After this time it was not possible to distinguish a freshly prepared sample from the old sample using STM. The next step was controlled dosing of sulfur-saturated Fe(110) films with O_2 gas from a leak valve. O_2 was dosed at a pressure between 5.0×10^{-8} mbar and 1.0×10^{-6} mbar at a dosing 1 L to 3600 L. After dosing the samples were studied by STM and AES.

For dosings lower than 100 L no relevant changes were observed neither in the STM topograph nor in the AES spectra. Fig. 4.15 (a) shows the AES spectrum of a sulfur-saturated Fe(110) film after exposure to 5 L O_2. The spectrum is

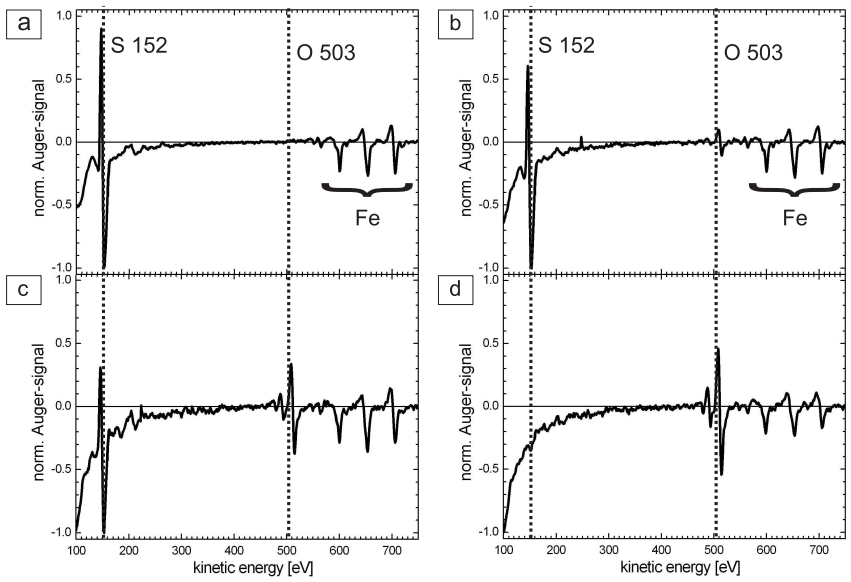

Figure 4.15: AES spectra of sulfur-saturated Fe(110) films exposed to O_2 gas in the UHV chamber. (a) After exposure to 5 L O_2. (b) After exposure to 360 L O_2. (c) After exposure to 3600 L O_2. (d) After exposure to N_2 at atmospheric pressure.

identical to the one of clean sulfur-saturated Fe(110) film in Fig. 4.12 (b). At O_2 dosing larger than 360 L the surface degrades seriously. STM reveals an increased surface roughness, while the AES spectra [Fig. 4.15 (b)-(c)] show a degradation of the sulfur peak and an increase of the oxygen peak. Finally a sulfur-saturated Fe(110) sample was exposed to N_2 at atmospheric pressure in the fast-entry lock. Surprisingly, the AES spectrum of this sample [Fig. 4.15 (d)] shows neither a sulfur peak nor a nitrogen peak, but a strong oxygen peak. This can be understood by considering the purity 99.999% of the N_2 gas used for the experiment. Since the main contaminant of the N_2 gas is O_2, the sample was exposed to about 10^4 L/s. Obviously, the sulfur-saturated Fe(110) surface is very sensitive to oxygen exposure and rapidly and completely oxidizes under these conditions.

It has been reported, that epitaxial Fe(110) films which were dosed with O_2 at elevated temperatures resulted in a well ordered Fe_3O_4 surface with half-metallic behavior [78]. Contrary, our STM results show that the surface after O_2 dosing is amorphous and some spots on the surface are non-conductive. Fig. 4.16 (a) shows the topography of a closed iron layer that has been saturated with sulfur. The structural domain boundaries along Fe[$1\bar{1}0$] are clearly visible (circle). After the exposure to 3600 L O_2 the sample was covered by protrusions as shown in Fig. 4.16 (b). A closer view of the surface is shown in Fig. 4.16 (c). The protrusions

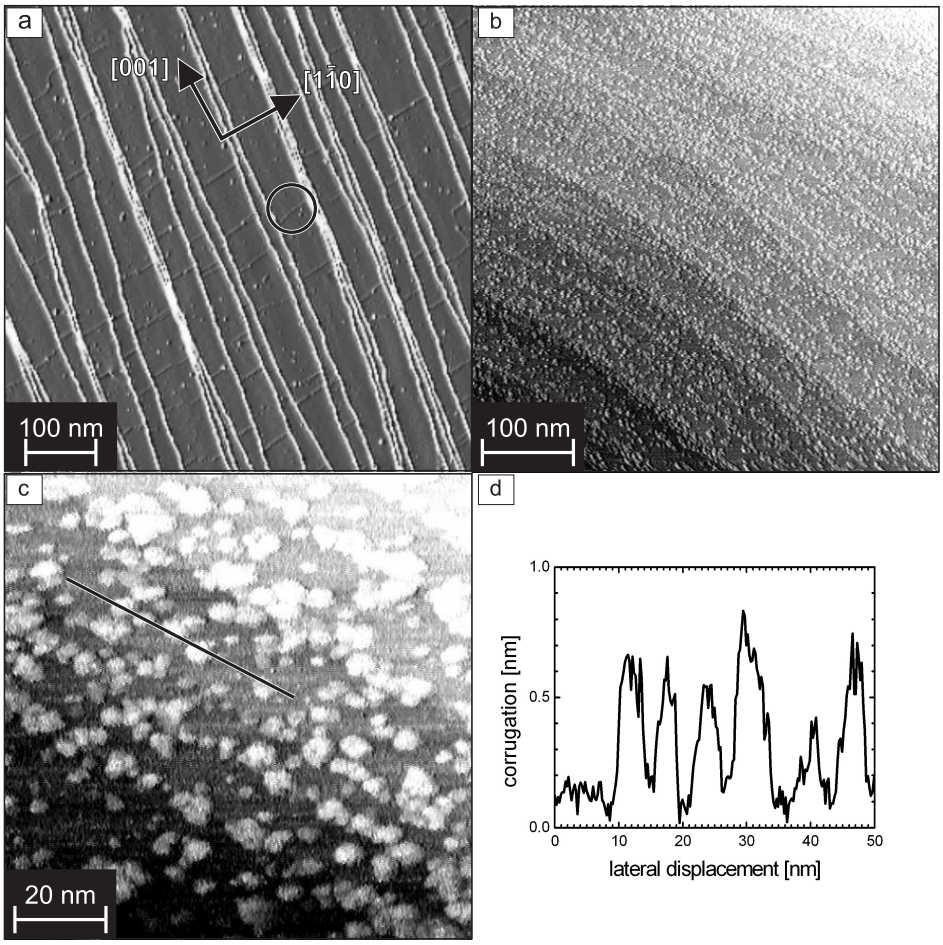

Figure 4.16: (a) STM topograph of a sulfur-saturated Fe(110) film. The structural domain boundary for the c(3 × 1) reconstruction appear as lines along [1$\bar{1}$0]. (b)-(c) STM topograph of a sulfur-saturated Fe(110) film exposed to 3600 L O_2. (d) Line profile across a terrace in (c).

are located preferentially at the step edges. A line profile of the surface shown in Fig. 4.16 (d) reveals that the protrusions have an average height of 0.6 nm and are laterally expanded by 5 nm. According to the previously shown AES data (Fig. 4.15) they are probably a kind of iron oxide nanoparticles.

The c(3 × 1) sulfur reconstruction offers little passivation against O_2. There are several mechanisms that could explain why the sulfur does not passivate the Fe(110) surface. It is possible that the dosed O_2 reacts with the sulfur in the domains leaving areas of exposed Fe(110) that are subsequently oxidized, this would mean that the sulfur layer is not inert enough against O_2. Another explanation

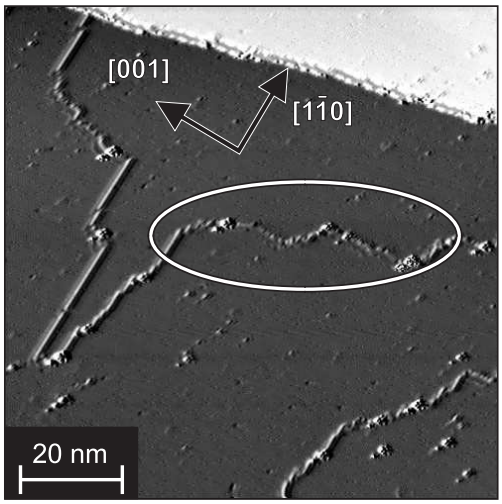

Figure 4.17: STM topograph of a sulfur-saturated Fe(110) closed layer exposed to 5 L O_2. No major effect of the O_2 exposure is observed. Some increased adsorbate nucleation around the kinked structural domain boundaries is observed.

could be that the sulfur layer is inert but is too permeable to O_2 allowing it to reach and react with the iron. If this is the process responsible for the oxidation, it would mean that the c(3×1) reconstruction is not dense enough. Finally, it is possible that the reconstruction is inert and dense enough but the oxidation begins at the weak points that result from the structural domain boundaries. In order to distinguish between these processes the regime of low dosing below 50 L O_2 was studied by STM. In principle it should be possible to distinguish between nucleation of oxidation in the middle of the domain or at the structural domain wall. Fig. 4.17 shows the surface of a sulfur-saturated Fe(110) film that has been exposed to 5 L O_2. Although it is not possible to distinguish extended areas where oxygen might have substituted sulfur, it is noticeable that there is an increased number of adsorbates at the kinks in the domain boundaries along [1$\bar{1}$3]. This may indicate that the oxidation begins at the kinks in the structural domain boundaries.

4.6 Sulfur segregation

Sulfur is a native impurity in bulk iron. It has been shown that the annealing of a (110)-terminated iron crystal under appropriate conditions leads to sulfur segregation onto the surface [62]. The sulfur reconstructions obtained by segre-

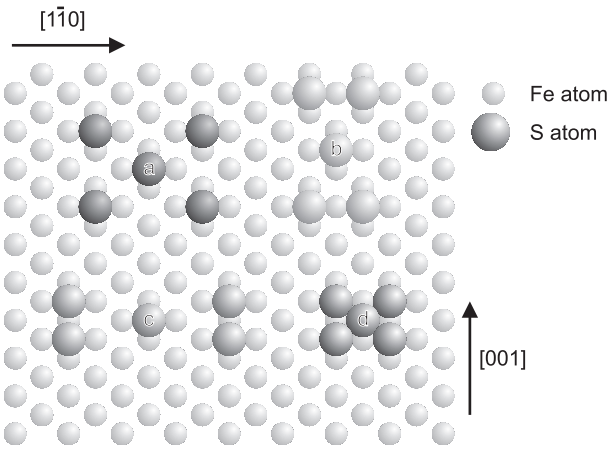

Figure 4.18: Summary of the reported sulfur reconstructions on Fe(110): (a) p(2 × 2), (b) c(3 × 1), (c) p(3 × 1), and (d) (1 × 1).

gation are different to those obtained by H_2S dosing. At increasing annealing temperatures Fe(110) c(6 × 4), p(3 × 1), and (1 × 1) reconstructions were found by Weissenrieder *et al.* [62]. Fig. 4.18 shows the atomic model for the sulfur reconstruction on the Fe(110) surface obtained either by dosing [(a)-(b)] or by segregation [(c)-(d)]. According to the DFT calculation in Ref. [75] the reconstructions obtained by segregation are energetically unfavorable with respect to the reconstruction obtained by H_2S dosing. The presence of subsurface sulfur may stabilize the reconstructions obtained by segregation.

The (1 × 1) sulfur reconstruction is a good candidate for passivation, because it has an atomic density three times higher than the c(3 × 1) reconstruction and no structural domain boundaries. Therefore, the (1 × 1) reconstruction is more resistant to the oxidation processes involving permeability to O_2 or presence of structural domain boundaries. On the other hand, DFT calculations show that the binding energy of the sulfur in the (1 × 1) reconstruction, 3.6 eV/atom [69], is lower that than of the c(3 × 1) reconstruction, 6.0 eV/atom [75], which may result in a less inert sulfur layer.

Since iron films produced by evaporation have a much lower concentration of impurities than a bulk crystal, the annealing process cannot result in segregation of a sufficient amount of sulfur to the surface. We explore an alternative process to increase the sulfur concentration in the evaporated films. This process is schematically represented in Fig. 4.19. Iron evaporation at RT results in a continuous (110)-terminated film. As we have seen before, dosing of about 50 L H_2S results in the saturation of the surface with $\frac{1}{3}$ ML sulfur. Upon annealing,

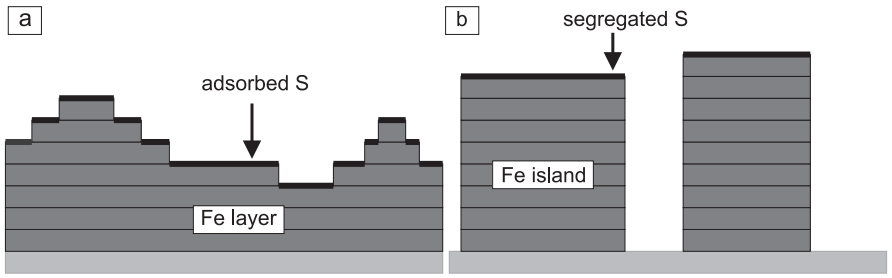

Figure 4.19: Process of iron island formation from sulfur rich iron. (a) After iron evaporation at RT, the sample is saturated with H_2S. A total coverage of $\Theta = \frac{1}{3}$ ML is obtained. (b) Upon annealing, the film breaks up into three-dimensional iron islands that have a smaller Fe(110) exposed surface area that might result in a larger sulfur concentration at the surface.

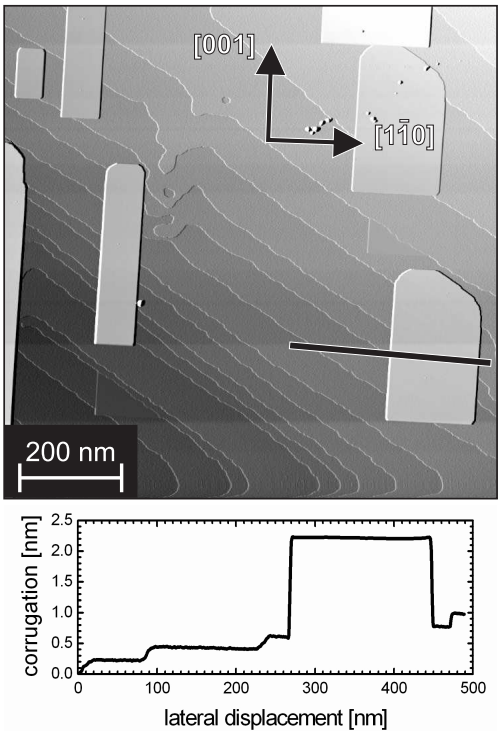

Figure 4.20: STM topograph (top panel) of a sample that has been prepared by evaporation of $\Theta = 8$ ML of iron at RT, then saturated with 50 L H_2S, and finally annealed. The presence of sulfur during the annealing process affects the island growth resulting in differently shaped islands compared to those obtained without sulfur contamination. A line profile (bottom) of one of the islands is shown.

the film breaks up into three-dimensional (110)-terminated islands. The sulfur reconstruction on these island is then studied by STM.

Fig. 4.20 shows a STM topograph of a sample prepared by RT evaporation of 8 ML iron and subsequent dosing with 60 L of H_2S. The final annealing process, at $T = 730$ K for $t = 5$ min, results in three-dimensional islands covering less than 10% of the sample. It is clear, that the presence of the sulfur affects the growth of the three-dimensional islands. As already discussed in Fig. 4.2, a typical three-dimensional island grown from sulfur free iron has a diamond shape elongated along the [001] direction and with the short edges along the close-packed directions. The islands grown from sulfur rich iron have an almost rectangular shape. They are still elongated along the [001] direction, but the short edges are along the $[1\bar{1}0]$ direction. This difference in the island shape may indicate that sulfur segregates to the edges of the islands.

Fig. 4.21 shows a closer view of a rectangular island. The atomically resolved image (b) shows a sulfur reconstruction at the surface. The only reconstruction compatible with a dense sulfur row along $[1\bar{1}0]$ in Fig. 4.21 (b) is the c(3×1) sulfur reconstruction. The lattice parameters of the reconstruction are 4.4 ± 0.4 Å and 8.2 ± 0.8 Å along the $[1\bar{1}0]$ and [001] directions, respectively. These values are in good agreement with the theoretical values of 4.05 Å and 8.60 Å for the c(3×1) sulfur reconstruction. The remaining sulfur in the film probably segregates to the other interfaces of the three-dimensional islands. This will result in the absence of subsurface sulfur that is probably required to stabilize the segregation reconstructions. Nevertheless, there is a qualitative difference between the reconstruction obtained and the simple adsorption reconstruction showed in Fig. 4.11: there are no structural domain boundaries on the island. This indicates that the reconstruction forms by a process different to the one due to H_2S dosing. When dosing with H_2S, the sulfur reconstruction nucleates at different spots on the surface leading to different structural domains that finally merge to a closed overlayer. Here, the sulfur probably segregates during the process of island formation and forms a very small number of nuclei of reconstructed areas from which the reconstruction grows. The process is dominated by domain growth, rather than by nucleation. Thus it is possible that on an atomically flat island, where no defects or steps act as nucleation centers, the average domain size is larger than the size of the island. Therefore, no structural domain boundaries are formed.

Structural monodomain islands may be more robust against oxidation due to the absence of weak spots at structural domain boundaries. An identical sample to that shown in Fig. 4.20 was exposed to N_2 at atmospheric pressure in the fast-entry lock. Fig. 4.22 (a) shows the STM topograph after exposure. Both,

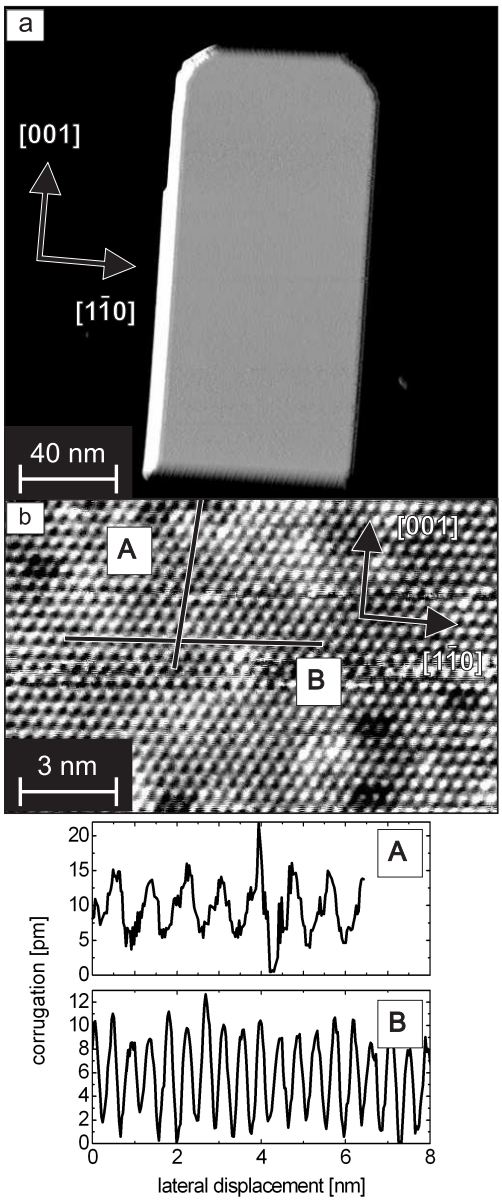

Figure 4.21: (a) STM topograph of an iron island grown from sulfur rich iron. (a) The surface of the island is uniform without signs of possible structural domain boundaries. (b) The atomically resolved STM image (top) and the line profiles along he [1$\bar{1}$0] and [001] directions (bottom) reveal that the island is covered by a c(3 × 1) sulfur reconstruction.

the islands and the wetting layer are densely covered by protrusions similar to those formed by exposing the directly adsorbed c(3 × 1) sulfur reconstruction

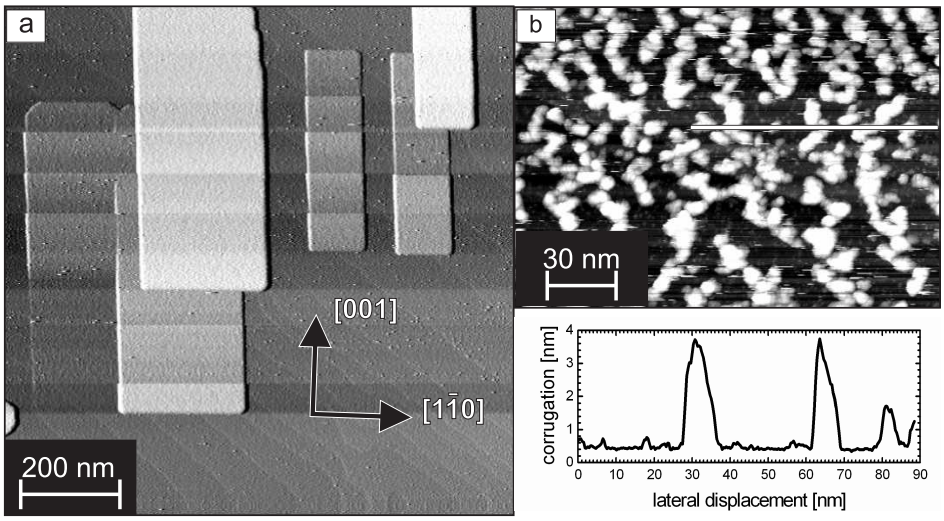

Figure 4.22: Iron islands grown from sulfur rich iron after exposure to N_2 in the fast-entry lock. (a) STM topograph showing that both the islands and the wetting layer are completely covered by iron oxide nanoparticles. (b) STM topograph (top panel) and line profile (bottom) of the surface of an island.

to O_2. The line profile of the island´s surface shown in Fig. 4.22 (b) (lower panel) reveals particles of different sizes with a maximum height of 3 nm. In this case the iron oxide nanoparticles are larger than those in Fig. 4.16, but the oxygen exposure is also much larger. This demonstrates that the sulfur surface reconstruction obtained by the process introduced in Fig. 4.19 does not offer a qualitatively better passivation than the directly dosed samples. Therefore, oxidation at the structural domain boundaries is not the only process responsible for the degradation of sulfur-saturated iron films under exposure to O_2.

Chapter 5

SP-STM/STS of ferromagnetic Dy/W(110) films

5.1 Introduction

The magnetic properties of rare-earth metals have been extensively studied over the last decades. Ref. [79] presents a compilation of the most important results. This research was motivated by interest in their complex magnetic phase diagrams and possible application in devices. In rare-earth metals competition between indirect exchange coupling, magnetocrystalline anisotropy, and magnetoelastic interaction, results in a rich variety of magnetic structures in single crystals and multilayers. The magnetic properties of lanthanides are also important because of the applications of hard-magnetic rare-earth-transition-metal intermetallics, such as SmCo or NdFeB, as permanent magnets and in high-density storage media [80–82]. This chapter discusses the magnetic structure of ferromagnetic Dy films grown on a W(110) crystal. By making use of the high spatial resolution and large maximum scan range of SP-STM, the spin structures of ferromagnetic Dy films from domain wall profiles to the long-range domain structure are studied.

This chapter begins with a short introduction to the relevant properties of bulk Dy (Sec. 5.2). Then, a thickness-dependent analysis of the film morphology is presented (Sec. 5.3). The electronic origin of the magnetic contrast is explained in Sec. 5.4. The main aspects of the thickness-dependent magnetic structure of Dy/W(110) are shown in Sec. 5.5. This chapter concludes with a comparison of our SP-STM results with previously reported resonant soft x-ray scattering data which provide information about the magnetic depth profile of the films (Sec. 5.6).

5.2 Properties of bulk dysprosium

The lanthanide rare-earth metals are characterized by the successive filling of the $4f$ electronic shell from Lanthanum which possesses an empty $4f$ shell till Lutecium with a full $4f$ shell. Dysprosium belongs to the heavy lanthanides (those lanthanides with the $4f$ shell more than half full) with an electronic structure [Xe] $4f^9(5d6s)^3$. The $4f$ electrons are strongly localized and their overlap with the $4f$ shells on neighboring lattice sites is negligible. Therefore, the $4f$ shell does not contribute to any chemical bond which is solely determined by the $5d$ and $6s$ shells. The magnetic ordering of heavy lanthanides is usually explained in the frame of the Ruderman–Kittel–Kasuya–Yosida- (RKKY) model [83–85], since there is no overlap between $4f$ electrons and the exchange is mediated by the conduction electrons.

At RT, the crystalline structure of dysprosium is hexagonal close-packed (hcp) (see Fig. 5.1) with lattice parameters of $a = 359.3$ pm and $c = 565.37$ pm along the $[2\bar{1}\bar{1}0]$ and [0001] directions, respectively [86], resulting in a c/a ratio of 1.574 which departs significantly from the ideal c/a ratio of 1.633.

The magnetic structure of bulk Dy exhibits two phase transitions with decreasing temperature T: a second order phase transition from paramagnetic to helimagnetic at the Néel temperature, $T_N = 178\,K$, and a first order phase transition from helimagnetic to ferromagnetic at the Curie temperature, $T_C = 85\,K$ [87, 88]. In the helimagnetic phase the magnetization lies in the basal (0001) plane. The individual basal planes are uniformly magnetized in a direction which

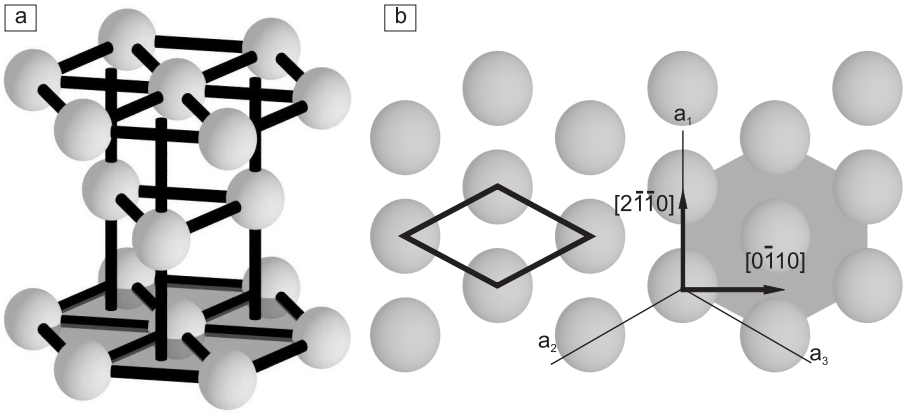

Figure 5.1: (a) Hexagonal close-packed (hcp) crystalline structure. The (0001) plane is marked. (b) Atomic distribution of the (0001) plane, with the unit cell and the crystalline directions.

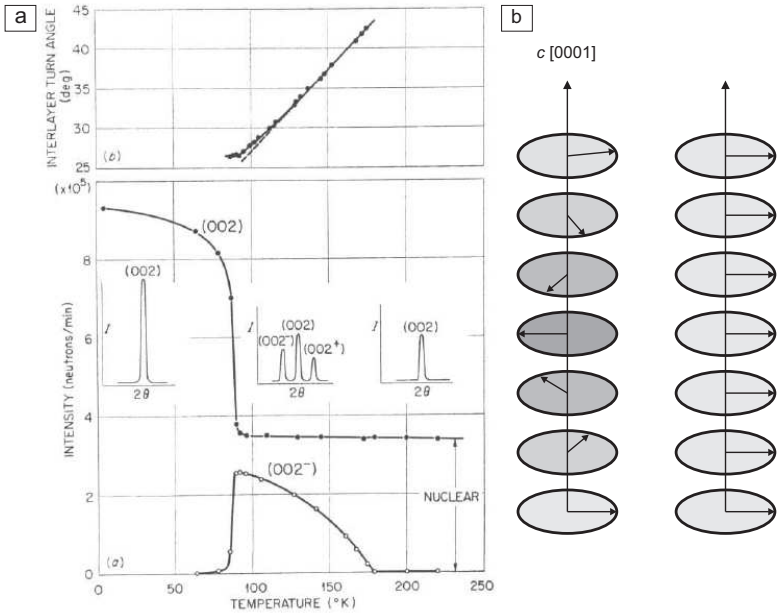

Figure 5.2: (a) Neutron scattering study of the magnetically ordered phases of Dy taken from Ref. [87]. Top, dependence of the helimagnetic turn angle as a function of the temperature in bulk Dy. Bottom, main and satellite neutron scattering peaks as a function of the temperature indicating the two magnetic transitions. (b) Model of the helimagnetic (left) and ferromagnetic (right) phases in bulk Dy.

changes from one layer to the next. The angle between the magnetization in two subsequent basal planes varies between 43° at T_{N} and 26° at T_{C} [87] (see Fig. 5.2). Below T_{C}, the magnetization lies in the basal plane along the $\langle 2\bar{1}\bar{1}0\rangle$ magnetic easy axes. Consequently, six equivalent directions of magnetization are possible. The saturation magnetic moment along the easy axes, $\mu_f = 10.20\ \mu_B$, slightly exceeds the value predicted on the basis of Hund´s rule, g$J = 10.0\ \mu_B$. The excess is usually attributed to the polarization of the conduction electrons [89].

A magnetic crystal elastically deforms under the influence of a magnetic interaction; this effect is called magnetoelastic coupling. The magnetoelastic coupling is particulary large for Dy [90, 91], resulting in a large magnetostriction that distorts the crystalline structure in the magnetically ordered phases. Above T_{N} there is a normal thermal expansion with increasing T. Below the critical temperature of the paramagnetic-helimagnetic phase the lattice parameters, a and b along the $[2\bar{1}\bar{1}0]$ and $[0\bar{1}10]$ directions, respectively, decrease maintaining the hexagonal geometry, while the crystal expands along c-axis, increasing the c/a ratio. At T_{C} the crystal suffers a orthorhombic distortion that involves linear distortions of 0.2%,

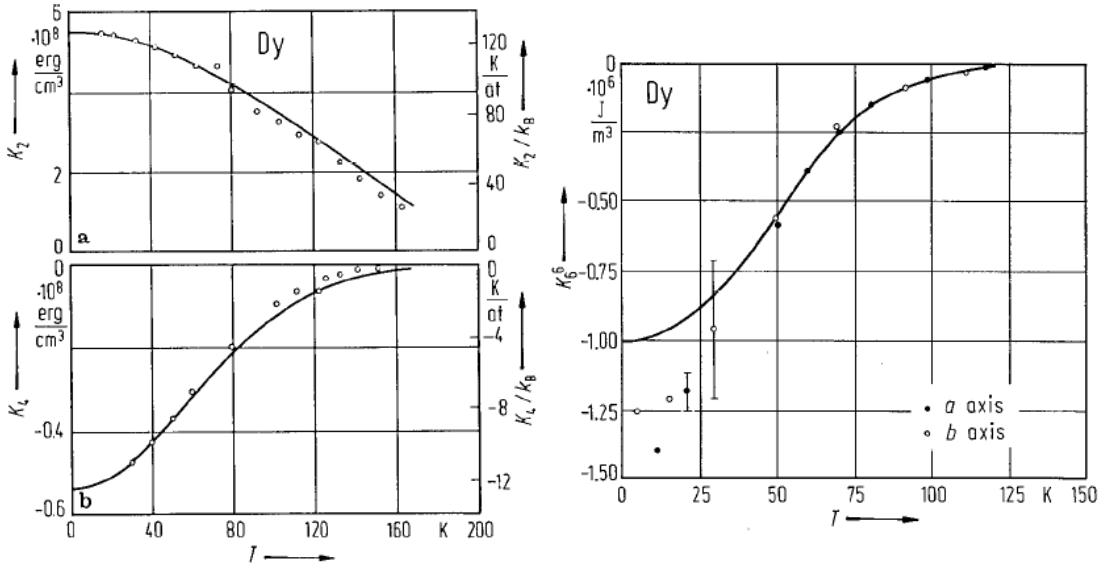

Figure 5.3: Magnetocrystalline anisotropy coefficients K_2, K_4, and K_6^6 as a function of temperature in Dy, from [93–95]

-0.5%, and 0.3% in the a, b, and c directions, respectively [92].

The energy of a ferromagnet depends on the direction of the magnetization relative to the crystallographic axes of the material. This so-called magnetocrystalline anisotropy energy basically results from the spin-orbit interaction. It is necessary to distinguish between the anisotropies of the perfect undisturbed crystal and the induced anisotropies describing the effect of deviations from ideal symmetry, as for example caused by the lattice defects as such dislocations [96]. The general expression for the anisotropy of a crystal with hexagonal symmetry is given by

$$H_{\mathrm{k}} = K_2 \cdot P_2(\cos\theta) + K_4 \cdot P_4(\cos\theta) + K_6 \cdot P_6(\cos\theta) + K_6^6 \cdot \sin^6\theta \cdot \cos 6\phi. \quad (5.1)$$

The P_l^m are Legendre polynomials, and θ and ϕ are the angles of the magnetization with respect to the c and a axes. The values of the magnetocrystalline anisotropy coefficients K_2, K_4, and K_6^6 for bulk Dy as a function of temperature are plotted in Fig. 5.3. The values for Dy are 10 to 1000 times larger than the for ferromagnetic transition metals. The value of K_6 is $\pm 10^3 \mathrm{J/m^3}$ [97], i.e, four orders of magnitude smaller than K_2. The anisotropy barrier between the easy a-axis and the hardest c-axis in the ferromagnetic phase at $T = 60$ K is $E_{\mathrm{A}}(T = 60\ \mathrm{K}) \simeq 7.2 \cdot 10^7\ \mathrm{J/m^3}$, while in the basal plane the anisotropy barrier at $T = 60$ K between a and b axes is only $E_{\mathrm{A}}(T = 60\ \mathrm{K}) \simeq 7.0 \cdot 10^5\ \mathrm{J/m^3}$.

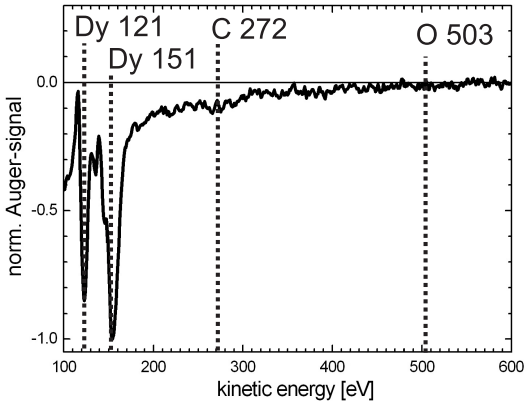

Figure 5.4: AES spectrum of a 90 ML Dy/W(110) film. The spectrum shows well developed Dy peaks, while the intensity of some of the commons impurity peaks (oxygen and carbon) ramains below the sensitivity threshold of 1% for our apparatus.

Another anisotropic term that plays a very important role for interfaces and surfaces is the so-called magnetic surface anisotropy [98]. This effect is attributed to the reduced symmetry of the atomic environment of interface atoms.

5.3 Morphology of Dy/W(110) films

The preparation of clean lanthanide-metal surfaces from a bulk single crystal is almost impossible, not only due to their extreme reactivity, but because bulk impurities have a strong tendency to segregate onto the surface [99, 100]. This problem is circumvented by replacing bulk-single crystals with single crystal thin films epitaxially grown in UHV condition onto a refractory-metal single crystal, such as Mo or W(110) [101]. These rare earth thin films contain lower numbers of interstitial C, N, and O impurities and substitutional Fe and Pd impurities [102]. By selecting appropriate growth parameters and subsequent annealing conditions, films with high surface quality can be prepared.

In this section the thickness-dependent morphology of Dy/W(110) films is discussed. Continuous Dy films with thicknesses Θ from $\Theta = 14$ ML to $\Theta = 450$ ML are prepared by thermal evaporation onto a W(110) single crystal held at RT and subsequent annealing. Dy is evaporated from an electron-bombardment evaporator (see Sec. 3.1.3) at a rate of $r_{\mathrm{Dy}} = 9 \pm 1$ ML/min. The samples are then annealed on the resistive heater in the analysis chamber for 4 min at temperatures between 490 K and 680 K, in order to obtain a flat film. For a Dy coverage larger than 14 ML, this process results in a continuous Dy film.

The AES spectrum of a 90 ML Dy/W(110) film in Fig. 5.4 shows a very low impurity level for the most common contaminants, such as oxygen and carbon, and no signal of W. This AES spectrum indicates that the sample consists of a

clean and continuous Dy film.

Fig. 5.5 shows the epitaxial relation between the hcp Dy film and the bcc (110) W substrate. The LEED pattern of the clean W(110) substrate shows a sharp (1×1) bcc(110) pattern. After the preparation of a 90 ML Dy/W(110) film, the LEED pattern in Fig. 5.5 (c) presents a sharp (0001) (1×1) hexagonal pattern. The comparison of the crystallographic directions in both patterns reveals that the epitaxial orientation follows the Nishiyama-Wassermann epitaxial relationship [103–106], i.e. Dy(0001) ∥ W(110) and Dy$[0\bar{1}10]$ ∥ W$[1\bar{1}0]$, as previously reported in Ref. [102].

The Dy(0001) surface can be atomically resolved with the STM by using the appropriate tunneling parameters, namely a very low tunneling resistance on the order of several kΩ. Fig. 5.6 (b) shows the atomic structure of the surface of a 90 ML Dy film as observed by STM. The line profiles along the close-packed

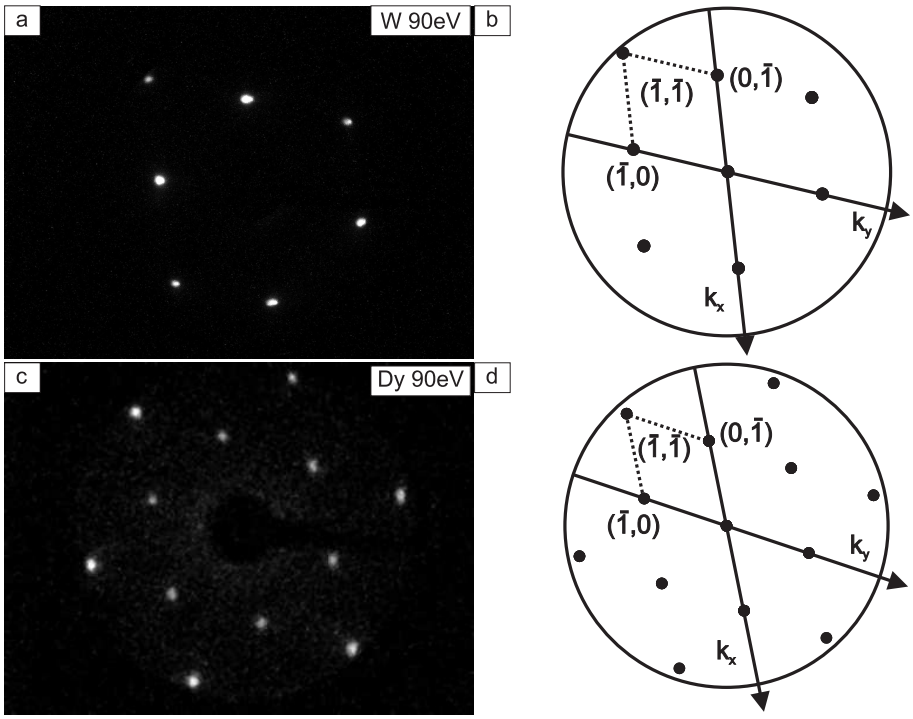

Figure 5.5: Epitaxial relation of Dy on W(110). (a) LEED pattern of the clean W(110) substrate at primary energy $E_K = 90$ eV showing a sharp bcc (110) pattern. (b) Diagram of the bcc (110) reciprocal space with the main directions and the reciprocal unit cell. (c) LEED pattern of a 90 ML Dy/W(110) film at primary energy $E_K = 90$ eV. It shows a sharp hcp (0001) pattern. (d) Diagram of the hcp (0001) reciprocal space with the main direction and the reciprocal unit cell.

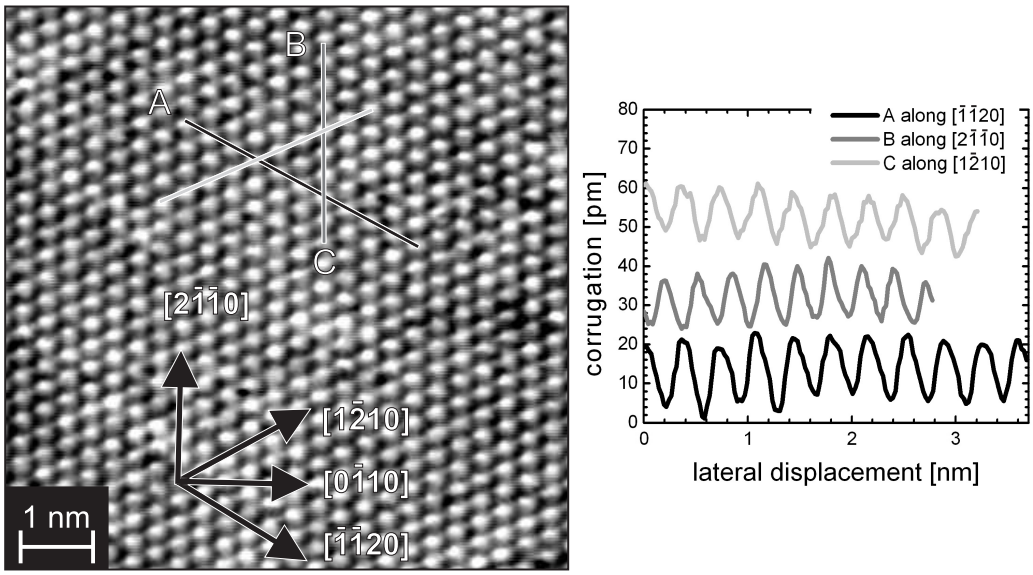

Figure 5.6: Atomically resolved STM topograph (left panel) and line profiles along the close-packed directions (right panel) on a 90 ML Dy/W(110) film. ($T = 41$ K, tunneling parameters: $U = -2.4$ mV, and $I = 330$ nA).

directions reveal a lattice constant of $a = 3.6 \pm 0.2$ Å, along the $[\bar{1}\bar{1}20]$ and the $[1\bar{2}10]$ directions, and $a = 3.2 \pm 0.2$ Å along the $[2\bar{1}10]$ direction. Due to creep of the piezoelectric tube, there is a distortion from a perfect hexagon of approximately 11%. Therefore, the orthorhombic distortion present below T_C (see Sec. 5.2) that amounts only to 1% is not observable by STM.

Figure 5.7 (a)-(d) shows differentiated STM topographs (500 nm × 300 nm) of flat Dy/W(110) films at average nominal coverage Θ of (a) 14 ML, (b) 22 ML, (c) 27 ML, and (d) 45 ML. With the exception of a few islands, the substrate's terrace-and-step structure is generally reproduced by films in the low coverage regime (a). At the position where W(110) step edges run below the Dy/W(110) film, steps of about 0.8 Å appear at the surface [line section in Fig. 5.7 (a) (right panel)]. The origin of these steps is the different height of the steps on the Dy(0001) and W(110) surface. In contrast to the clean substrate (see Fig. 3.12), however, the Dy terraces exhibit numerous narrow trenches along the close-packed $\langle 2\bar{1}10 \rangle$ directions. A few short segments of these trenches are deeper and asymmetric [white arrow and line section in Fig. 5.7 (b) (right panel)]. Occasionally the step edges, which separate adjacent terraces, smooth out [black arrows and line section in Fig. 5.7 (b) (right panel)]. With increasing film thickness [(b) and (c)] the asymmetric trenches as well as the smooth step edges become longer.

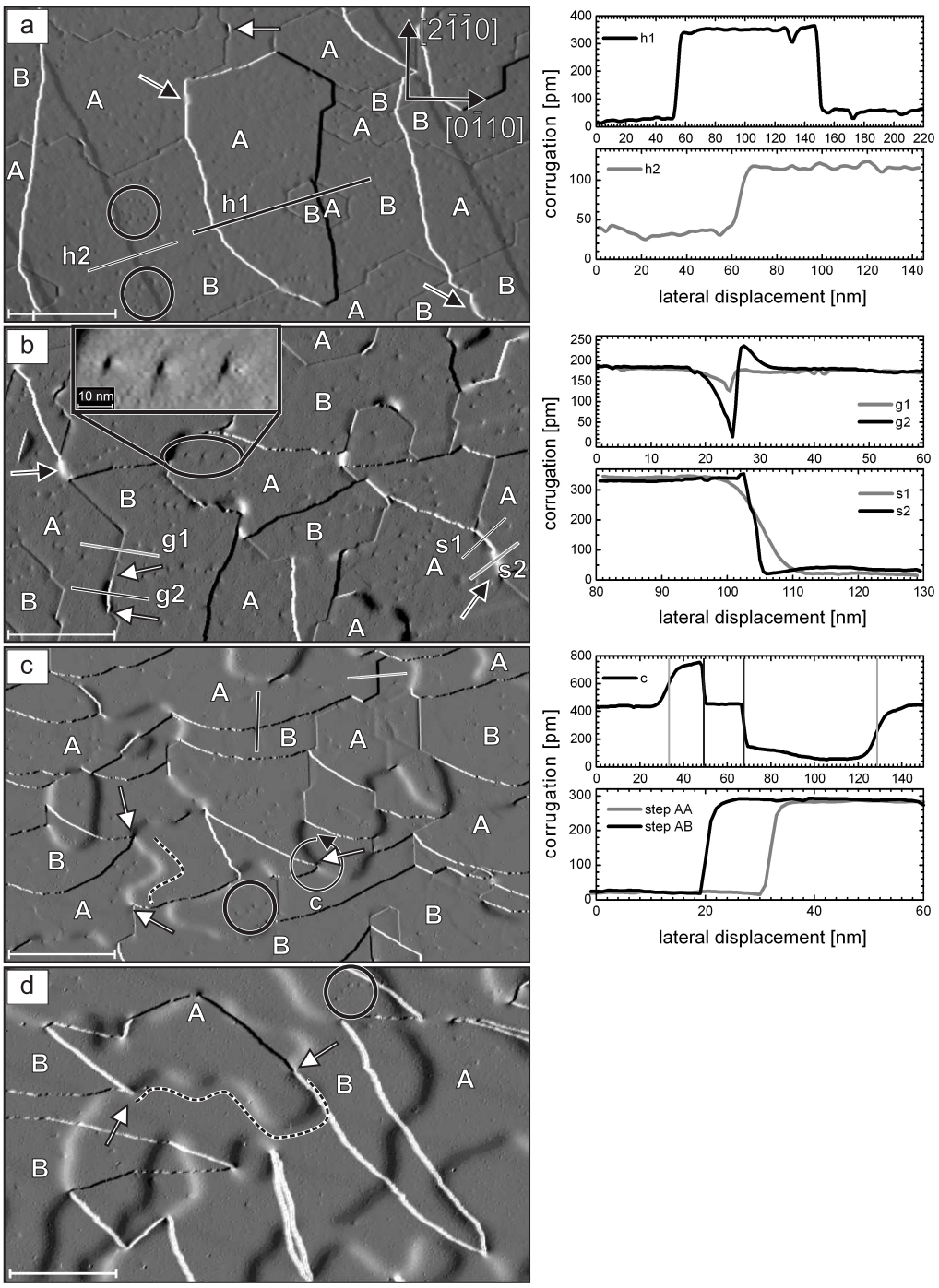

Figure 5.7: Differentiated STM topographs of Dy/W(110) at different film thicknesses Θ: (a) 14 ML, (b) 22 ML, (c) 27 ML, and (d) 45 ML. (scale bar: 100 nm)

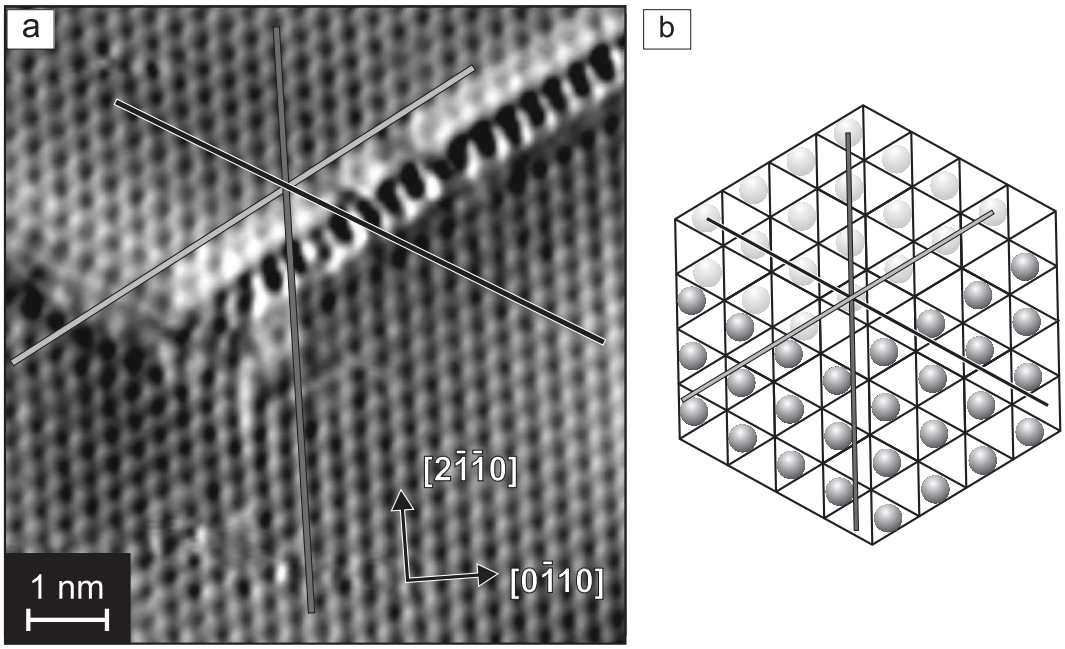

Figure 5.8: (a) Atomically resolved STM topograph of a grain boundary in a 15 ML Dy/W(110) film. The extrapolation of the atomic lattice across the defect line reveals that the Dy patches in the upper and lower part of the image exhibit different stackings. ($T = 40$ K, tunneling parameters: $U = -2.4$ mV, and $I = 100$ nA). (b) Atomic model of a grain boundary between the stackings.

Eventually, at a coverage of about 45 ML the trenches disappear and the surface morphology [see Fig. 5.7 (d)] is dominated by double-screw dislocations (arrows) and smooth step edges (hatched line). Two normal step edges and two smooth step edges depart from every screw dislocation [line section in Fig. 5.7 (c) (right panel)]. The nature of the defects observed in Dy/W(110) films is discussed in the next paragraphs.

The vicinity around a trench is shown in the atomically resolved STM topograph in Fig. 5.8. An extrapolation of the atomic positions from the upper part onto the lower part of the image reveals that the lattice is shifted in all three densely packed directions (see lines in Fig 5.8). These data suggest that the trenches observed on thin Dy films on W(110) are grain boundaries between differently stacked grains.

While Fe on W(110) exhibits pseudomorphism at up to two ML, the first atomic layer in heavy rare earth metals on W(110) forms a slightly distorted hexagonal wetting layer [107, 108]. Relative to the bulk Dy(0001) basal plane,

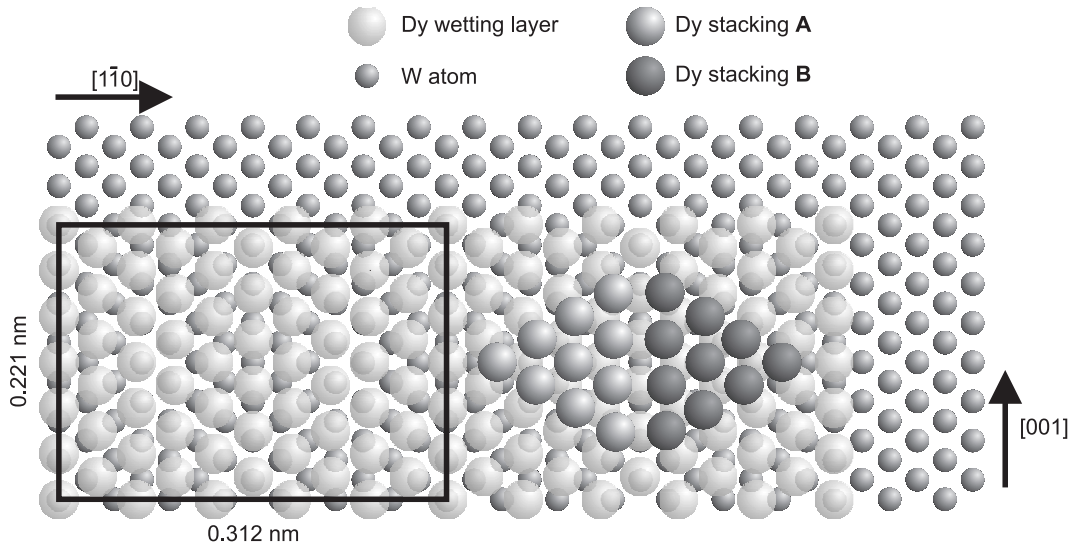

Figure 5.9: Dy/W(110) wetting layer model based on the atomic model proposed in Ref. [107].

the wetting layer is expanded by 1.2% along the W[001] direction and compressed by 0.6% along the W[1$\bar{1}$0] direction. This gives a Dy:W coincidence-lattice match of 6:7 and 5:7 along the W[001] and W[1$\bar{1}$0] directions, respectively [107]. The model in Fig. 5.9 represents the Dy wetting layer following the model proposed in Ref. [107]. On top of this wetting layer there are two possible hexagonal stackings which are energetically equivalent since there is no direct match between the W(110) atomic positions and the wetting layer. The Dy/W(110) films were evaporated at RT, so that just after evaporation, there are numerous crystal nuclei that should be equally distributed between the two possible hexagonal stackings **A** and **B** on the wetting layer (see Fig. 5.9). Further Dy deposition results in the growth of grains with different stacking series that coalesce forming a closed film. Therefore, for an identical local coverage both stakings **A** and **B** can be present at the surface. Consequently, the trenches present at the surface of low coverage samples [see Fig. 5.7 (a)-(c)] are grain boundaries between grains with different stacking series.

There are two possible exposed stackings for identical local coverage, **A** and **B**. The exposed stackings are marked on the STM topographs in Fig. 5.7. The detailed analysis of the stackings allows to distinguish between two types of steps: (i) steps separating adjacent terraces with different stacking and (ii) steps separating terraces with the same stacking [line sections in Fig. 5.7 (c) (right panel)]. The former type of step has an irregular step edge. The latter type of step has

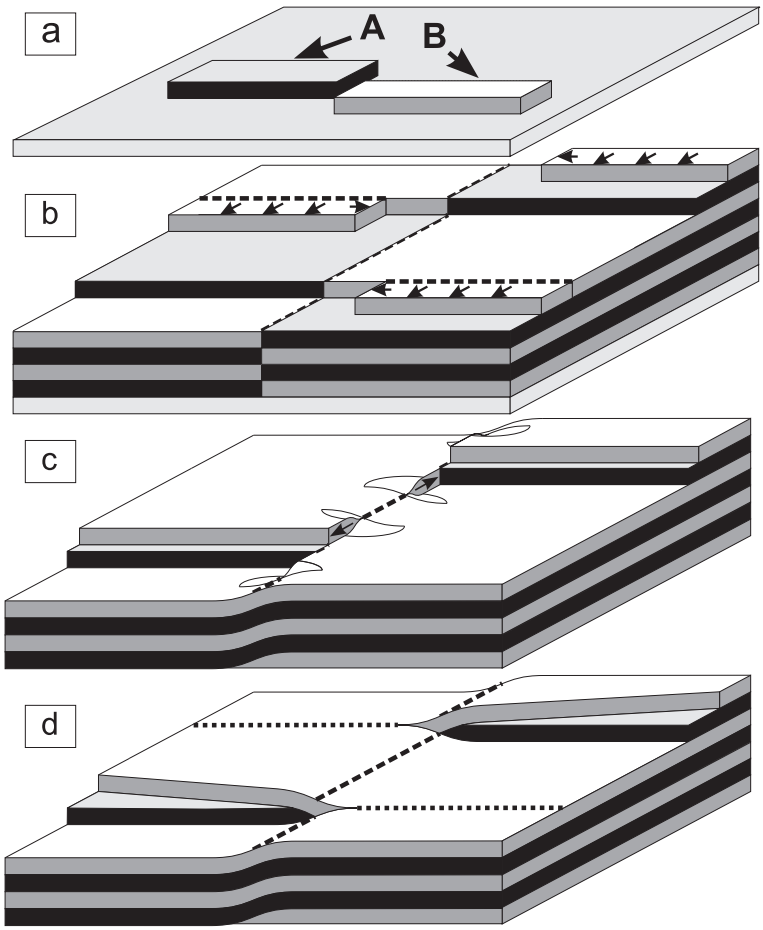

Figure 5.10: The thickness-dependent morphology of Dy films on W(110) can be understood by the following sequence: (a) **A**- and **B**- stacked second layer islands nucleate on the wetting layer. (b) In sufficiently thin films differently stacked patches coexist. They are separated by structural grain boundaries. (c) At a certain critical film thickness the grain boundaries become energetically unfavorable. Two partial screw dislocations form instead. These dislocations depart from each other until they merge with another partial screw dislocation. If the Burgers vectors $\vec{b}$ of both dislocations point in the same direction they from a perfect screw dislocation as shown in (d). Otherwise, the two partial dislocations annihilate.

straight step edges along the close-packed directions and corresponds to the position of the grain boundaries. This second type of step edges is the one that locally smooths out (see black arrows in Fig. 5.7).

Fig. 5.10 shows a thickness-dependent model of Dy/W(110) films. As already mentioned, the nucleation of **A**- and **B**-stacked islands starts with the second

Dy layer [see Fig. 5.10 (a)]. At low film thickness the stacking of the grains is maintained [see Fig. 5.10 (b)]. However, since there are grain boundaries between differently stacked grains, and the penalty energy of the grain boundaries increases with film thickness the grain boundaries are partially relaxed above a critical thickness θ_{crit} [Fig. 5.10 (c)] . This is locally accomplished by the formation of two partial screw dislocations. The asymmetric trenches and the smooth step edges result from this relaxation. Fig. 5.7 (a) indicated $\theta_{\text{crit}} \approx 14$ ML. The Burgers vectors of partial screw dislocations are of equal length but of opposite sign, i.e. $\vec{b} = \pm\frac{1}{2}[0001]$, respectively. As the film becomes thicker the distance between the two partial screw dislocations belonging to the same pair increases. Eventually, the dislocation merges with another partial screw dislocation of an adjacent pair. Hereby, two cases can be distinguished: if the Burgers vectors of the two merging partial screw dislocations are equal they form a perfect screw dislocation with $\vec{b} = [0001]$. As a result two step edges emerge from the point where the dislocation line intercepts with the surface. This situation is schematically represented in Fig. 5.10 (d). Otherwise, if the Burgers vectors have opposite sign, the two partial screw dislocations annihilate leaving a continous smooth step edge.

The surfaces of the Dy/W(110) films in Fig. 5.7 present ensembles of point-like defects (white circle). These defect are characterized by asymmetric depressions [see inset in Fig. 5.7 (b)]. The nature of these defects has been identified by means of atomic resolution scanning tunneling microscopy. The top panel of Fig. 5.11 shows an atomic resolution STM image of the region around one of the point-like defects. The Dy atoms appear as depressions. Along two parallels (arrows) in the parallelogram in Fig. 5.11 line profiles have been taken which are plotted in the bottom panel. If the Dy(0001) surface were undistorted both line profiles should contain the same number of atoms. The comparison, however, reveals an anomaly: while the gray profile exhibits 20 depressions only 19 are observed along the black profile. This observation can only be explained if the defect site is the starting point of an additional semi-infinite plane which propagates to the right of Fig. 5.11(top panel), i.e. an edge dislocation. These edge dislocations are characterized by $\vec{b} = \langle 2\bar{1}\bar{1}0\rangle$. As mentioned before, the Dy films grow on a slightly distorted hexagonal wetting layer that relative to the bulk (0001) basal plane, is expanded 1.2% along the W[001] direction and compressed by 0.6% along the W[1$\bar{1}$0] direction. This misfit produces strain which is partially relaxed by the formation of edge dislocations. The presence of these misfit dislocations has also been reported in other epitaxially grown lanthanide systems such as holmium-yttrium multilayers [109]. Since the energy associated with the misfit dislocations is proportional to the dislocation line length, the density of these defects decreases

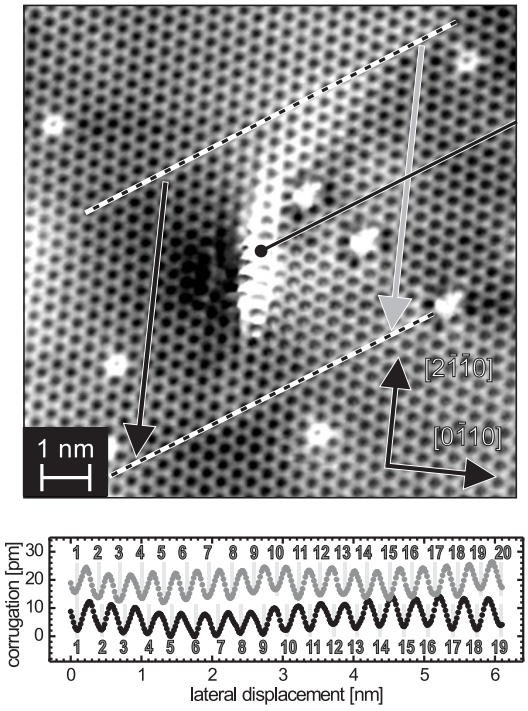

Figure 5.11: (a) Atomically resolved STM topograph (top panel) around a point-like defect in a Dy/W(110) film ($T = 40$ K, tunneling parameters: $U = -3$ mV, and $I = 100$ nA). The line profiles (bottom panel) taken along the two arrows reveal the presence of an edge dislocation with $\vec{b} = [2\bar{1}\bar{1}0]$.

with increasing film thickness (see Fig. 5.7).

In short, screw dislocations and misfit dislocations are present in Dy/W(110) films as a result of the morphology of the wetting layer. The density of these line defects depends on the thickness of the film. At low coverage no screw dislocations are present and there are many misfit dislocations. At high coverage screw dislocations are present but there are fewer misfit dislocations.

5.4 Magnetic contrast of Dy(0001)

The bulk band structure of all trivalent lanthanides is characterized by a local band gap at the Γ point. In Fig. 5.12 the calculated ferromagnetic Dy band structure is plotted (taken from Ref. [110]). In the Dy band structure, at the Γ point the gap between the highest occupied state and the lowest unoccupied state is approximately 2 eV. The calculated spin splitting, defined as the energetic difference between majority and minority spin bands, accounts to $\Delta_{ex} = 0.9$ eV.

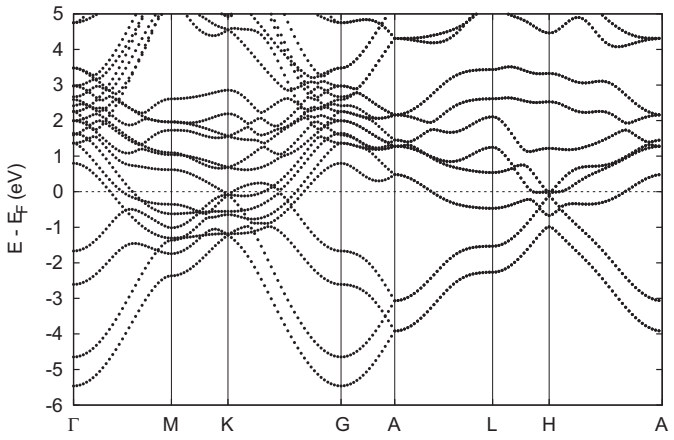

Figure 5.12: Dy bulk band structure calculation with the magnetization in the easy a-axis. The band gap at the Γ point is 2 eV. Data from Ref. [110].

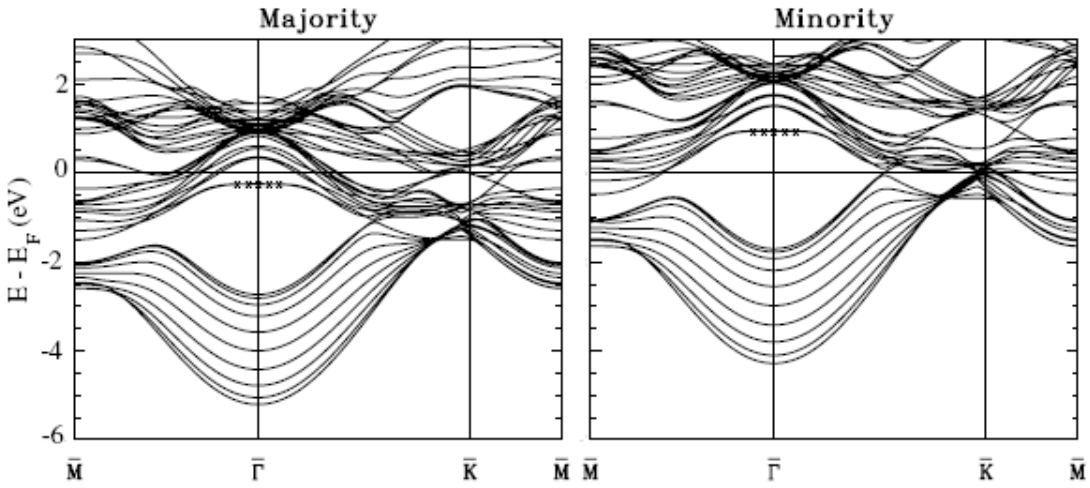

Figure 5.13: Band structure calculation for the Gd(0001) surface. The band structure develops a spin-split surface state that is marked with crosses. The majority surface state (spin parallel to the one of the $4f$ electrons) is located 0.24 eV below E_{F} and the minority surface state is 0.95 eV above E_{F}. Data from Ref. [111].

As introduced in Sec. 5.3, Dy grows epitaxially on W(110) as bulk-like hcp films with Dy(0001) ∥ W(110).

Within the band gap of the (0001) surface-projected bulk band structure of all trivalent lanthanides a $5d_{z^2}$-like surface state can be found at the $\bar{\Gamma}$ point. This surface state has been observed in photoemission and inverse photoemission [113]. It dominates the STS spectra since the d_{z^2} orbital extends far into

the vacuum [114]. The surface state is characterized by a very flat band, i.e. low dispersion. It is strongly localized to the surface layer and decays exponentially into bulk and vacuum. Due to the interaction with the localized $4f$ electrons, the surface state exhibits an exchange splitting that scales with the $4f$ magnetic moment [115]. This exchange splitting results in an occupied state below E_{F} with the spin parallel to the $4f$ spin (majority spin), and an unoccupied minority spin state. In the calculated band structure of the Gd(0001) surface (see Fig. 5.13) the spin-split surface state is located below and above E_F with a spin splitting of $\Delta_{ex} = 1.2$ eV, 0.4 eV larger than found experimentally [114]. For Dy(0001), the majority part of the surface state appears at $E = 102$ meV below $\mathrm{E_F}$ and the minority part at $E = 403$ meV above $\mathrm{E_F}$, at $T = 10$ K [115]. The spin splitting accounts to $\Delta_{ex} \simeq 500$ meV, 0.4 eV smaller than the theoretical bulk value [110].

Fig. 5.14 shows angle-resolved photoemission spectra (ARPES) of Dy/W(110) films taken from Ref. [112]. On the left, the photoemission spectra shows the electronic states of the valence-band. Near the Fermi level the majority part of

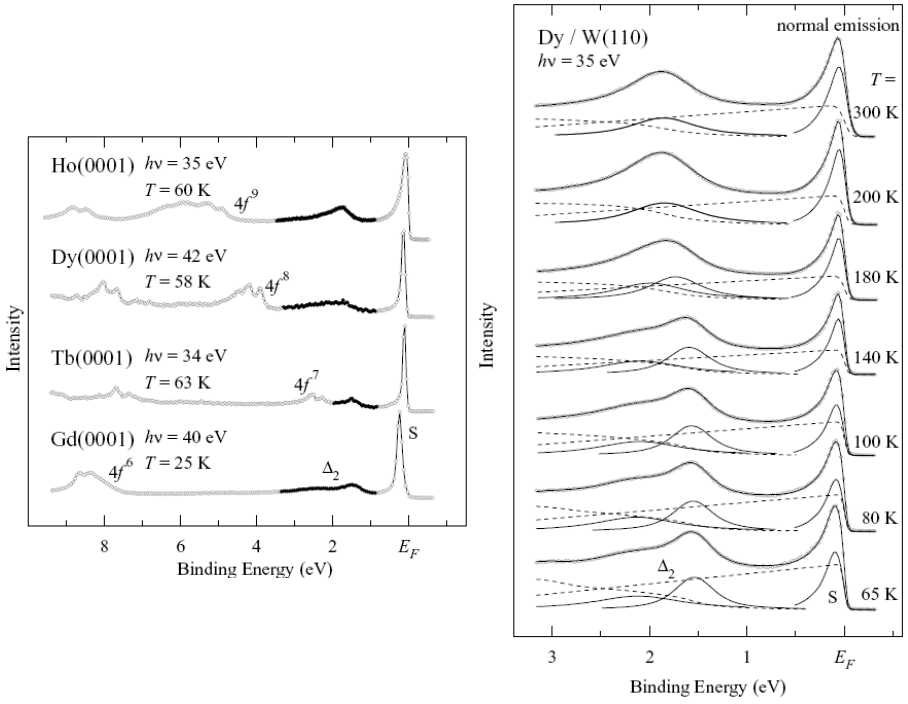

Figure 5.14: Angle-resolved photoemission spectra of Dy films grown on W(110). On the left, photoemission spectra showing the valence-band electronic states. On the right, valence-band photoemission spectra of Dy metal measured at various temperatures, showing the temperature dependence of the Δ_2 band. Data from Ref. [112]

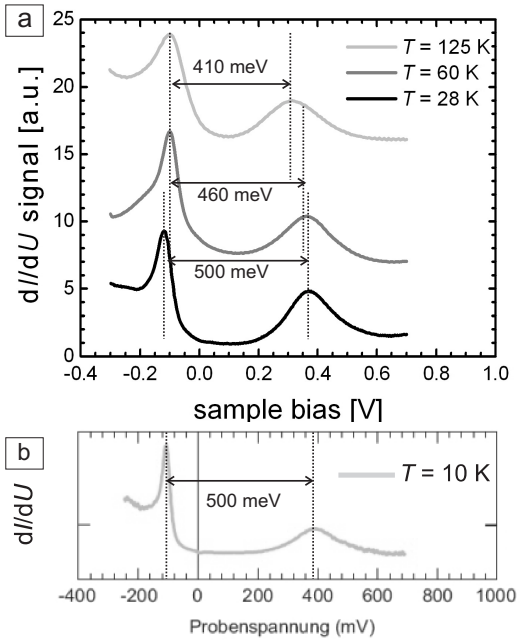

Figure 5.15: (a) $\mathrm{d}I/\mathrm{d}U$ spectra of Dy(0001) taken with bare W tips at $T = 28$ K, $T = 60$ K, and $T = 125$ K. The majority and minority parts of the $\bar{\Gamma}_{d_{z^2}}$ surface state appear as narrow peaks below and above E_F, respectively. The exchange splitting decreases monotonously with increasing temperature. (b) $\mathrm{d}I/\mathrm{d}U$ spectrum of Dy(0001) at a temperature of $T =$ 10 K from Ref. [115].

the surface state appears. The $4f$ final-state multiplet appears at a binding energy of ≈ 4 eV. In the binding energy range of 0.8 eV to 3.0 eV, the Dy spectra are dominated by the Δ_2 band. The Δ_2 band is a bulk band that is spin split at the Γ point due to interaction with the localized $4f$ states [116, 117]. The temperature dependence of the exchange splitting of the Δ_2 band is shown in Fig. 5.14(right panel). The lower lying part of the Δ_2 band is centered at ≈ 1.5 eV below the Fermi level but it is broadened by about 1 eV.

Fig. 5.15 (a) shows spin-averaged $\mathrm{d}I/\mathrm{d}U$ spectra of the Dy(0001) surface taken on a 45 ML Dy/W(110) film at different temperatures, $T = 28$ K, $T = 60$ K, and $T = 125$ K, corresponding to 1/3, 3/4, and 3/2 of T_C, respectively. The spectra were acquired with a bare W tip. The plotted spectra are the average over about 50 measured spectra. All of them show the typical two peaks structure of the (0001) surface of the trivalent lanthanides. The majority and the minority parts of the surface state appear at $E \simeq -100$ meV and $E \simeq 400$ meV, respectively. The exchange splitting of the surface state decreases with increasing temperature, mainly due to the displacement of the minority part of the surface state towards $\mathrm{E_F}$. For comparison similar measurements on Dy/W(110) obtained at 10 K by D. Wegner [62] are shown in Fig. 5.15 (b). Although our spectra have larger peak widths due to the higher measurement temperatures, the energy position of

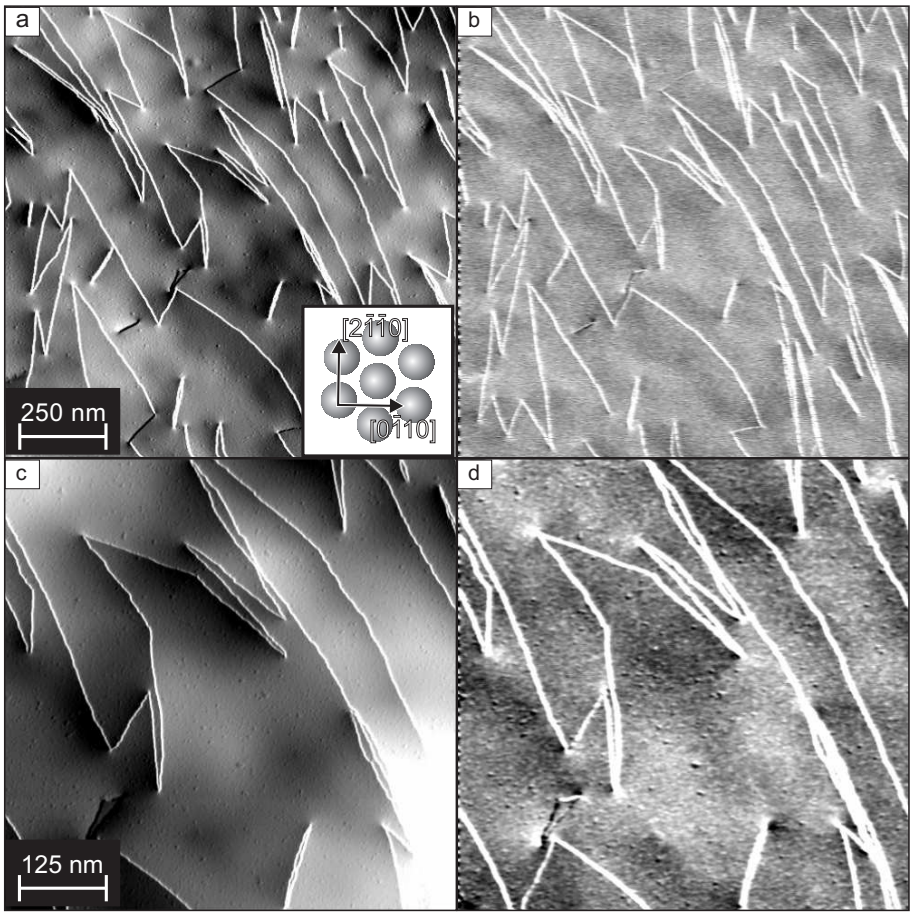

Figure 5.16: STM topographs (left panels) and spin-averaged dI/dU-maps (right) on a 90 ML Dy/W(110) film taken with a bare W tip. A slight electronic contrast is present around the screw dislocations ($T = 60$ K, tunneling parameters: $U = -0.2$ V, and $I = 15$ nA).

the surface state and the exchange splittings are almost identical to the results obtained at 10 K. Therefore, it is clear that the surface state does not change much well below T_C. The dependence of the exchange splitting of the surface state in Tb(0001) has been studied by STS [118]. The authors found a reduction of the exchange splitting with increasing temperature, consistent with the results presented here for Dy.

Fig. 5.16 shows STM topographs (left panels) and spin-averaged dI/dU-maps (right) of a 90 ML Dy/W(110) film taken with a bare tungsten tip. A weak electronic contrast is observed around the core of the screw dislocations. It can be attributed to the stress field around the dislocation which decreases with the

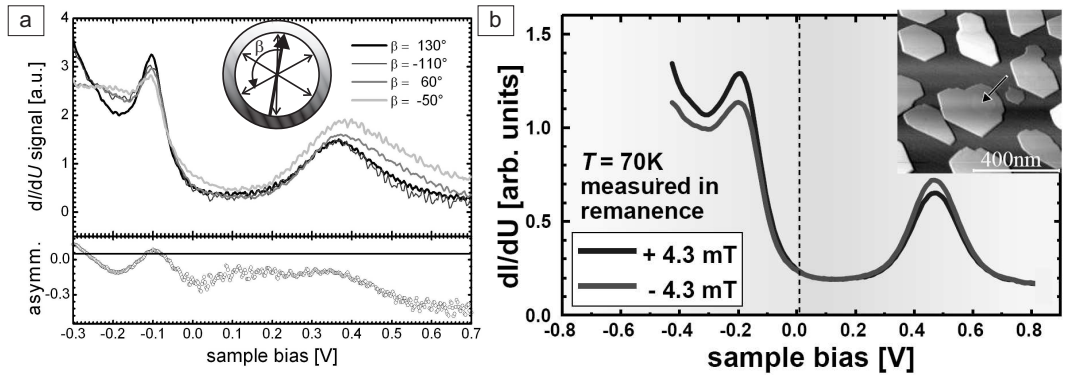

Figure 5.17: (a) SP-STS spectroscopy (top panel) on four different domains in a 60 ML Dy/W(110) film. β indicates the angle between $\vec{m}_{\mathrm{s}}$ and $\vec{m}_{\mathrm{t}}$. The bottom panel shows the asymmetry between $\beta = 130°$ and $\beta = -50°$ domains. ($T = 60$ K, $U_{\mathrm{stab}} = -0.3$ V, and $I_{\mathrm{stab}} = 15$ nA) (b) SP-STS spectroscopy on Gd/W(110) islands after saturation in opposed out-of-plane directions. Taken from Ref. [114].

inverse of the distance to the dislocation core [119].

SP-STM on Dy/W(110) films reveals six-fold in-plane magnetic contrast corresponding to six different domains at the surface. Fig. 5.17 (a) (top panel) shows the SP-STS spectra on four of the six possible domains on a 90 ML Dy/W(110) film acquired with a spin-sensitive Dy-coated tip. The spectra show the spin-split surface state at the same position. The relative intensity of the majority and minority parts of the surface state scales with the projection of the surface local magnetization, $\vec{m}_{\mathrm{s}}$, onto the tip magnetization, $\vec{m}_{\mathrm{t}}$, as expected from Eq. 2.14. For comparison Fig. 5.17 (b) shows the SP-STS spectra of the surface state of Gd/W(110) [114]. The asymmetry A calculated after Eq. 4.1 [see Fig. 5.17 (a) (bottom panel)] amounts to 15% and 30% at the position of the majority part and minority part of the surface state, respectively. The maximum magnetic contrast in SP-STM is expected at the position of the spin-split surface state as observed for Gd/W(110) [114]. However, to our experience better contrast is obtained at a bias voltage between $U = -1$ V and $U = -0.6$ V.

In order to understand the origin of the large contrast at high negative bias, spectra with a larger bias range (-2 V $\leq$ U $\leq +0.8$ V) have been investigated. Fig. 5.18 (a) shows a typical spectrum of the Dy(0001) surface taken with a non-magnetic W tip. The spectrum is dominated by the surface state, and there is only a small feature around $U = -0.75$ V. At high negative sample bias a monotonously increasing $\mathrm{d}I/\mathrm{d}U$ signal is observed. Fig. 5.18 (b)-(c) shows spectra taken with different Dy-coated tips on different samples. Both sets of spectra are dominated

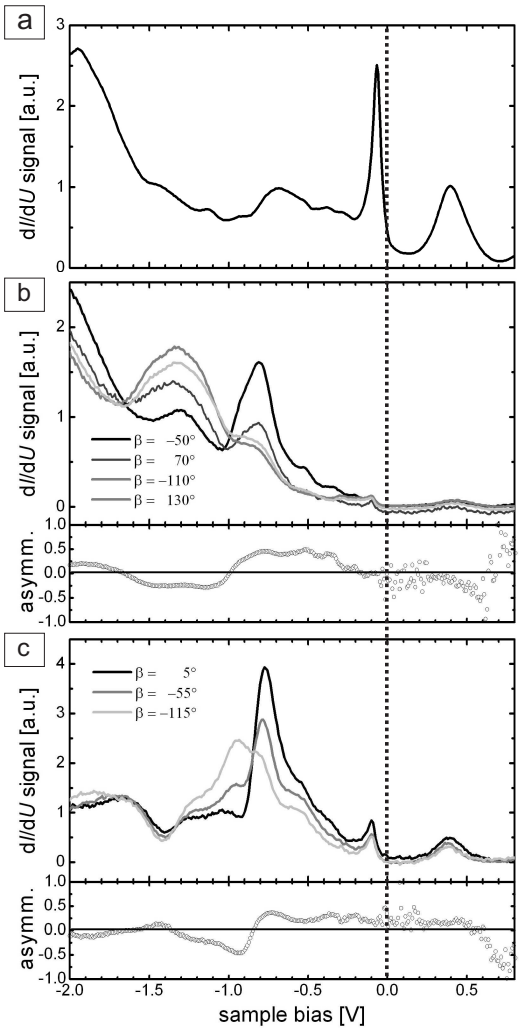

Figure 5.18: SP-STS spectroscopy on 90 ML Dy/W(110) films using different tips ($T = 52$ K and $U_{\mathrm{stab}} = -2$ V). β indicates the angle between $\vec{m}_{\mathrm{s}}$ and $\vec{m}_{\mathrm{t}}$. (a) STS spectrum with a bare W tip. $I_{\mathrm{stab}} = 45$ nA. (b) SP-STS spectra (top panel) with a Dy-coated tip on four domains with different $\vec{m}_{\mathrm{s}}$ and asymmetry (bottom) between the spectra from $\beta = -50°$ and $\beta = 130°$ ($I_{stab} = 45$ nA) (c) SP-STS spectra (top) with a Dy-coated tip on three domains with different $\vec{m}_{\mathrm{s}}$ and asymmetry (bottom) between the spectra from $\beta = 5°$ and $\beta = -115°$ ($I_{stab} = 40$ nA).

by strongly polarized peaks around $U = -0.8$ V. These structures are typical for all the spectra taken with Dy-coated tips, although the position of the "main" peak varies between $U = -0.9$ V and $U = -0.7$ V. Values as high as $A = 50\%$ at the "main" peak position are frequently measured. However, no sample electronic state is present at -0.8 eV below the Fermi level as shown by the ARPES spectra in Fig. 5.14. Although the lower lying part of the Δ_2 band is centered approximately 1.5 eV below the Fermi level, this feature is not observed in the STS spectra. Since the Δ_2 band is a bulk state, it probably decays strongly into the vacuum resulting in a vanishing DOS at the tip position. It is clear that the observed feature does not correspond to the Δ_2 band. Another possible origin of the observed electronic states is the presence of strongly polarized states in the small Dy clusters on the tips. The electronic structure of these states would depend on the cluster shape resulting in the shift of the "main" peak observed for different tips. It is also well

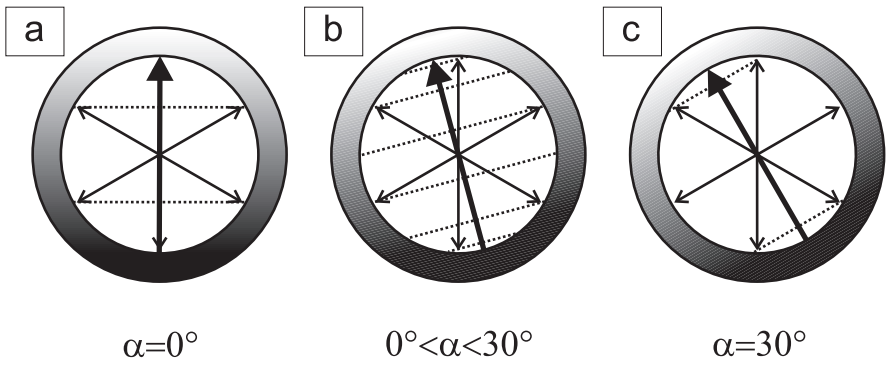

Figure 5.19: Schematic representation of the possible orientations of $\vec{m}_t$ with respect to $\vec{m}_s$. The thin arrows represent the six possible $\vec{m}_s$ directions along the $\langle 2\bar{1}\bar{1}0\rangle$ easy axes, while the thick arrow represents $\vec{m}_t$. (a) $\alpha = 0°$, resulting in four contrast levels. (b) $0° < \alpha < 30°$, resulting in six contrast levels. (c) $\alpha = 30°$, resulting in three contrast levels.

known that the tip electronic structure dominates the STS spectra at negative bias voltage [120].

The number of contrast levels observed by magnetic $\mathrm{d}I/\mathrm{d}U$-mapping depends on the relative orientation of $\vec{m}_t$ with respect to $\vec{m}_s$. For a magnetic sixfold surface, the three possible relations are schematically drawn in Fig. 5.19. α is the angle between $\vec{m}_t$ and $\vec{m}_s$ for the domain with the largest $\mathrm{d}I/\mathrm{d}U$-signal. If $\alpha = 0°$, i.e. $\vec{m}_t$ is parallel the magnetization of one domain, the magnetic $\mathrm{d}I/\mathrm{d}U$ maps assume four different contrast levels as schematically shown in Fig. 5.19 (a). The two "gray" levels correspond to two domain types where the respective $\vec{m}_s$ form an angle of 120°, respectively. If $\alpha = 30°$, i.e. $\vec{m}_t$ lies along a sample´s hard axis, the magnetic $\mathrm{d}I/\mathrm{d}U$ maps only have three contrast levels. In this case each contrast level belongs to two domain types as schematically represented in Fig. 5.19 (c). In the intermediate case, where $0° < \alpha < 30°$ [see Fig. 5.19 (b)], six different contrast levels corresponding to the six different $\vec{m}_s$ directions are obtained.

Fig. 5.20 shows examples of $\mathrm{d}I/\mathrm{d}U$-maps resulting in six (b) and three (e) contrast levels. The histogram of the intensity of the $\mathrm{d}I/\mathrm{d}U$-signal in Fig. 5.20 (b) is plotted in Fig. 5.20 (c). Six peaks can be clearly recognized. The peaks are labelled *i*-*vi* from lowest to highest intensity of the $\mathrm{d}I/\mathrm{d}U$ signal. As schematically shown in the inset of Fig. 5.20 (c) $\vec{m}_t$ is tilted by α with respect to domain *vi* which in total leads to six different projections of $\vec{m}_s$ onto $\vec{m}_t$. Considering the sixfold symmetry of the Dy(0001) surface, it is possible to conclude that $\vec{m}_s$ of domain *i* forms an angle of ±60° with $\vec{m}_s$ of domains *ii* and *iii*, ±120° with $\vec{m}_s$ of

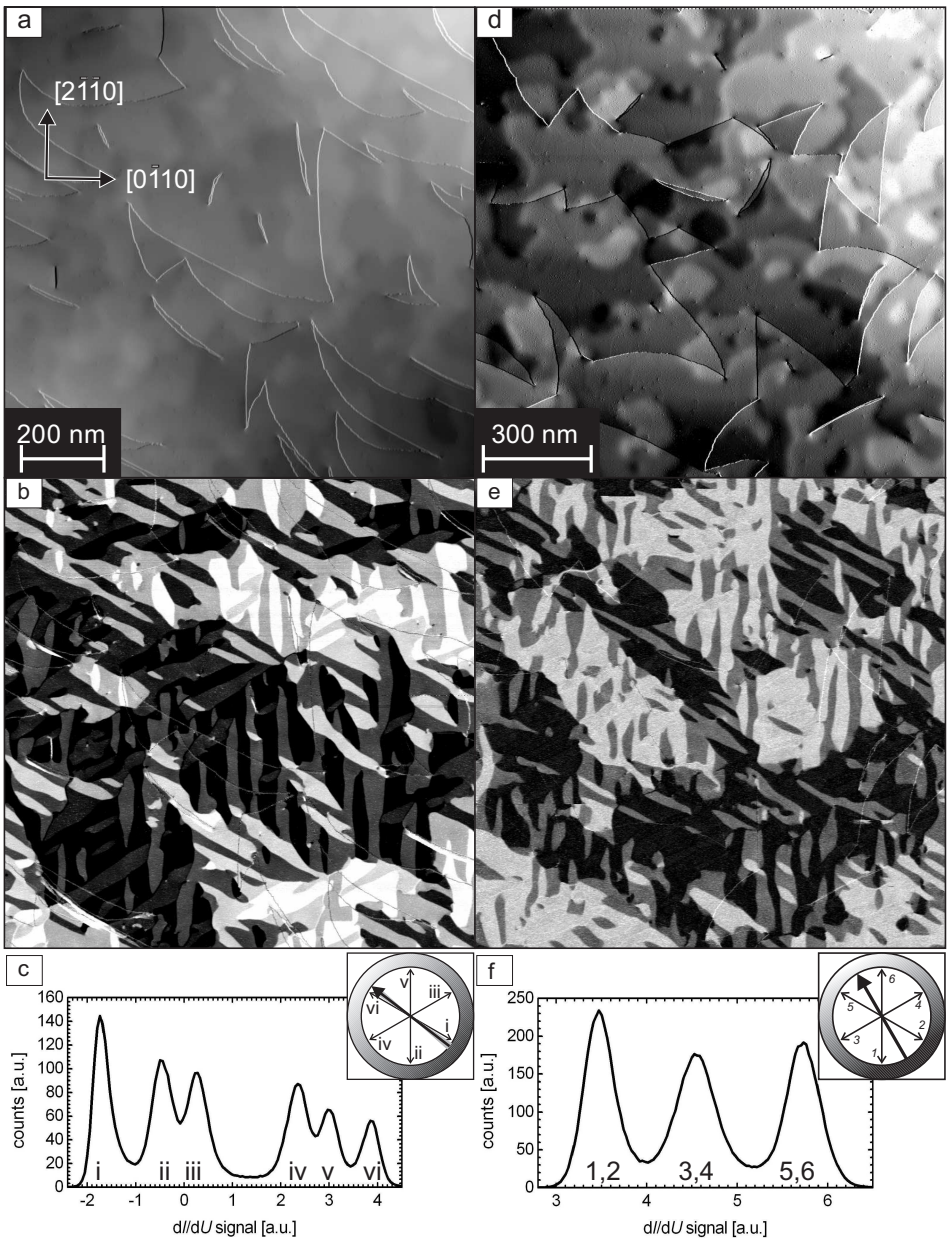

Figure 5.20: (a) STM topograph of a 90 ML Dy/W(110) film. (b) The spin-resolved dI/dU-map reveals six magnetic contrast levels. (c) Histogram of the dI/dU-map (T = 25 K, Dy-coated tip, tunneling parameters: $U = -1.0$ V, and I = 30 nA). (d) STM topograph of a 135 ML Dy/W(110) film. (e) The dI/dU-map shows only three contrast levels. (f) Histogram of the dI/dU-map at (e)($T = 60$ K, Dy-coated tip, tunneling parameters: $U = -0.2$ V and $I = 15$ nA).

Domain index	$\frac{\mathrm{d}I}{\mathrm{d}U}$ [a.u.]	$\frac{\mathrm{d}I}{\mathrm{d}U_{\mathrm{SP}}}$ [a.u.]
i	-1.74 ± 0.02	-2.96 ± 0.05
ii	-0.449 ± 0.013	-1.66 ± 0.04
iii	0.262 ± 0.012	-0.95 ± 0.04
iv	2.36 ± 0.02	1.14 ± 0.05
v	2.99 ± 0.02	1.77 ± 0.05
vi	3.88 ± 0.02	2.66 ± 0.05

Table 5.1: Analysis of the $\mathrm{d}I/\mathrm{d}U$-signal intensity in Fig. 5.20 (b).

domains *iv* and *v*, and is opposed to $\vec{m}_{\mathrm{s}}$ of domain *vi*. In order to calculate α, the values of the $\mathrm{d}I/\mathrm{d}U$-signal intensity are analyzed. The values of the $\mathrm{d}I/\mathrm{d}U$-signal intensity for the six domains are summarized in Tab. 5.1.

On the basis of Eq. 2.14, the magnetic $\mathrm{d}I/\mathrm{d}U$-signal can be decomposed in a spin-averaged part, $\mathrm{d}I/\mathrm{d}U_{\mathrm{SA}}$, and a spin-dependent part, $\mathrm{d}I/\mathrm{d}U_{\mathrm{SP}}$. The spin-dependent part is proportional to the projection of $\vec{m}_{\mathrm{s}}$ onto $\vec{m}_{\mathrm{t}}$. For the $\mathrm{d}I/\mathrm{d}U$ signal values in Tab. 5.1, $\mathrm{d}I/\mathrm{d}U_{\mathrm{SA}}$ is calculated as their arithmetic average, $\mathrm{d}I/\mathrm{d}U_{\mathrm{SA}} = 1.22 \pm 0.03$ a.u. The values for the spin dependent part of the six domains in Fig. 5.20 (c) are summarized in Tab. 5.1.

For constant tip-sample distance, i.e. in the case of vanishing polarization of the *total* tunneling current, the absolute value of $\mathrm{d}I/\mathrm{d}U_{\mathrm{SP}}$ for domains with opposite polarization, e.g. domains *i* and *vi* in Tab. 5.1, should be equal. However, the tip-sample distance is slightly different on domains with different $\vec{m}_{\mathrm{s}}$, due to the different polarization of the total tunneling current. This effect introduces a small error in the calculation of α. From Eq. 2.14, $\mathrm{d}I/\mathrm{d}U_{\mathrm{SP}}$ results in:

$$\frac{\mathrm{d}I}{\mathrm{d}U}_{\mathrm{SP}}(a) \propto \vec{m}_{\mathrm{s}}(a) \cdot \vec{m}_{\mathrm{t}}, \tag{5.2}$$

where $\mathrm{d}I/\mathrm{d}U_{\mathrm{SP}}(\mathrm{a})$ is the spin-averaged part of the $\mathrm{d}I/\mathrm{d}U$ signal for domain *a*. Then

$$\frac{\frac{\mathrm{d}I}{\mathrm{d}U}_{\mathrm{SP}}(a)}{\frac{\mathrm{d}I}{\mathrm{d}U}_{\mathrm{SP}}(b)} = \frac{\vec{m}_{\mathrm{s}}(a) \cdot \vec{m}_{\mathrm{t}}}{\vec{m}_{\mathrm{s}}(b) \cdot \vec{m}_{\mathrm{t}}} = \mathrm{F}(\alpha) \tag{5.3}$$

only depends on the angle between $\vec{m}_{\mathrm{s}}$ in domains *a* and *b* which can be inferred from symmetry considerations and α.

The value of α calculated with Eq. 5.3 from the values in Tab. 5.1 is $\alpha = 8 \pm 4°$. This result is drawn schematically in Fig. 5.20 (c) where $\vec{m}_{\mathrm{t}}$ and $\vec{m}_{\mathrm{s}}$ are indicated by the arrows. The shaded regions mark the uncertainty in α.

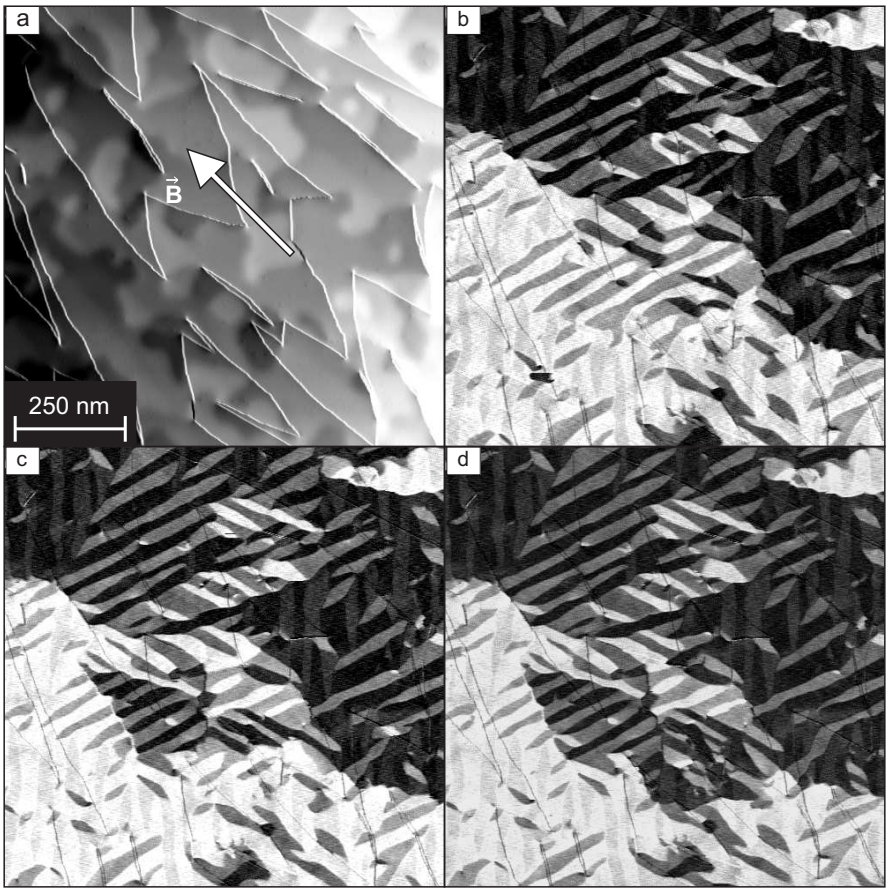

Figure 5.21: (a) STM topograph of a 90 ML Dy/W(110) film. (b) The spin-resolved dI/dU-map shows the magnetic virgin state of the surface. (c) Magnetic structure of the Dy film after several pulses produced by the Helmholtz coil. The arrow in (a) shows the direction of the magnetic field. New domains appear in the middle of the studied area. (d) Magnetic structure of the Dy film after more magnetic pulses (T = 58 K, Dy-coated tip, tunneling parameters: $U = -0.6$ V and $I = 30$ nA).

Fig. 5.20 (e) shows an example of a dI/dU-map taken with a tip where $\vec{m}_{\mathrm{t}}$ lies along one hard axis of the Dy(0001) surface resulting in three contrast levels. In Fig. 5.20 (f) the histogram of the dI/dU-signal in Fig. 5.20 (e) and the schematic representation of $\vec{m}_{\mathrm{t}}$ and $\vec{m}_{\mathrm{s}}$ are shown. The "white" contrast corresponds to domains *5* and *6*, the "gray" contrast to domains *3* and *4*, and the "black" contrast to domains *1* and *2*. The "white" and "black" contrasts are distributed either alternatingly with "gray" contrast, or in larger patches. However, the "gray" contrast appears only as stripes alternating with "black" or "white" contrast, as there is an angle of 180° between $\vec{m}_{\mathrm{s}}$ of the two corresponding domains.

In order to fully demonstrate the magnetic origin of the observed $\mathrm{d}I/\mathrm{d}U$ contrast, two coils in a Helmholtz configuration were situated outside the STM chamber to produce magnetic pulses. The Helmholtz pair consists of two identical circular magnetic coils that are placed symmetrically one on each side of the sample along a common axis, and separated by a distance equal to the radius of the coil. Each coil has $N = 300$ turns and a radius $r \simeq 12$ cm. The value of the magnetic field at the sample position in-plane with respect to the sample surface can be calculated as:

$$\vec{B}_{\max} = \frac{8\mu_0 N I_{\max}}{5\sqrt{5}r}, \tag{5.4}$$

where μ_0 is the magnetic permeability of vacuum and $I_{\max}$ the maximum current through the coil.

The current is produced by discharging a capacitor array with a capacitance of $C = 90$ mF loaded, with $V = 220$ V, through the coils that have a resistance of $R = 3\ \Omega$ and an inductance of $L = 0.2$ H. From the equations for a series RLC circuit [121], the maximum current is obtained, $I_{\max} = 57$ A. This results in a magnetic field of $\vec{B} = 0.12$ T in the surface plane.

Fig. 5.21 shows the STM topograph (a) as well as the magnetic $\mathrm{d}I/\mathrm{d}U$-maps of the sample remanent state (b) and after several magnetic field pulses (c)-(d) applied by the Helmholtz pair. The magnetic field pulse only results in minor changes of the spin structure as can be seen in Fig. 5.21 (c)-(d). Obviously, the sample is magnetically very hard. However, it is demonstrated that the contrast is magnetic in origin.

5.5 Domain structure of ferromagnetic Dy/W(110) films

According to Refs. [112, 122, 123], the magnetic structure of crystalline Dy films grown epitaxially on W(110) presents the same magnetic phases as bulk dysprosium. Nevertheless, so far, the domain structure of Dy/W(110) films has not been studied with techniques of sufficient lateral resolution. In this section, several aspects of the magnetic structure of ferromagnetic Dy/W(110) films are discussed. The section begins with a thickness-dependent study of the magnetic structure (Sec. 5.5.1). The magnetic easy axes at the surface and the domain wall properties are discussed in Sec. 5.5.2. Sec. 5.5.3 deals with the interplay of line defects and the magnetic structure. The presence of more complex magnetic structures is demonstrated in Sec. 5.5.4. Finally, SP-STM data that indicates non-collinear magnetism in Dy-coated probe tips are presented.

5.5.1 Film thickness dependence of the domain structure of ferromagnetic Dy/W(110) films

As it was shown in Sec. 5.3, the morphology of Dy/W(110) depends strongly on the film thickness. Consequently, the magnetic structure is expected to be influenced by the thickness-dependent morphology. In this section, the ferromagnetic domain structure of Dy/W(110) films at different thicknesses is discussed.

Continuous films with coverage from $\Theta = 14$ ML to $\Theta = 450$ ML were prepared and subsequently studied by SP-STM at temperatures well below the bulk T_{C}. As shown in the following, the domain structure depends strongly on the film thickness and especially on the density of line defects produced during the growth of the films (see Sec. 5.3).

Fig. 5.22 shows STM topographs (left panels) and magnetic $\mathrm{d}I/\mathrm{d}U$ maps (right) of Dy/W(110) films in a wide coverage range. As introduced in Sec. 5.3, thin films are characterized by terraces divided by grain boundaries and a high density of misfit dislocations, while thicker films are characterized by perfect screw dislocations and fewer misfit dislocations. The analysis of the histograms of the $\mathrm{d}I/\mathrm{d}U$-signal intensity in Fig. 5.22 reveals that in the coverage range studied the surface has sixfold magnetic symmetry. Obviously, the surface of the films is ferromagnetically coupled. However, the domain structure varies with coverage. The domain size increases with increasing film thickness from about 15×40 nm^2 at 14 ML [Fig. 5.22 (a)] to about 40×270 nm^2 at 450 ML [Fig. 5.22 (g)]. The domains are always elongated along the close-packed directions. The possible origin of the domain size increase is the energy associated with the domain wall formation. The domain wall energy is proportional to its area. Therefore, if the domain wall crosses the whole film, larger domains with fewer domain walls are favored for thicker films.

The domain structure of thicker films [Fig. 5.22 (e)-(g)] is characterized by a striped domain pattern, i.e. $\vec{m}_{\mathrm{s}}$ of adjacent domains is successively rotated by $\pm 60°$. The magnetic structure of thinner films is more complex. The magnetic domains differ strongly in shape and size. However, it is possible to distinguish some long-range order, as areas with prevailing bright or dark domains are formed. This also indicates a preference for low angle magnetic domain walls in thin films.

It is clear that larger scan areas are needed to understand the domain pattern of thicker films. Fig. 5.23 (a) shows the topography and the magnetic structure of a 4×4 μm^2 area of a 450 ML Dy/W(110) film. The positions of the smooth step edges in the topography (left panel) reveal where the grains of the film are located. The magnetic structure is characterized by a striped domain pattern.

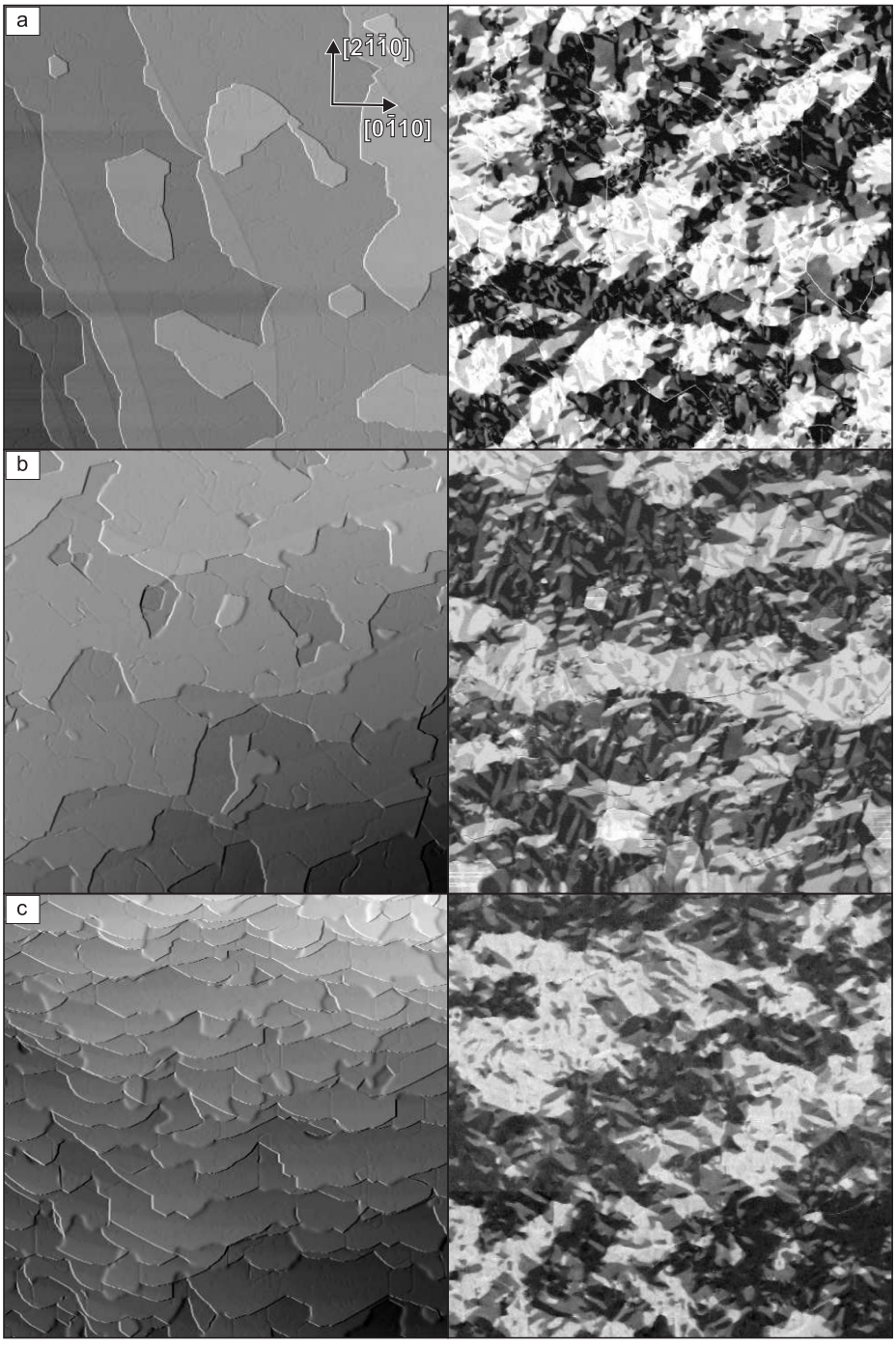

Figure 5.22: Overview of the growth (left panels) and the domain structure (right) of Dy/W(110) films (image size: $1 \times 1\,\mu\mathrm{m}^2$). (a) 14 ML at $T = 60$ K. (b) 23 ML at 59 K. (c) 27 ML at 58 K. This figure is continued on the next page.

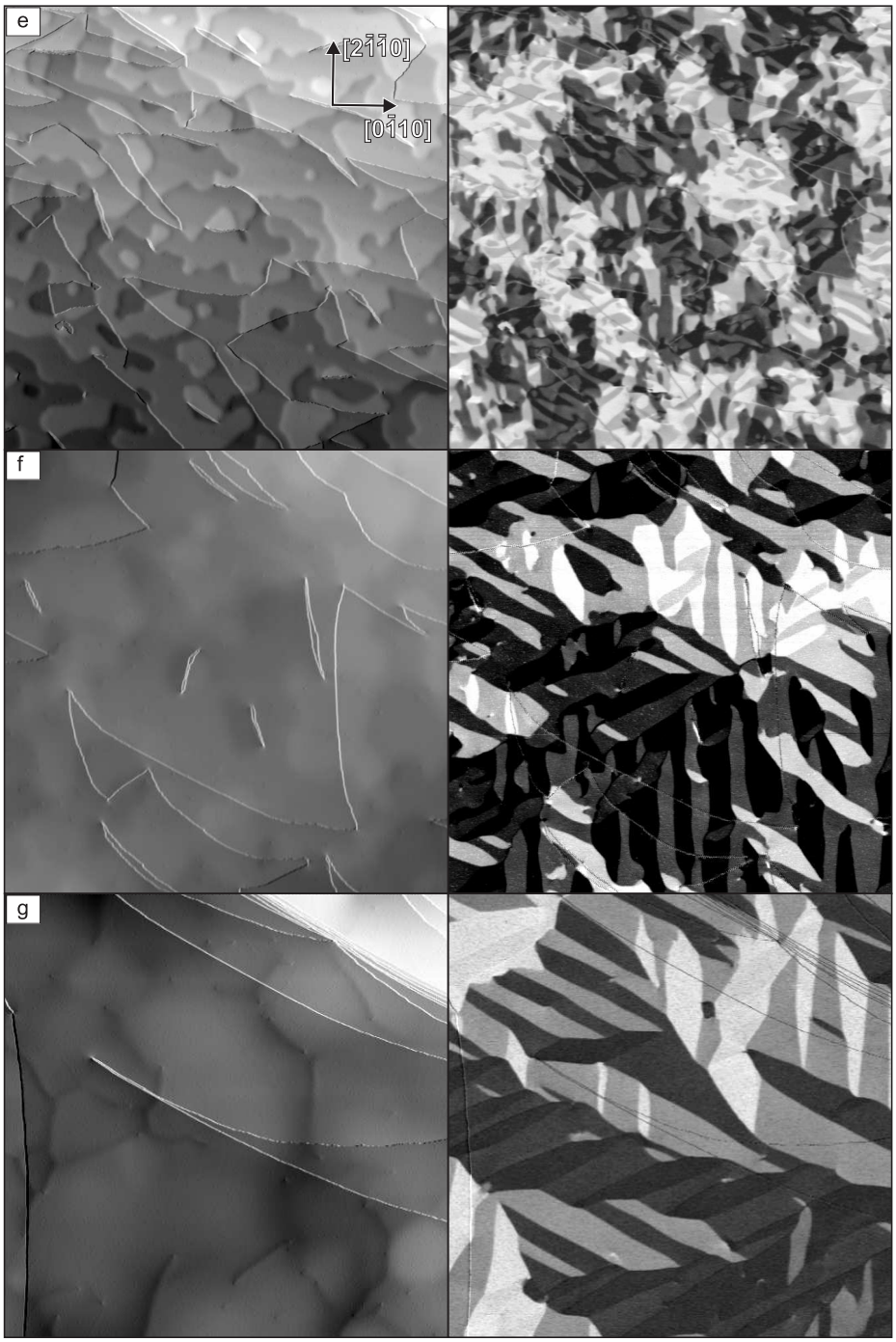

Figure 5.22 (continued): (d) 45 ML at $T = 60$ K. (e) 90 ML at 25 K. (e) 450 ML at 60 K.

As mentioned above, two types of domains whose $\vec{m}_s$ differ by 60° alternate. Therefore, they are separated by internal 60° domain walls. These structures are as long as 800 nm. The lateral size of the domains perpendicular to internal domain walls is very regular, about 40 nm. Probably, the large magnetostriction results in a limited and regular domain size. In contrary, the domain size parallel to the internal domain wall varies strongly. Furthermore, in Fig. 5.22 (f) we can observe the structure of boundaries between two adjacent striped domain patterns which exhibits a zigzag shape. A detailed analysis of the domain walls at this boundary reveals that both 60° domain walls and 120° domain walls are present at these edges. It is introduced below, that both types of domain walls run along preferred directions. This results in the zigzag shape present at boundaries between adjacent striped domain patterns.

5.5.2 Analysis of domain structure and domain walls of ferromagnetic Dy/W(110) films

The well-ordered domain structure of thick Dy/W(110) films allows a detailed study of $\vec{m}_s$. As mentioned before, adjacent domains are mostly separated by 60° domain walls. For a domain with a specific $\vec{m}_s$, only two 60° domain walls are possible, namely with a ±60° rotation of $\vec{m}_s$ to the adjacent domain. These two possible 60° domain walls run along close-packed directions [see Fig. 5.7 (d)-(f)].

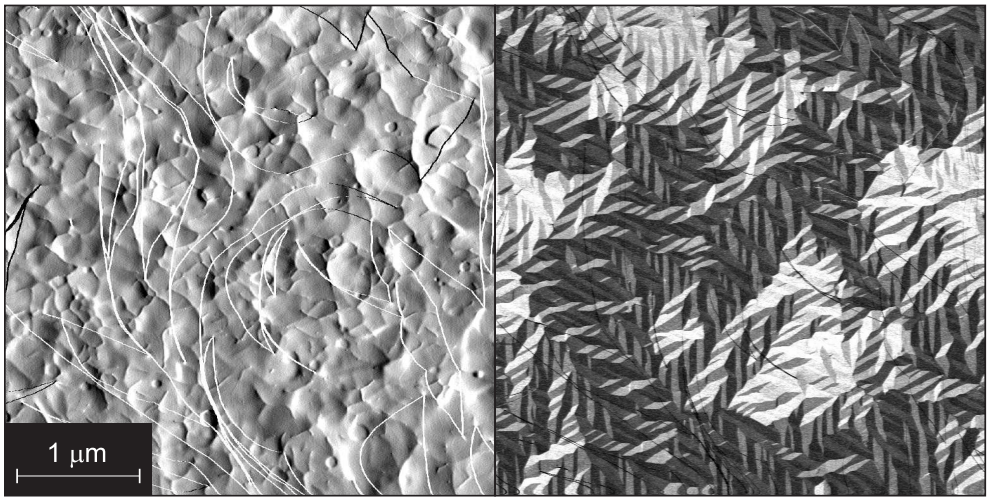

Figure 5.23: Differentiated STM topograph (left panel) and magnetic dI/dU-map (right) of a 4×4 μm^2 area of a 450 ML Dy/W(110) film ($T = 60$ K, Dy-coated tip, tunneling parameters: $U = -0.6$ V and $I = 30$ nA).

The direction of the 60° domain walls is used to determine $\vec{m}_s$ of the domains. Starting from Maxwell's equations, the magnetic charge σ_s at an interface between two regions with magnetizations $\vec{m}_1$ and $\vec{m}_2$ can be calculated as:

$$\sigma_s = \vec{n} \cdot (\vec{m}_1 - \vec{m}_2), \tag{5.5}$$

where $\vec{n}$ is the interface normal. At this moment, we consider atomically sharp interfaces. The internal structure of the domain wall may also result in the formation of magnetic charges. In this framework, the condition for the formation of an energy free magnetic interface is the absence of magnetic charges (page 119 in Ref. [124]):

$$\vec{n} \cdot (\vec{m}_1 - \vec{m}_2) = 0. \tag{5.6}$$

On the basis of this condition, it can safely be concluded that the easy axes of the Dy(0001) are along the $\langle 2\bar{1}\bar{1}0 \rangle$ directions and coincide with the bulk easy axes. For example, Fig. 5.24 shows the magnetization directions of a 90 ML Dy/W(110) film. It shall be noted, however, that without an external field available, SP-STM cannot determine the absolute direction of $\vec{m}_s$; two mirror-symmetric solutions are always possible. A detailed analysis of the domain walls in Fig. 5.24 reveals the presence of few 120° domain walls (white ellipses) and one 180° domain wall (black ellipse). The spin structure of the different domain walls and the dependence of the domain wall width on the rotation angle is analyzed in the following paragraphs.

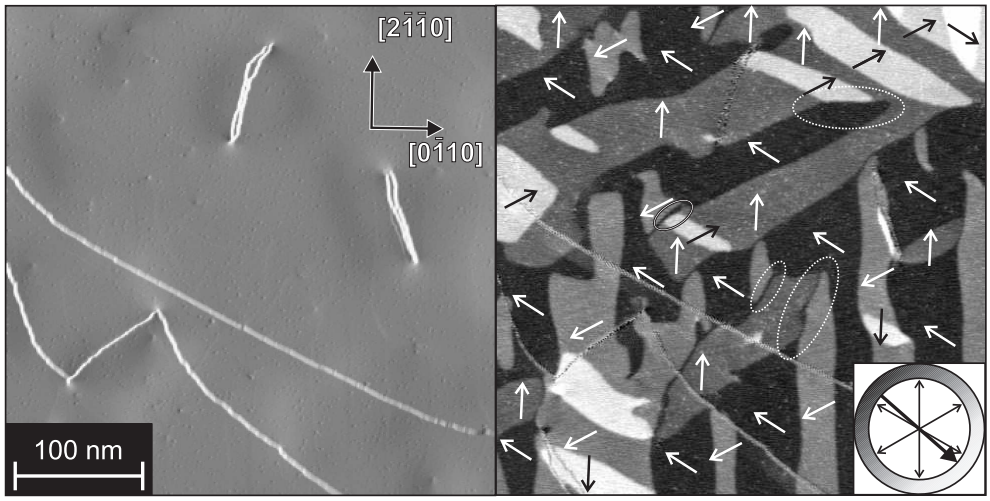

Figure 5.24: STM topograph (left panel) and magnetic $\mathrm{d}I/\mathrm{d}U$ map (right) of a 90 ML Dy/W(110) film ($T = 25$ K, tunneling parameters: $U = -1.0$ V and $I = 21$ nA). The solution for $\vec{m}_s$ with easy axes along the $\langle 2\bar{1}\bar{1}0 \rangle$ is represented with arrows.

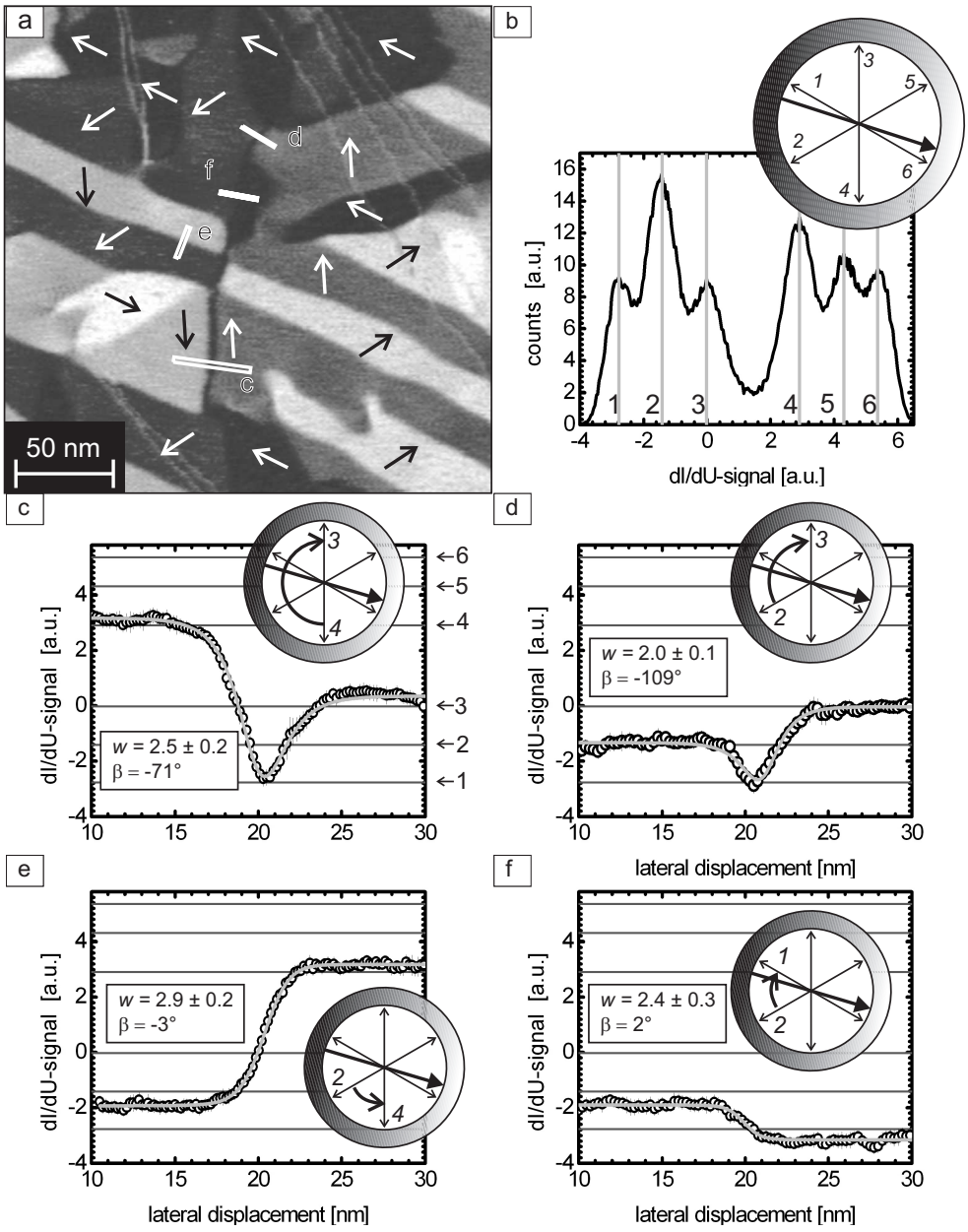

Figure 5.25: Domain wall profile analysis of a 90 ML Dy/W(110) film. (a) Magnetic dI/dU-map. The direction of $\vec{m}_{\mathrm{s}}$ for the domains is indicated by arrows. (b) dI/dU-signal intensity histogram of (a). (c-f) Line profile and schematic representation of magnetic path for the domain walls labelled with **c-f** in (a). The gray lines represent the fit of the domain-wall profiles. (T = 59 K, Dy-coated tip, tunneling parameters: $U = -0.6$ V and $I = 30$ nA).

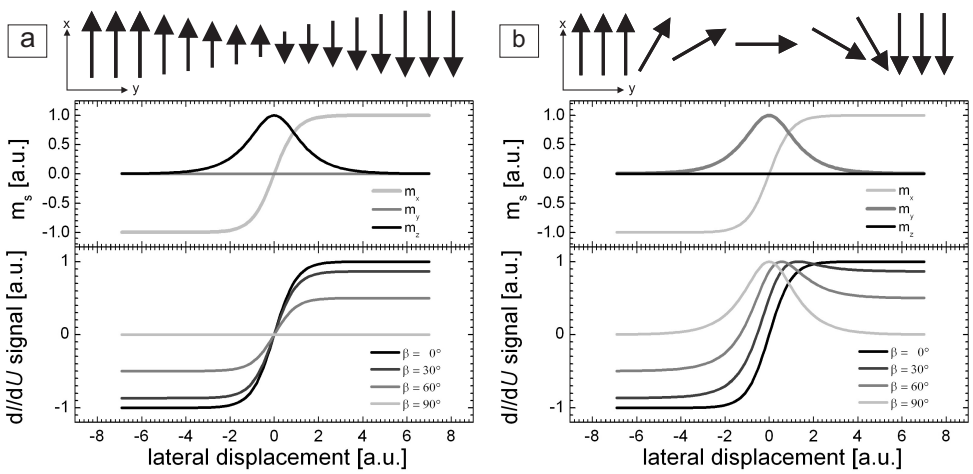

Figure 5.26: Model of 180° domain wall profiles taken with an in-plane sensitive tip where $\vec{m}_\mathrm{t}$ forms an angle β with the x-direction. (a) Model of the $\vec{m}_\mathrm{s}$ projected onto the surface x-y plane (top panel) for a Bloch domain wall with a simple profile, $\vec{m}_\mathrm{s}$ projection (middle), and the magnetic $\mathrm{d}I/\mathrm{d}U$ profile (bottom) on the basis of Eq. 2.14 (b) Model of the $\vec{m}_\mathrm{s}$ projected onto the surface x-y plane (top panel) for a Néel domain wall with a simple profile, $\vec{m}_\mathrm{s}$ projection (middle), and the magnetic $\mathrm{d}I/\mathrm{d}U$ profile (bottom).

Fig. 5.25 presents a study of the internal spin-structure of domain walls in a 90 ML Dy/W(110) surface. Fig. 5.25 (a) shows the domain structure of a 90 ML Dy/W(110) film. The $\mathrm{d}I/\mathrm{d}U$-signal intensity histogram of Fig. 5.25 (a) is shown in Fig. 5.25 (b). Fig. 5.25 (c)-(f) shows line profiles of the magnetic $\mathrm{d}I/\mathrm{d}U$-signal across a 180° domain wall, a 120° domain wall, and two different 60° domain walls labelled with **c-f** in Fig. 5.25 (a), respectively. The horizontal lines in the domain wall profiles represent the contrast levels from the histogram in Fig. 5.25 (b). Fig. 5.26 displays the $\mathrm{d}I/\mathrm{d}U$-signal calculated for a 180° domain wall on the basis of Eq. 2.14. ϕ and β are the polar and azimuthal angles of $\vec{m}_\mathrm{t}$ with respect to the surface normal and $\vec{m}_\mathrm{s}$ of the domain with highest $\mathrm{d}I/\mathrm{d}U$-signal, respectively. Two classes of 180° domain walls are proposed; Bloch domain walls [see Fig. 5.26 (a)] with $\vec{m}_\mathrm{s}$ perpendicular to the domain wall plane, and Néel domain walls [see Fig. 5.26 (b)] where $\vec{m}_\mathrm{s}$ rotates in the domain wall plane. In both cases a simple domain wall profile is assumed. In the case of a perfectly in-plane tip (ϕ=0), the domain wall profile for a Bloch domain wall maintains its general shape while the amplitude varies with β. In contrast, for a Néel domain wall in the collinear case, $\beta = 0°$, the profile is point-symmetric while for $0° < \beta < 90°$ the profile is asymmetric. Within a 180° Néel domain wall, $\vec{m}_\mathrm{s}$ is at some point collinear with $\vec{m}_\mathrm{t}$ resulting in the possible maximum $\mathrm{d}I/\mathrm{d}U$-

signal. We can assume that the experimental $\vec{m}_{\mathrm{t}}$ is almost perfectly in-plane ($\phi \approx 0$) because a large in-plane contrast is observed [see $\mathrm{d}I/\mathrm{d}U$-signal histogram in Fig. 5.25 (b)]. Therefore, comparison of the experimental domain profiles in Fig. 5.25 (c)-(f) with the calculated domain profiles in Fig. 5.26 reveals the Néel-character of the domain walls at the Dy/W(110) surface. It is well known that domain walls in ferromagnetic bulk materials prefer the Bloch type domain wall because this avoids an internal stray field in the domain wall [124]. At the surface, however, the magnetization of a Bloch wall would produce a magnetic stray field. Therefore the Bloch walls of a ferromagnetic sample are usually capped with a Néel-type structure [125, 126]. Furthermore, this surface effect favors Néel domain walls in thin films. Additionally, the large uniaxial anisotropy along the c-axis in Dy (see Sec. 5.2) may favor the formation of bulk Néel domain walls. Since the 120° and 180° domain wall profiles exhibit only one point of inflection, it is possible to conclude that the magnetoelastic energy dominates over the magnetocrystalline anisotropy energy at the surface (page 228 in Ref. [124]). Otherwise, large angle domain walls would decompose into several successive 60° domain walls. Néel domain walls result in two possible paths for the magnetization inside the domain wall, i.e. $\vec{m}_{\mathrm{s}}$ in the domain wall can rotate clockwise or anticlockwise. The energy of these two paths is different for 60° and 120° domain walls resulting in domain walls that always run along the shortest path. In the case of 180° domain walls these two paths are energetically degenerate. The path of the magnetization inside the domain walls is schematically represented in the insets in Fig. 5.25 (c)-(f). While Eq. 5.6 dictates that 120° domain walls always run along $\langle 0\bar{1}10\rangle$ directions, no preferential orientation is obtained for 180° domain walls. In our experience, 180° domain walls run along the close-packed directions.

We can ask further how the rotation angle affects the domain wall width in different domain walls. There is no analytical expression for the profile in Néel domain walls (page 244 in Ref. [124]), hence, to study the domain wall widths systematically the measured profiles were fitted to the standard Bloch domain wall profile (page 219 in Ref. [124]). Although this profile was introduced for 180° Bloch domain walls in bulk uniaxial ferromagnets where magnetostriction can be neglected, it has been successfully used for fitting the domain wall profile in Néel like domain walls in Ref. [127]. The analytical expression for the standard Bloch domain wall profile is

$$y(x) = y_0 + y_{\mathrm{sp}} \cdot \cos(\arccos[\tanh((x - x_0)/(w/2))] + \beta)\,, \tag{5.7}$$

where $y(x)$ is the magnetic $\mathrm{d}I/\mathrm{d}U$-signal measured at position x, x_0 is the position of the domain wall, w the domain wall width, and y_0 and y_{sp} are the non–spin-

polarized and spin-polarized parts of the $\mathrm{d}I/\mathrm{d}U$-signal. Although this is not the correct profile for the domain walls at the Dy/W(110) surface, a relatively good fit and a good approximation of the domain wall width can be obtained. The domain wall widths amount to 2.6 ± 0.2 nm, 2.0 ± 0.2 nm, and 2.5 ± 0.2 nm for 60°, 120°, and 180° domain walls respectively. Usually, the exchange stiffness and the magnetocrystalline anisotropy govern the domain wall width, resulting in larger widths for increasing rotation angle. However, in our system the width does not scale with the rotation angle. As already mentioned, magnetostriction is large in Dy. From the magnetostriction point of view all the domain walls analyzed are elastically compatible with respect to the wall plane, i.e. the free deformation of the two domains do not differ in any of their components tangential to the walls (page 222 in Ref. [124]). The compatibility condition leads to stresses confined within the wall resulting in an additional contribution to the domain wall energy. This magnetostrictive contribution to the domain wall energy increases with increasing rotation angle. The competition between exchange which favors wider domain walls for increasing rotation angle and magnetostriction causes the observed behavior of the domain wall width. The angle β obtained by fitting of the 180° and 120° domain walls corresponds to $\alpha = 11 \pm 1°$ which is in good agreement with $\alpha = 12 \pm 4°$ calculated from the $\mathrm{d}I/\mathrm{d}U$-signal histogram in Fig. 5.25 (b) using Eq. 5.3. This further supports the Néel character of the domain walls.

The calculation of a precise domain wall profile for our system is not simple since: (i) in rare earth metals one must consider more than nearest-neighbor exchange, since the exchange interaction is relatively long-range and generally oscillatory, (ii) the magnetoelastic contribution should be considered, and (iii) the presence of the surface is relevant. Therefore, even with a precise model of the spin structure, the extraction of material parameters from domain wall profiles is not satisfactory due to the large number of interactions that should be taken into account. There are a few theoretical studies of the spin configuration of domain walls in rare earths, especially relevant for our study is the one of Egami and Graham [128]. They calculated the spin structure for a 180° domain wall in bulk ferromagnetic dysprosium oriented parallel to the (0001) plane, that means perpendicular to our domain wall. Their calculation considers the exchange interaction up to the fourth nearest-neighbor and $H_\mathrm{k} = K_2 \cdot P_2(\cos\theta) + K_6^6 \cdot \sin^6\theta \cdot \cos 6\phi$ for the anisotropy energy (see Eq. 5.1). A very sharp Néel-like domain wall with a thickness of $t \simeq 2$ nm was obtained.

5.5.3 Correlation of structural and magnetic properties

The analysis of the Dy/W(110) film morphology (see Sec. 5.3) reveals the presence of two types of growth-induced defects, namely screw dislocations and misfit dislocations. In this section, the interplay between these defects and the film domain structure is studied.

Fig. 5.27 shows a comparison of positions of the screw dislocations (white circles) and misfit dislocations (black circles) with the magnetic structure in films with a nominal coverage of: (a) 14 ML, (b) 90 ML, and (c) 450 ML. For the ease of comparison between topographic and magnetic images the position markers of the defects which were identified in the topographs (left panels) have been copied to the magnetic images (right panels). As already mentioned, in very thin films (a) a large amount of misfit dislocations are present. The misfit dislocations coincide with pinning points for the domain walls. In contrast, the grain boundaries have little effect on the magnetic structure. Obviously, the large misfit dislocation density dominates the domain structure of thin films leading to an irregular domain structure. In films with an intermediate thickness (b) the number of misfit dislocations is approximately one order of magnitude lower. Nevertheless, the comparison of their positions and the magnetic structure reveals that they act still as pinning centers. The effect of screw dislocations in the magnetic structure is similar. An example of a thick film is shown in Fig. 5.27 (c). The misfit dislocations are preferentially located at the positions of smooth step edges. Probably the misfit dislocations nucleate at the positions where the crystal structure in already disordered. Furthermore, the misfit dislocation density is approximately three times lower than in the film shown in Fig. 5.27 (b). The energy associated to a dislocation is proportional to its line length, therefore, the energy of the misfit dislocation rises with increasing film thickness. Probably, in thick films other relaxation mechanisms are preferred over the formation of misfit dislocations. Here again, the comparison of the positions of screw and misfit dislocations with the magnetic structure reveals that they act as pinning centers.

In order to investigate the pinning strength we applied field pulses by means of the Helmholtz pair which is capable of producing a field up to $\vec{B} = 0.12$ T. Minor changes in the domain structure are found only in relatively thick films ($\Theta \geq$ 90 ML in Fig. 5.21). The magnetic domain structure of thin films ($\Theta = 27$ ML), however, remained unaffected even after the application of several hundreds of field pulses thereby indicating strong pinning. Both experiments were performed at $T = 60$ K.

This strong interaction between line defects and domain walls is not surprising for Dy. The large magnetoelastic energy of Dy results in a strong coupling between

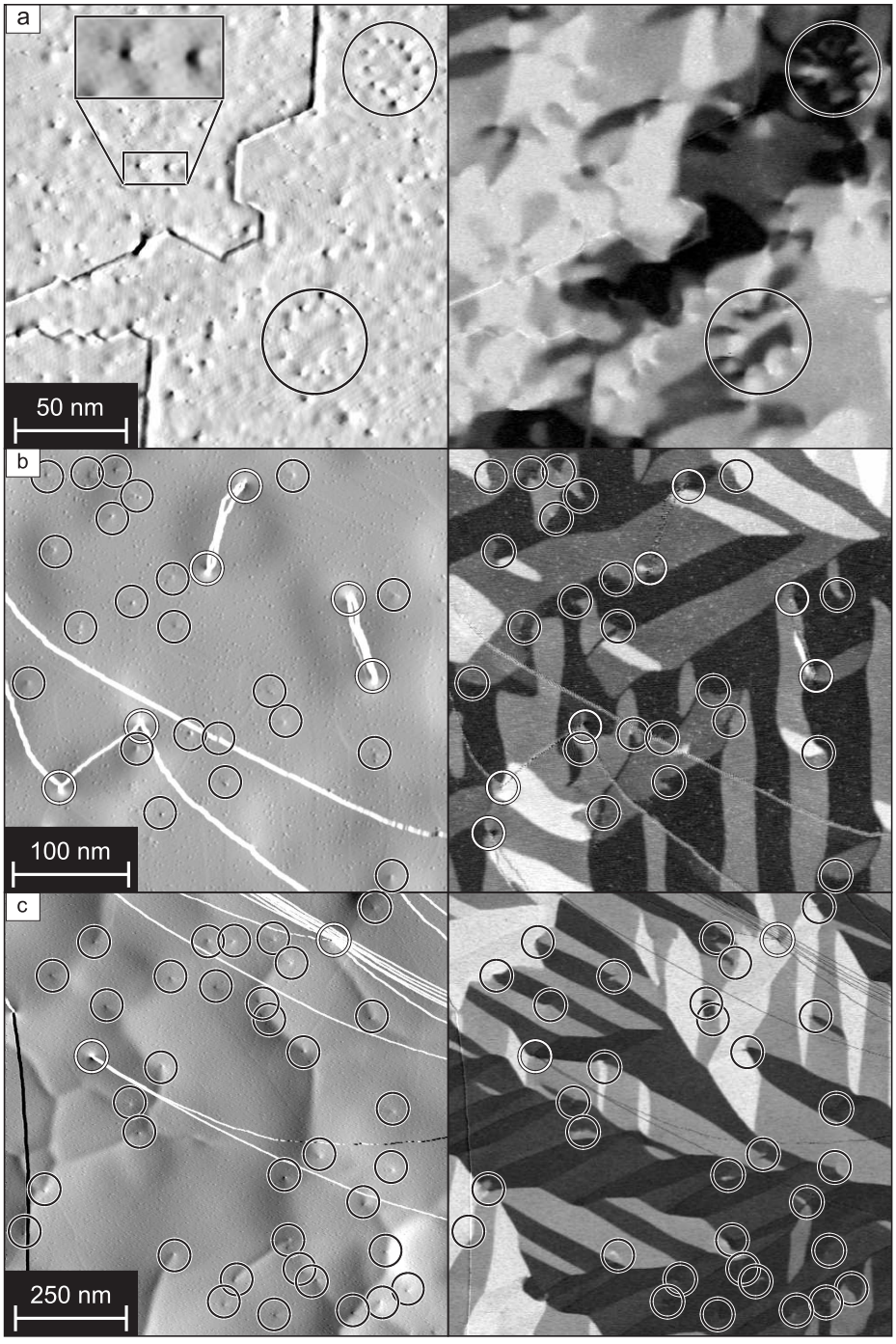

Figure 5.27: Interplay between growth-induced dislocations, i.e. screw dislocations (white circles) and misfit dislocations (black circles), and the magnetic structure of Dy/W(110) films with a thickness of: (a) 14 ML, (b) 90 ML, and (c) 450 ML.

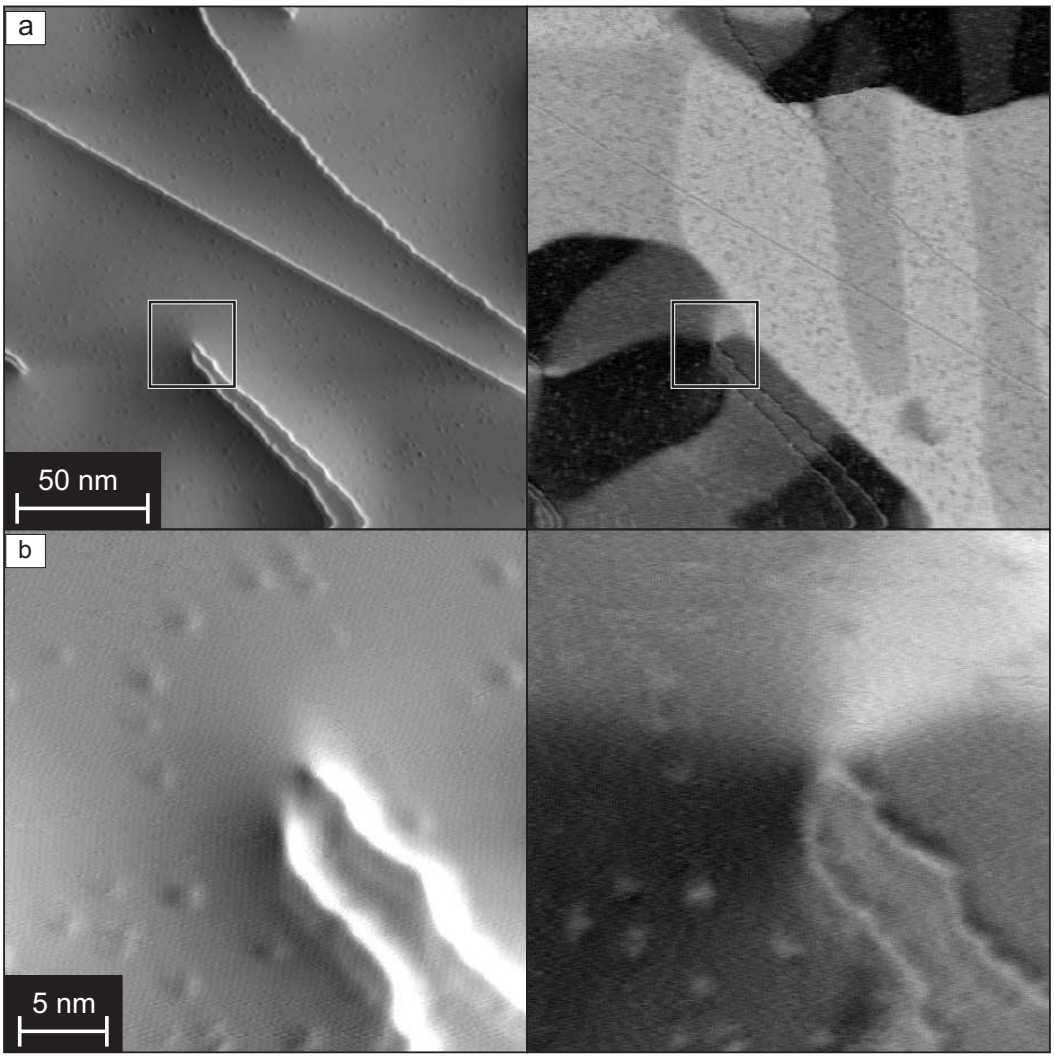

Figure 5.28: (a) STM topograph (left panel) and spin-resolved dI/dU-map (right) of a 90 ML Dy/W(110) film. The box shows the position of a screw dislocation. (b) STM topograph (left panel) and spin-resolved dI/dU-map (right) at the position of the screw dislocation($T = 60$ K, tunneling parameters: $U = -0.60$ V and $I = 30$ nA).

the magnetic structure and the stress fields of the dislocations.

Making use of the high lateral resolution of SP-STM we have studied the magnetic structure around pinning centers at dislocations. Both at screw dislocations (see Fig. 5.28) and misfit dislocations (see Fig. 5.29), two oppositely arranged bright and dark lobes which are separated by regions with intermediate contrast are present. Thereby, this magnetic structure resembles the vortex core found in iron islands (Sec. 4.2.2). Fig. 5.29 shows a detailed study of the domain

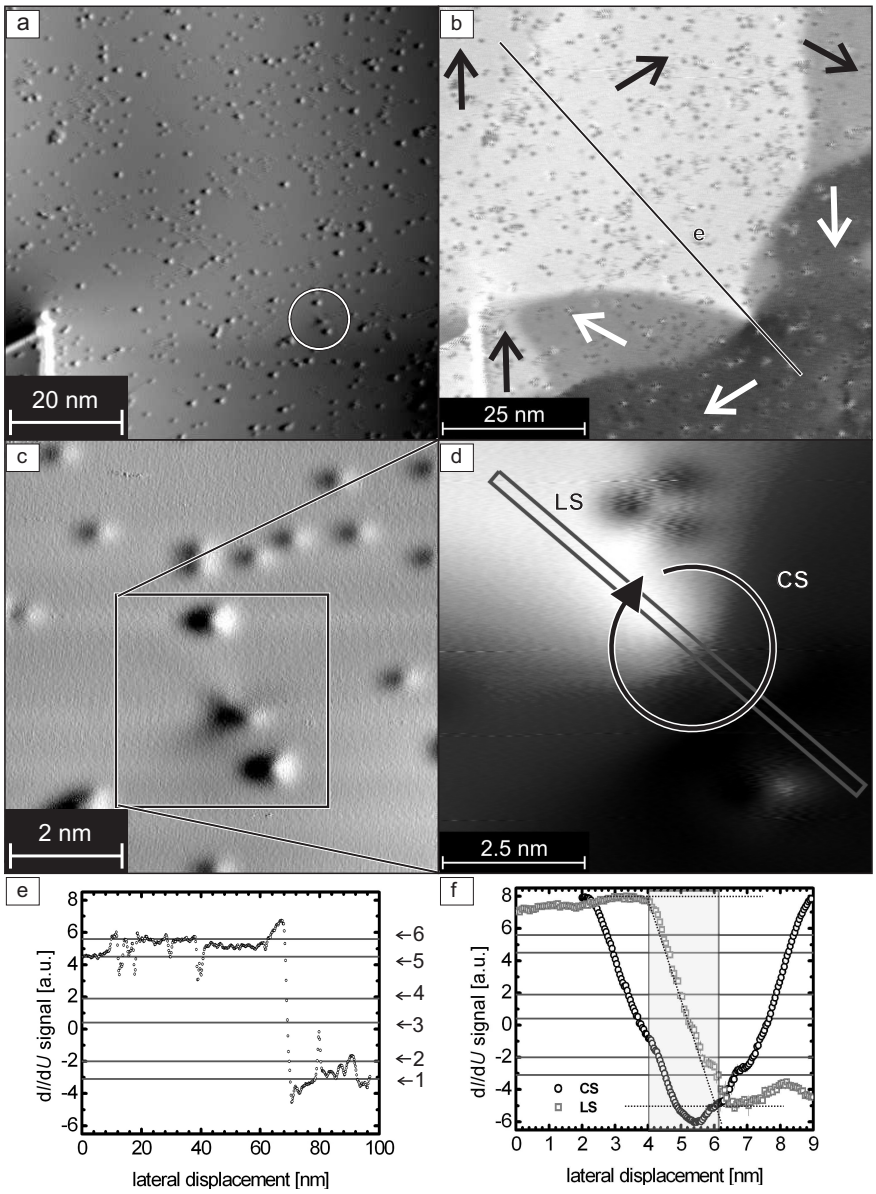

Figure 5.29: STM topograph (a) and spin-resolved dI/dU-map (b) of a 90 ML Dy/W(110) film. At the position of a misfit edge dislocation, marked with a white circle in (a), five different domains are pinned. (c) Higher magnification STM. (d) Magnetic dI/dU-map of the area around the dislocation core. (e) Profile of the magnetic dI/dU signal along the line marked with an **e** in (b) that crosses the core of the magnetic vortex. (f) Profiles of the magnetic dI/dU signal along **LS** and **CS** in (d). ($T = 58$ K, tunneling parameters: $U = -0.9$ V and $I = 30$ nA).

structure around a misfit dislocation where five different domains are pinned. A magnetic $\mathrm{d}I/\mathrm{d}U$ profile across the dislocation core [line **e** in Fig. 5.29 (b)] reveals that $\vec{m}_\mathrm{s}$ rotates abruptly through 180° at the position of the dislocation. Furthermore, a circular profile of the magnetic $\mathrm{d}I/\mathrm{d}U$-signal around the dislocation core [**CS** in Fig. 5.29 (d)] shows that $\vec{m}_\mathrm{s}$ curls continuously and homogenously. Therefore, it is possible to conclude that a vortex-like magnetic structure is located at the dislocation core. However, the presence of an out-of-plane component of $\vec{m}_\mathrm{s}$ at the dislocation position is still to be confirmed by the use of an out-of-plane sensitive SP-STM tip. Nevertheless, the origin of the magnetic vortices should be different to that of the vortex in iron islands (Sec. 4.2.2). In the case of iron islands, $\vec{m}_\mathrm{s}$ rotates around the center of the island to minimize the dipolar energy. At the center of the island, a topological discontinuity of $\vec{m}_\mathrm{s}$ arises which is solved by the generation of a vortex. At pinning centers of Dy/W(110) films, the dipolar energy does not play an important role. The vortex core diameter is only $d = 2.0 \pm 0.5$ nm [see profile **LS** in Fig. 5.28 (f)], significantly smaller to those found in Fe islands, $d = 10 \pm 3$ nm. A further analysis of the magnetic $\mathrm{d}I/\mathrm{d}U$ profile **e** in Fig. 5.29 (b) reveals a large increase by about 50% in the amplitude of the magnetic $\mathrm{d}I/\mathrm{d}U$-signal at about 20 nm around the dislocation. We can analyze this increase of the $\mathrm{d}I/\mathrm{d}U$-signal as a result of a non-collinear $\vec{m}_\mathrm{t}$, i.e., $0° < \alpha < 30°$. On the basis of Eq. 5.3, α is $20 \pm 4°$. Since $\vec{m}_\mathrm{s}$ curls continuously around the vortex core, at some position should be collinear with $\vec{m}_\mathrm{t}$. This will result in an increase of the magnetic $\mathrm{d}I/\mathrm{d}U$-signal amplitude by 6% on the basis of Eq. 2.14. A non-collinear $\vec{m}_\mathrm{t}$ fails to explain the observed amplitude increase of 50%. This anomalous increase in the amplitude of the magnetic $\mathrm{d}I/\mathrm{d}U$-signal indicates a change of the electronic structure and/or polarization around the position of the dislocation.

In Fig. 5.29, the presence of a vortex-like magnetic structure around a misfit dislocation coincides with the point where five different domains meet. We can ask if the magnetic structure is caused by the pinning of several domains. Fig. 5.30 shows the magnetic structure of a 90 ML Dy/W(110) film. The high magnification inset in Fig. 5.30 (left panel) reveals the presence of a misfit dislocation. An analysis of the domain structure at this position reveals no domain wall pinning. Only a vortex-like structure is present inside a domain more than 15 nm away from the closest domain wall [inset in Fig. 5.30 (right panel)]. In conclusion, the data indicate that the vortex like domain structures are not necessarily bound to domain walls. Instead, they may also exist at misfit dislocations in otherwise uniform domains.

We propose two possible mechanisms that would lead to the vortex-like struc-

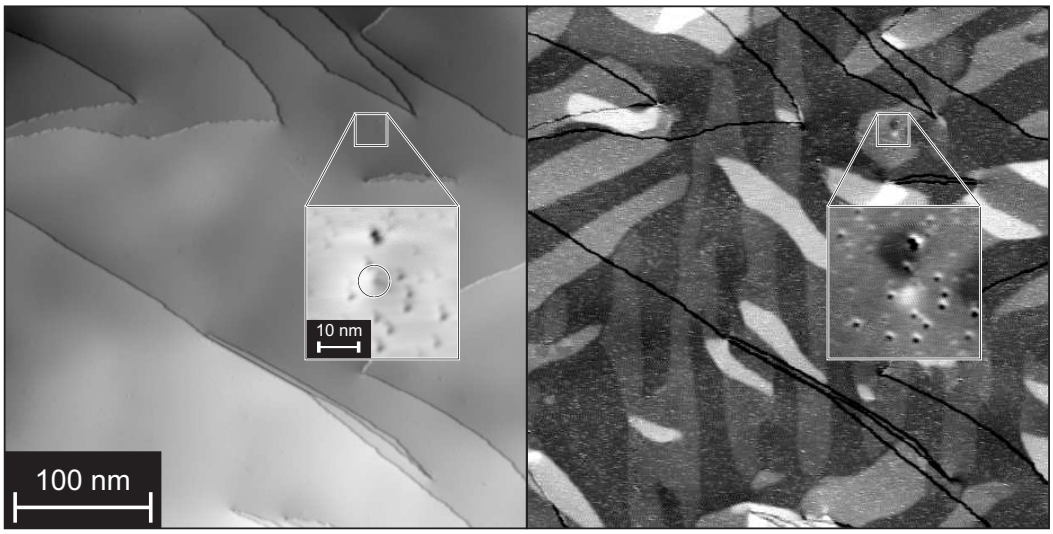

Figure 5.30: STM topograph (left panel) and spin-resolved dI/dU-map (right) of a 90 ML Dy/W(110) film. The inset in the topography shows the position of a misfit dislocation. The inset in the magnetic dI/dU-map reveals the formation of a magnetic vortex inside a domain ($T = 60$ K, tunneling parameters: $U = -0.45$ V and $I = 23$ nA)

ture, namely, a local dislocation-induced reorientation transition or a frozen helimagnetic phase. First, since the crystallographic structure around the dislocation lines is distorted, a local defect-induced anisotropy different from that of the perfect crystal exits at the dislocation position. This local anisotropy might produce a strong uniaxial anisotropy along the c-axis at dislocation core position [96] that produces the vortex-like magnetic structure. Second, dI/dU-maps taken with non-magnetic (see Fig. 5.16) and magnetic (see Fig. 5.29) tips indicate that the local electronic properties at the position of the dislocations are different. This change in the electronic structure might cause localized areas of a helimagnetic phase even below T_{C} resulting in the vortex-like magnetic structure.

5.5.4 Unstable magnetic structures

The three magnetic dI/dU maps in Fig. 5.31 were taken successively on the same area. A 180° domain wall appears in Fig. 5.31 (a) where the internal contrast changes within the wall (inset). Furthermore, analysis of the magnetization around the 120° domain wall, marked with a circle, reveals that the condition in equation Eq. 5.6 is not fulfilled. Therefore, the 120° domain wall is not magnetically compensated. Fig. 5.31 (b) shows a closer view of the area that was taken

after Fig. 5.31 (a). Comparing the position of the 180° domain wall in both dI/dU maps, it is possible to conclude that the domain wall has moved by about 20 nm.

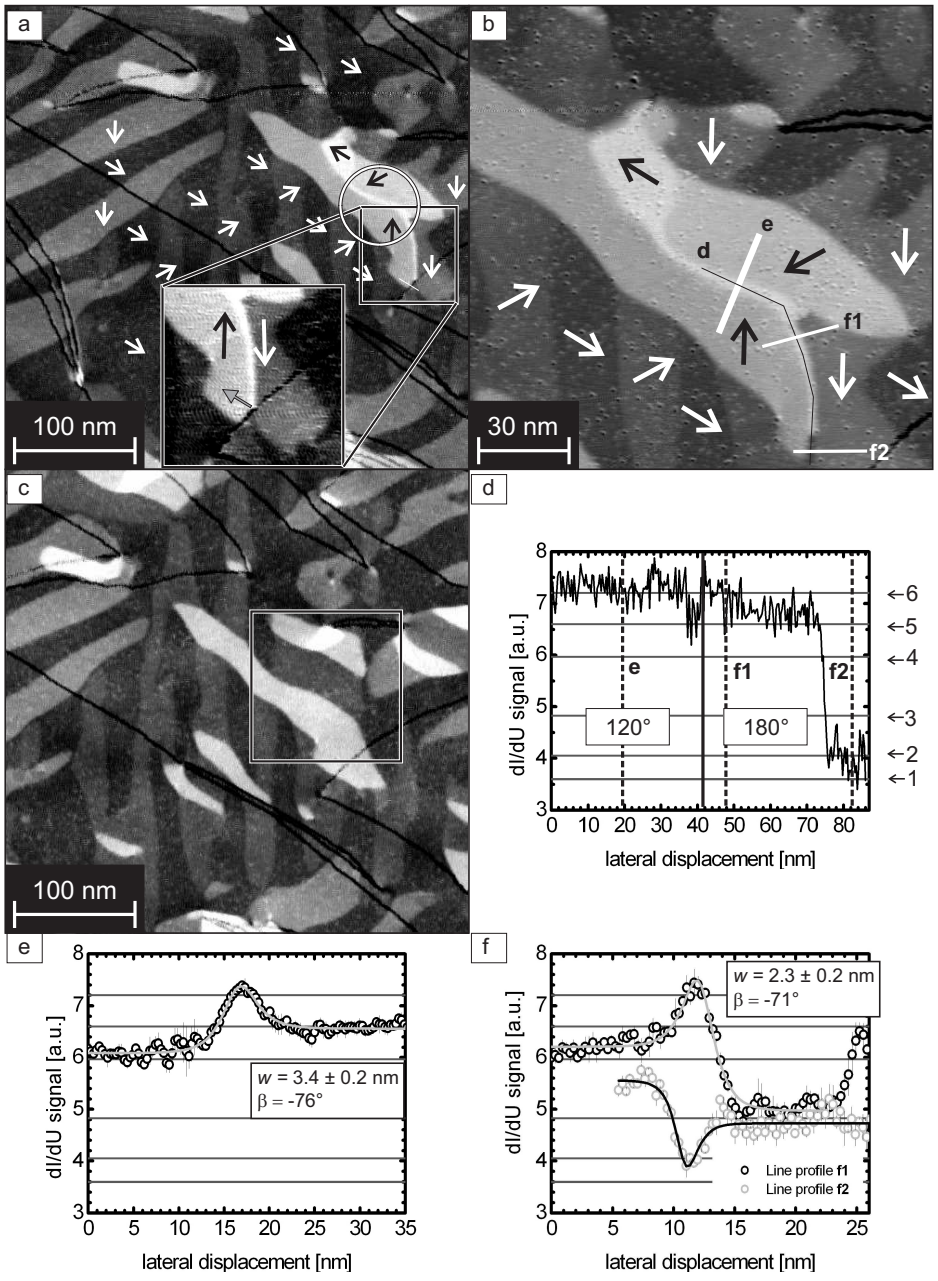

Figure 5.31: (a)-(c) Magnetic dI/dU maps of a 90 ML Dy/W(110) film measured successively. The magnetic structure of the area change after each scan. (d) Line profile along the **d**. Line profile across a (e) 120° and (f) 180° domain walls.

The gray arrow in the inset in Fig. 5.31 (a) displays the displacement of the domain wall. Fig. 5.31 (c) shows an overview of the area taken after Fig. 5.31 (b). The area imaged in (b) (square) has spontaneously and dramatically changed. Obviously, the magnetic structure of this area is unstable.

As mentioned above, in 180° domain walls the two possible paths of $\vec{m}_s$ are energetically degenerate. Occasionally, these two paths are present within the same 180° domain wall. Exactly this situation is observed in the domain wall in Fig. 5.31 (a) (inset), where $\vec{m}_s$ in the upper and the lower segments rotate in the opposite sense. These two domain wall segments meet in a line perpendicular to the surface, a so-called Bloch line (page 258 in Ref. [124]). Bloch lines in Néel walls have a magnetic structure similar to that of a vortex, where $\vec{m}_s$ curls around the core of the Bloch line. Therefore, the presence of a Bloch line and a magnetically uncompensated domain wall results in an unstable area that can dramatically change its magnetic structure, probably under the influence of the stray field produced by the Dy-coated tip.

A magnetic $\mathrm{d}I/\mathrm{d}U$ profile along the 180° and 120° domain walls [**e** in Fig. 5.31 (b)] is shown in Fig. 5.31 (d). The horizontal lines represent the contrast levels of the $\mathrm{d}I/\mathrm{d}U$-signal in Fig. 5.25 (a). The profile reveals that the width of the Bloch line amounts to 3 ± 1 nm. The domain wall profile of the non-magnetically compensated 120° domain wall is shown in Fig. 5.31 (e). The profile is fitted with the model in Eq. 5.7. The domain wall width obtained, $w = 3.4 \pm 0.2$ nm, is much larger than that of magnetically compensated 120° domain walls (see Fig. 5.25). In contrast, w for the 180° [Fig. 5.31 (f)] domain wall is in good agrement with the value in Fig. 5.25.

5.5.5 Bias-dependent contrast with Dy-coated probe tips

Occasionally, it is observed that the SP-STM magnetic contrast of magnetically coated SP-STM tips can change from in-plane to out-of-plane depending on the bias voltage. A mechanism based on intra-atomic non-collinear magnetism was proposed to explain this phenomenon [129]. There, the magnetic contrast is not explained as a function of a $\vec{m}_t$ which direction does not depend on the bias voltage as assumed in Ref. [21], but as a result of the bias-dependent tunneling through electronic orbitals with different quantization axes. This mechanism may also explain voltage-dependent contrast given by some Dy-coated tips. For example, Fig. 5.32 shows two magnetic $\mathrm{d}I/\mathrm{d}U$-maps of a Dy/W(110) film that were measured in the forward (a) and backward (b) channels with different tunneling parameter. If we assume an bias independent direction of $\vec{m}_t$, on the basis of

Eq. 5.3, the direction of $\vec{m}_t$ for both images can be calculated from dI/dU-signal intensity histogram (bottom panels). The result is schematically represented in the insets. The calculated $\vec{m}_t$ for each dI/dU-maps differ by $54\pm12^\circ$ in the surface plane. Since the magnetic dI/dU-maps were measured simultaneously a periodic and reversible change of $\vec{m}_t$ can be excluded. Therefore, this apparent rotation of $\vec{m}_t$ might be explained by the voltage-dependent tunneling where the energetic dependence of both spin channels in tip and sample should be taken into account. Unfortunately, there is not a complete data set where magnetic dI/dU maps were measured for a larger range of bias voltages.

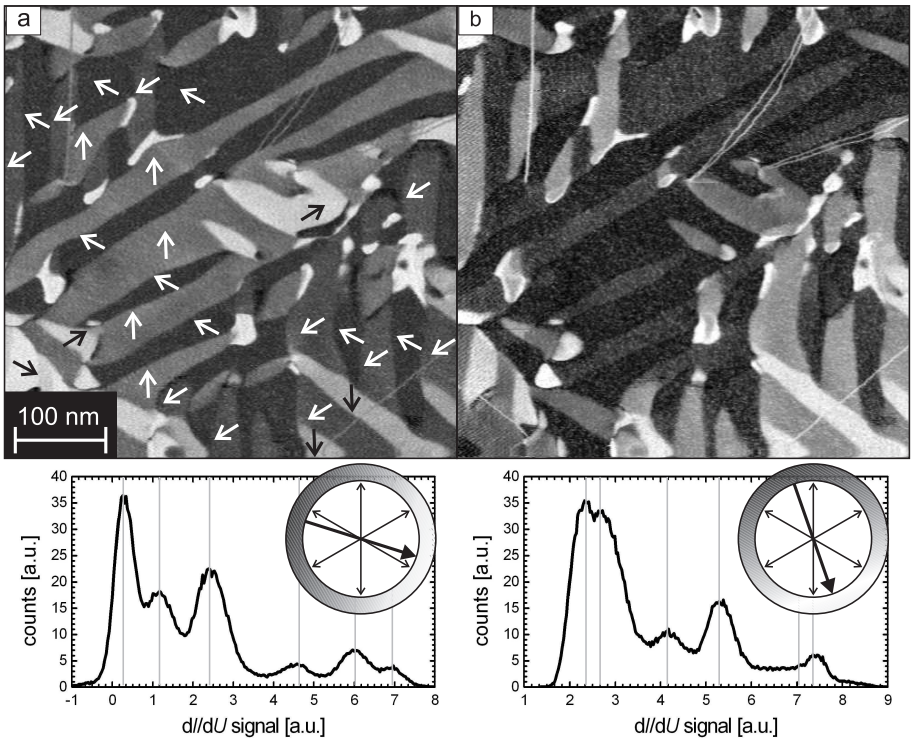

Figure 5.32: Magnetic dI/dU-maps of a 90 ML Dy/W(110) film taken with a Dy-coated tip in the (a) forward channel ($U = -1.0$ V and $I = 45$ nA) and (b) backward channel ($U = -0.45$ V and $I = 23$ nA).

5.6 Comparison with magnetic depth profile analysis

Epitaxially grown Dy/W(110) films have intensively been studied by resonant soft x-ray scattering in Refs. [122, 123]. The use of different photon energies allows the mapping of the magnetic profile of the films upon cooling through the first-order phase transition from the ferromagnetic to the helimagnetic phase.

This transition has a hysteretic and discontinuous character in bulk samples. In contrast, the authors find a gradual ferromagnetic to helimagnetic transition in Dy/W(110) films. Fig. 5.33 shows the depth profile analysis of a $\Theta = 180$ ML film. This film was prepared in two steps; (i) first $\Theta = 20$ ML was evaporated at 0.5 ML/min and annealed at $T = 670$ K and (ii) then the rest of the material was evaporated at 2 ML/min and annealed at $T = 800$ K. According to the authors, this two-step procedure results in a better crystallinity and less grain boundaries than a one-step process. Upon cooling below $T_N \approx 179$ K the entire

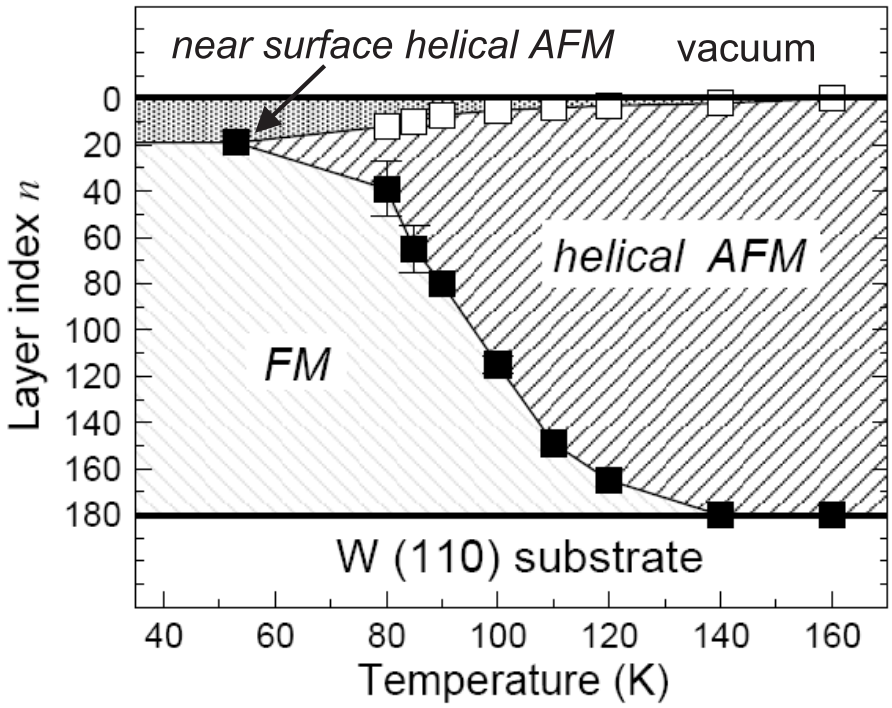

Figure 5.33: Magnetic depth profile of a 180 ML Dy/W(110) film during the first-order phase transition from the ferromagnetic to the helimagnetic phase. Data from Ref. [123]

sample becomes helimagnetically ordered. Below $T \approx 125$ K a second near-surface helimagnetic phase (cross-hatched area) appears. The near-surface helimagnetic phase is characterized by a smaller turn angle than the bulk helimagnetic phase. The helimagnetic angle is about 19° at $T \approx 125$ K and decreases with decreasing temperature. This phase was detected also in the top-most 20 layers below T_{C}. The normal helimagnetic phase survives in between the near-surface helimagnetic phase and the ferromagnetic phase down to about 50 K.

The SP-STM data presented in this work clearly show that at the surface the film is ferromagnetically ordered in the temperature range between 60 K [see Fig. 5.22 (f)] and 25 K [see Fig. 5.22 (e)]. Furthermore, the increase of the domain

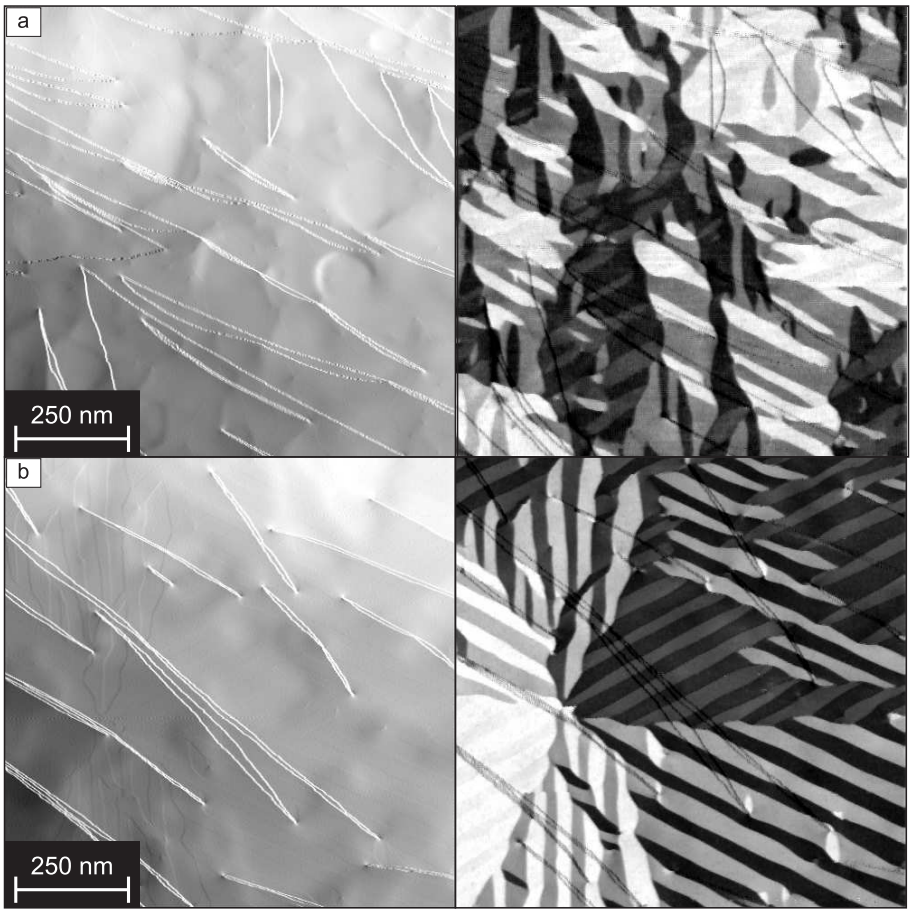

Figure 5.34: (a) STM topograph (left panel) and magnetic $\mathrm{d}I/\mathrm{d}U$ map (right) of a 180 ML Dy/W(110) film grown by following the preparation method in Sec. 5.3. (b) STM topograph (left panel) and magnetic $\mathrm{d}I/\mathrm{d}U$ map (right) of a 180 ML Dy/W(110) film grown by following the preparation method in Ref. [122, 123].

size with increasing film thickness indicates that the ferromagnetic structure at the surface depends on the total film thickness.

One possible cause for this apparent discrepancy is the different preparation procedure that may affect the magnetic structure. We have prepared 180 ML Dy/W(110) films following the preparation method in Sec. 5.3 [Fig. 5.34 (a)] and in Refs. [122, 123] [Fig. 5.34 (b)]. The preparation procedure leads to a better film quality, i.e. fewer misfit and screw dislocations, however, no drastic change of the magnetic structure at the surface is observed. Another possible origin is the different degree of surface sensitivity of the techniques. While SP-STM probes the magnetic properties of the top-most layer, the depth resolution of resonant soft x-ray scattering integrates over about 20 layers. The presence of several ferromagnetically coupled layers at the surface is, however, not incompatible with the results of the depth profile analysis. A feasible model of the film magnetic depth profile below T_C would be several ferromagnetic Dy layers at the surface. Below this ferromagnetic surface phase several layers of the near-surface helimagnetic phase might be present. This model would be compatible with both SP-STM and resonant soft x-ray scattering data.

Holmium (Ho) also exhibits a helimagnetic structure. It has been shown that in Ho(0001)/W(110) films the neighboring basal planes in the surface region of the film have a tendency towards ferromagnetic alignment [130]. This effect is related to the nature of the helimagnetic phase that originates from the long-range and oscillatory character of the RKKY interaction. The reduced number of neighboring planes, and the different electronic structure of the surface may result in a ferromagnetic alignment at the surface in the case of Ho/W(110) as well as of Dy/W(110) films.

Chapter 6

Summary and Outlook

In this thesis spin-polarized tunneling through an adsorbate layer for sulfur-covered Fe(110) and the magnetic properties of Dy/W(110) films have been studied by spin-polarized scanning tunneling microscopy (SP-STM).

It has been demonstrated that the characteristic magnetic vortex structure of three–dimensional Fe islands on W(110) is observable by SP-STM after sulfur adsorption, even though the electronic structure of the surface is modified. We have confirmed that saturation with H_2S leads to an adsorbed c(3×1) sulfur monoatomic layer. Although we found that this sulfur layer does not passivate Fe(110), the use of an appropriate adsorbate as a passivation layer may be a pathway to extend SP-STM to operation under ambient conditions.

Some fundamental questions concerning the structural and magnetic properties of ferromagnetic Dy films grown on W(110) have been answered. Thickness-dependent measurements reveal that perfect screw dislocations with $\vec{b} = [0001]$ which are typical in rare earth metal (REM) films on W(110) are caused by two equivalent stackings of the REM second layer on top of the slightly distorted hexagonal first atomic layer. These perfect screw dislocations appear at a thickness $\Theta > 18$ ML. Furthermore, ensembles of point-like defects are identified by means of atomically resolved STM as edge dislocations with $\vec{b} = \frac{1}{3}\langle 2\bar{1}\bar{1}0\rangle$. The misfit between the first atomic layer and the film is the origin of these dislocations. The density of the misfit-induced dislocations decreases rather fast with increasing film thickness.

The thickness-dependent domain structure of the Dy/W(110) films between 14 ML and 450 ML at $T \leq 60$ K has been studied. The measurements show that the surface is ferromagnetically coupled. The surface presents a six-fold magnetic symmetry with bulk-like easy axes, i.e. $\langle 2\bar{1}\bar{1}0\rangle$. With increasing film thickness the domain size grows and the complexity of the domain structure decreases. Fur-

thermore, the domain wall profiles unveil the Néel-like character of the domain walls at the surface. The domain walls are found to be very narrow, around 2 nm. A high resolution SP-STM study of the domain structure reveals that the two kinds of line defects, i.e. screw dislocations and misfit edge dislocations, are very strong pinning centers for the domain walls. Moreover, the complex domain structure in very thin films results from the large density of pinning centers at misfit dislocations. The magnetic structure around the dislocations resembles that of a magnetic vortex. Further experimental work with out-of-plane sensitive magnetic tips is necessary to reveal the possible presence of an out-of-plane magnetization at the defect position, similar to the centers of magnetic vortex cores.

Bibliography

[1] *Hard drive disk milestones*, Hitachi Global Storage Technologies www.hitachigst.com.

[2] M. Bode and R. Wiesendanger, *Magnetic Microscopy of Nanostructures* (Springer Verlag, Berlin, 2004), p. 203.

[3] W. Wulfhekel, *Magnetic Microscopy of Nanostructures* (Springer Verlag, Berlin, 2004), p. 181.

[4] M. Kläui, C. A. F. Vaz, J. Rothman, J. A. C. Bland, W. Wernsdorfer, G. Faini, and E. Cambril, Phys. Rev. Lett. **90**, 097202 (2003).

[5] M. Liebmann, A. Schwarz, U. Kaiser, R. Wiesendanger, D.-W. Kim, and T.-W. Noh, Phys. Rev. B. **71**, 104431 (2005).

[6] T. Uhlig, M. Rahm, C. Dietrich, R. Höllinger, M. Heumann, D. Weiss, and J. Zweck, Phys. Rev. Lett. **95**, 237205 (2005).

[7] C. Nistor, E. Faraggi, and J. L. Erskine, Phys. Rev. B. **72**, 014404 (2005).

[8] A. Wachowiak, J. Wiebe, M. Bode, O. Pietzsch, M. Morgenstern, and R. Wiesendanger, Science **298**, 577 (2002).

[9] G. Binnig and H. Rohrer, Helv. Phys. Acta **55**, 726 (1982).

[10] G. Binnig, H. Rohrer, C. Gerber, and E. Weibel, Phys. Rev. Lett. **49**, 57 (1982).

[11] G. Binnig, H. Rohrer, C. Gerber, and E. Weibel, Phys. Rev. Lett. **50**, 120 (1983).

[12] G. Binnig and H. Rohrer, Rev. Mod. Phys. **59**, 615 (1987).

[13] R. Wiesendanger, *Scanning Probe Microscopy and Spectroscopy: Methods and Applications* (Cambridge University Press, 1994).

[14] M. Bode, Rep. Progr. Phys. **66**, 523 (2003).

[15] J. Bardeen, Phys. Rev. Lett. **6**, 57 (1961).

[16] J. Tersoff and D. R. Hamann, Phys. Rev. Lett. **50**, 1998 (1983).

[17] J. Tersoff and D. R. Hamann, Phys. Rev. B. **31**, 805 (1985).

[18] J. Li, W.-D. Schneider, and R. Berndt, Phys. Rev. B. **56**, 7656 (1997).

[19] J. C. Slonczewski, Phys. Rev. B. **39**, 6995 (1989).

[20] T. Miyazaki and N. Tezuka, J. Magn. Magn. Mat. **6**, 1847 (1995).

[21] D. Wortmann, S. Heinze, P. Kurz, G. Bihlmayer, and S. Blügel, Phys. Rev. Lett. **86**, 004132 (2001).

[22] H. Lüth, *Surfaces and interfaces of solid materials* (Spriger-Verlag, Berlin, 2001).

[23] Omicron Nano Technology GmbH D-65232 Taunusstein (1995).

[24] M. Getzlaff, Ph.D. thesis, University of Bielefeld (1993).

[25] Pfeiffer Vacuum GmbH D-35613 Asslar (1995).

[26] *EG-Sicherheitsdatenblatt gemäß Richtlinie 91/155/EWG: Schwefelwasserstoff*, GHC Handels GmbH D-22761 Hamburg (2004).

[27] *SPECTRALEED Optics and electron gun. Users´s guide.*, Omicron Nano Technology GmbH D - 65232 Taunusstein (1995).

[28] M. Henzler and W. Göpel, *Oberflächenphysik des Festkörpers* (Teubner Studienbücher, Suttgart, 1994).

[29] C. Witt, M. Bode, and R. Wiesendanger, Appl. Phys. A **63**, 303 (1996).

[30] T. Hänke, Ph.D. thesis, University of Hamburg (2005).

[31] *Variable temperature UHV STM 25 K to 1500 K*, Omicron Nano Technology GmbH D - 65232 Taunusstein (1995).

[32] O. Pietzsch, A. Kubetzka, D. Haude, M. Bode, and R. Wiesendanger, Rev. Sci. Instr. **71**, 424 (2000).

[33] S. H. Pan, *Piezo-electric motor*, International Patent Publication Number WO 93/19494, International Bureau, World Intellectual Property Organization (1993).

[34] CryoVac gmbH D-53842 Troisdorf (delivered in 1998).

[35] M. Bode, R. Pascal, and R. Wiesendanger, Surf. Sci. **344**, 185 (1995).

[36] J. Wiebe, A. Wachowiak, F. Meier, D. Haude, T. Foster, M. Morgenstern, and R. Wiesendanger, Rev. Sci. Inst. **75**, 4871 (2004).

[37] C. J. Chen, *Introduction to scanning tunneling microscopy* (Oxford University Press, New York, 1993).

[38] A. Kubetzka, M. Bode, O. Pietzsch, and R. Wiesendanger, Phys. Rev. Lett. **88**, 057201 (2002).

[39] T. K. Yamada, M. M. J. Bischoff, T. Mizoguchi, and H. van Kempen, Appl. Phys. Lett. **82**, 1437 (2006).

[40] B. Marchon, P. Bernhardt, M. E. Bussell, G. A. Somorjai, M. Salmeron, and W. Siekhaus, Phys. Rev. Lett. **60**, 1166 (1988).

[41] B. Marchon, D. F. Ogletree, M. E. Bussell, G. A. Somorjai, M. Salmeron, and W. Siekhaus, J. Micr. **152**, 427 (1989).

[42] B. Marchon, D. F. Ogletree, M. Salmeron, and W. Siekhaus, J. Vac. Sci. Techn. A **6**, 531 (1988).

[43] O. Pietzsch, A. Kubetzka, M. Bode, and R. Wiesendanger, Phys. Rev. Lett. **84**, 5212 (2000).

[44] A. Kubetzka, O. Pietzsch, M. Bode, and R. Wiesendanger, Phys. Rev. B **63**, 140407 (2001).

[45] E. Y. Vedmedenko, A. Kubetzka, K. von Bergmann, O. Pietzsch, M. Bode, J. Kirschner, H. P. Oepen, and R. Wiesendanger, Phys. Rev. B **92**, 077207 (2004).

[46] M. Bode, A. Wachowiak, J. Wiebe, A. Kubetzka, M. Morgenstern, and R. Wiesendanger, Appl. Phys. Lett. **84**, 948 (2004).

[47] H. J. Elmers, J. Hauschild, U. Gradmann, H. Bethge, D. Heuer, and U. Köhler, PRL **73**, 898 (1996).

[48] H. J. Elmers, J. Hauschild, and U. Gradmann, Phys. Rev. B **59**, 3688 (1999).

[49] H. Bethge, D. Heuer, C. Jensen, K. Reshöft, and U. Köhler, Surf. Scie. **331**, 878 (1995).

[50] A. Wachowiak, Ph.D. thesis, University of Hamburg (2003).

[51] G. Yi, P. R. Aitchison, W. D. Doyle, J. N. Chapman, and C. D. W. Wilkinson, J. Appl. Phys. **92**, 6087 (2002).

[52] K. J. Kirk, S. McVitie, J. N. Chapman, and C. D. W. Wilkinson, J. Appl. Phys. **89**, 7174 (2001).

[53] R. D. Gomez, T. V. Luu, A. O. Pak, K. J. Kirk, and C. D. W. Wilkinson, J. Appl. Phys. **85**, 6163 (1999).

[54] M. Herrmann, S. McVitie, and C. D. W. Wilkinson, J. Appl. Phys. **87**, 2994 (2000).

[55] S. Evoy, D. W. Carr, L. Sekaric, Y. Suzuki, J. M. Parpia, and H. G. Craighead, J. Appl. Phys. **87**, 404 (2000).

[56] U. Gradmann, G. Liu, H. J. Elmers, and M. Przybylski, Hyper Interact. **57**, 1845 (1990).

[57] E. Feldtkeller and H. Thomas, Phys. kondens. Materie **4**, 8 (1965).

[58] T. Shinjo, T. Okuno, R. Hassdorf, K. Shigeto, and T. Ono, Science **289**, 930 (2000).

[59] M. Pratzer, H. J. Elmers, M. Bode, O. Pietzsch, A. Kubetzka, and R. Wiesendanger, Phys. Rev. Lett. **87**, 127201 (2001).

[60] Y. Taga, A. Isogai, and K. Nakajima, Trans. Jap. Inst. Met. **17**, 201 (1976).

[61] S. R. Kelemen and A. Kaldor, J. Chem. Phys. **75**, 1530 (1981).

[62] J. Weissenrieder, M. Gothelid, G. L. Lay, and U. O. Karlsson, Surf. Sci. **515**, 135 (2002).

[63] J. Oudar, Bull. Soc. Fr. Mineral. Cristallogr. **94**, 225 (1971).

[64] H. D. Shih, F. Jona, D. W. Jepsen, and P. M. Marcus, Phys. Rev. Lett. **46**, 731 (1981).

[65] M. J. S. Spencer, A. Hung, I. K. Snook, and I. Yarovsky, Surf. Sci. **540**, 420 (2003).

[66] C. Kittel, *Introduction to Solid State Physics* (John Wiley and Sons, New York, 2005).

[67] M. Albrecht, T. Furubayashi, U. Gradmann, and W. A. Harrison, J. Magn. Magn. Mater. **104-107**, 1699 (1992).

[68] M. Albrecht, U. Gradmann, T. Furubayashi, and W. A. Harrison, Europhys. Lett. **20**, 65 (1992).

[69] M. J. Spencer, I. K. Snook, and I. Yarovsky, J. Phys. Chem. B **109**, 9604 (2006).

[70] K. Hermann and M. A. V. Hove, *Leedpat version 2.0*, http://w3.rz-berlin.mpg.de/ hermann/ssdin5/ (2002).

[71] A. J. Pignocco and G. E. Pellissier, Surf. Sci. **7**, 261 (1967).

[72] F. Portele, Z. Naturforschung **24a**, 1268 (1969).

[73] A. G. Naumovets and A. G. Fedorus, Sov. Phys. JETP **41**, 587 (1976).

[74] M. A. V. Hove, W. H. Weinberg, and C.-M. Chan, *Low-Energy Electron Diffraction* (Springer Verlag, Berlin, 1986).

[75] M. J. Spencer, I. K. Snook, and I. Yarovsky, J. Phys. Chem. B **110**, 956 (2006).

[76] H.-J. Kim, E. Vescovo, S. Heinze, and S. Blügel, Surf. Sci. **478**, 193 (2001).

[77] A. F. Holleman and E. Wiberg, *Lehrbuch der Anorganischen Chemie* (Walter de Gruyter, Berlin, 1995).

[78] Y. S. Dedkov, U. Rüdiger, and G. Güntherodt, Phys. Rev. B **65**, 064417 (2002).

[79] J. Jensen and A. R. Mackintosh, *Rare earth Magnetism. Structure and excitations* (Clarendon press, Oxford, 1991).

[80] R. M. White, Science **229**, 11 (1985).

[81] K. H. J. Buschow, Rep. Prog. Phys. **54**, 1123 (1991).

[82] M. Fähnle, K. Hummler, M. Liebs, and T. Beuerle, Appl. Phys. A **57**, 67 (1993).

[83] M. A. Ruderman and C. Kittel, Phys. Rev. **96**, 99 (1954).

[84] T. Kasuya, Prog. Theoret. Phys. (Japan) **16**, 45 (1956).

[85] K. Yosida, Phys. Rev. **106**, 893 (1957).

[86] R. Harris and G. V. Raynor, J. Less-Common. Metals **17**, 336 (1969).

[87] M. K. Wilkindon, W. C. Koehler, E. O. Wollan, and J. W. Cable, J. Appl. Phys. **32**, 48S (1961).

[88] D. R. Behrendt, S. Legvold, and F. H. Spedding, Phys. Rev. **109**, 1544 (1958).

[89] W. H. Koehler, J. Appl. Phys. **36**, 1078 (1965).

[90] S. Legvold, J. Alstad, and J. Rhyne, Phys. Rev. Lett. **10**, 509 (1963).

[91] F. J. Darnell, Phys. Rev. **132**, 128 (1963).

[92] F. J. Darnell, Phys. Rev. **130**, 1825 (1963).

[93] E. Callen and H. B. Callen, J. Phys. Chem. Solids **27**, 1271 (1966).

[94] J. J. Rhyne and A. E. Clark, J. Appl. Phys. **38**, 1379 (1967).

[95] J. L. Feron, Ph.D. thesis, Grenoble (1969).

[96] H. Kronmüller, Conf. on Magn. and Magn. Materials AIP Conf. Proc. **10**, 1006 (1973).

[97] P. B. Fynbo, J. Phys. **F7**, 1349 (1977).

[98] L. Néel, C. R.Acad. Sci. Paris. **237**, 1468 (1953).

[99] S. C. Wu, H. Li, Y. S. Li, D. Tian, J. Quinn, F. Jona, and D. Fort, Phys. Rev. B **44**, 13720 (1991).

[100] J. Quinn, Y. S. Li, F. Jona, and D. Fort, Phys. Rev. B **46**, 9694 (1992).

[101] J. Kolaczkiewicz and E. Bauer, Surf. Sci. **175**, 487 (1986).

[102] H. Li, D. Tian, J. Quinn, Y. S. Li, S. C. Wu, and F. Jona, Phys. Rev. B **45**, 3853 (1992).

[103] J. H. van der Merwe, Philos. Mag. A **45**, 127 (1982).

[104] J. H. van der Merwe, Philos. Mag. A **45**, 145 (1982).

[105] J. H. van der Merwe, Philos. Mag. A **45**, 159 (1982).

[106] J. H. van der Merwe, Appli. Surf. Sci. **22/23**, 545 (1985).

[107] E. D. Tober, R. X. Ynzunza, C. Westphal, and C. S. Fadley, Phys. Rev. B **53**, 5444 (1996).

[108] D. Weller and S. F. Alvarado, J. Appl. Phys. **59**, 2908 (1986).

[109] E. Grier, Ph.D. thesis, University of Oxford (2000).

[110] G. Bihlmayer (2005), private comunication.

[111] P. Kurz, G. Bihlmayer, and S. Blügel, J. Phys. Condens. Matter **14**, 6353 (2002).

[112] C. Schüßler-Langeheine, Ph.D. thesis, Freie Universität Berlin (1999).

[113] E. Weschke, C. Schüssler-Langeheine, R. Meier, A. V. Fedorov, K. Starke, F. Hübinger, and G. Kaindl, Phys. Rev. Lett. **77**, 3415 (1996).

[114] M. Bode, M. Getzlaff, and R. Wiesendanger, Phys. Rev. Lett. **81**, 4256 (1998).

[115] A. Bauer, D. Wegner, and G. Kaindl, cond-mat p. 0502581 (2005).

[116] C. Schüßler-Langeheine, E. Weschke, C. Mazumdar, R. Meier, A. Y. Grigoriev, G. Kaindl1, C. Sutter, G. G. D. Abernathy, and M. Richter, Phys. Rev. Lett. **84**, 5624 (2000).

[117] C. Schüßler-Langeheine, E. Weschke, H. Ott, , A. Y. Grigoriev, A. Möllera, R. Meier, C. Mazumdar, and G. Kaindl, J. Elec. Spect. Relat. Phenom. **114-116**, 795 (2001).

[118] M. Bode, M. Getzlaff, A. Kubetzka, R. Pascal, O. Pietzsch, and R. Wiesendanger, Phys. Rev. Lett **83**, 3017 (1999).

[119] H. G. V. Bueren, *Imperfections in crystals* (North-Holland Publishing Company, 1960).

[120] V. A. Ukraintsev, Phys. Rev. B **53**, 11176 (1996).

[121] D. E. Johnson, J. R. Johnson, and J. L. Hilburn, *Electric circuit analysis* (Prentice Hall, Englewood Cliffs, NJ, 1989).

[122] H. Ott, Ph.D. thesis, Freie Universität Berlin (2004).

[123] H. Ott, C. Schüßler-Langeheine, E. S. G. Kaindl, and E. Weschke, submited to Appl. Phys. Lett. (2005).

[124] A. Hubert and R. Schäfer, *Magnetic domains. The analysis of magnetic microstructures* (Springer Verlag, Berlin, 2000).

[125] H. P. Oepen and J. Kirschner, Phys. Rev. Lett. **62**, 819 (1989).

[126] M. R. Scheinfein, J. Unguris, R. J. Celotta, and D. T. Pierce, Phys. Rev. Lett. **63**, 668 (1989).

[127] R. Ravlić, M. Bode, A. Kubetzka, and R. Wiesendanger, Phys. Rev. B. **67**, 174411 (2003).

[128] T. Egami and C. D. Graham, J. Appl. Phys. **42**, 1299 (1971).

[129] M. Bode, O. Pietzsch, A. Kubetzka, S. Heinze, and R. Wiesendanger, Phys. Rev. Lett. **86**, 2142 (2001).

[130] E. Weschke, H. Ott, E. Schierle, C. Schüßler-Langeheine, D. V. Vyalikh, G. Kaindl, V. Leiner, M. Ay, T. Schmitte, H. Zabel, et al., Phys. Rev. Lett. **93**, 157204 (2004).

Publications

- S. Krause, L. Berbil-Bautista, T. Hänke, F. Vonau, M. Bode, and R. Wiesendanger: *Consequences of Atomic-Scale Defects on the Magnetic Structure of High Anisotropy Films: Pinning Centers on Dy/W(110)*, submitted to Phys. Rev. Lett.

- L. Berbil-Bautista, S. Krause, T. Hänke, M. Bode, and R. Wiesendanger: *Spin-plorazied scanning tunneling microscopy through an adsorbate layer: sulfur covered Fe/W(110)*, Surf. Sci. Lett. **600**, L20 (2006).

- T. Hänke, M. Bode, S. Krause, L. Berbil-Bautista, and R. Wiesendanger: *Temperature-dependent scanning tunneling spectroscopy of Cr(001): orbital Kondo resonance versus surface state*, Phys. Rev. B **72**, 085453 (2005).

- T. Hänke, S. Krause, L. Berbil-Bautista, M. Bode, R. Wiesendanger, V. Wagner, D. Lott, and A. Schreyer: *Absence of spin-flip transition at the Cr(001) surface: A combined spin-polarized scanning tunneling microscopy and neutron scattering study*, Phys. Rev. B **71**, 184407 (2005).

- L. Berbil-Bautista, T. Hänke, M. Getzlaff, R. Wiesendanger, I. Opahle, K. Koepernik, and M. Richter: *Observation of 5f states in U/W (110) films by means of scanning tunneling spectroscopy*, Phys. Rev. B **70**, 113401 (2004).

- M. Hupalo, V. Yeh, L. Berbil-Bautista, S. Kremmer, E. Abram, and M. C. Tringides: *Uniform-height island growth of Pb on Si(111)-Pb($\sqrt{3} \times \sqrt{3}$) at low temperatures*, Phys. Rev. B **64**, 155307 (2001).

- M. Hupalo, S. Kremmer, V. Yeh, L. Berbil-Bautista, E. Abram, and M. C. Tringides: *Uniform island height selection in the low temperature growth of Pb/Si(1 1 1)-(*7×7*)*, Surf. Sci. **493**, 526 (2001).

- V. Yeh, L. Berbil-Bautista, C. Z. Wang, K. M. Ho, and M. C. Tringides: *Role of the Metal/Semiconductor Interface in Quantum Size Effects: Pb/Si(111)*, Phys. Rev. Lett. **85**, 5158 (2000).

Conferences

- L. Berbil-Bautista, S. Krause, M. Bode, and R. Wiesendanger: *Thickness-dependent domain structure of ferromagnetic Dy(0001)/W(110) studied by spin-polarized STM*, Frühjahrstagung der Deutschen Physikalischen Gesellschaft, Dresden, Germany, 2006 (talk).

- S. Krause, L. Berbil-Bautista, M. Bode, and R. Wiesendanger: *Thermal switching behaviour of superparamagnetic nanoislands: SP-STM on Fe/W(110)*, Frühjahrstagung der Deutschen Physikalischen Gesellschaft, Dresden, Germany, 2006 (talk).

- L. Berbil-Bautista, S. Krause, M. Bode, and R. Wiesendanger: *Ferromagnetic Domains in Dy(0001) Films on W(110) Studied by Means of Spin-Polarized-STM*, 13^{th} International Conference on Scanning Tunneling Microscopy, Sapporo, Japan, 2005 (talk).

- S. Krause, L. Berbil-Bautista, M. Bode, and R. Wiesendanger: *Spin-Polarized STM Through an Adsorbate Layer: Sulfur-Covered Fe/W(110)*, 13^{th} International Conference on Scanning Tunneling Microscopy, Sapporo, Japan, 2005 (talk).

- L. Berbil-Bautista, S. Krause, T. Hänke, M. Bode, and R. Wiesendanger: *Growth and electronic properties of thick films and pyramidal islands of Dy/W(110) studied by STM/STS*, Frühjahrstagung der Deutschen Physikalischen Gesellschaft, Berlin, Germany, 2005 (talk).

- S. Krause, L. Berbil-Bautista, T. Hänke, M. Bode, and R. Wiesendanger: *Spinpolarisierte Rastertunnelmikroskopie auf S-bedeckten Fe-Inseln*, Frühjahrstagung der Deutschen Physikalischen Gesellschaft, Berlin, Germany, 2005 (talk).

- L. Berbil-Bautista, T. Hänke, M. Getzlaff, I. Opahle, M. Richter, and R. Wiesendanger: *Observation of 5f-states on U/W(110) films by means*

of STS, 12^{th} International Conference on Scanning Tunneling Microscopy, Eindhoven, Netherlands, 2003 (talk).

- M. Getzlaff, T. Hänke, L. Berbil-Bautista, and R. Wiesendanger: *Uranium thin films: structural and electronic properties*, Frühjahrstagung der Deutschen Physikalischen Gesellschaft, Dresden, Germany, 2003 (talk).

- L. Berbil-Bautista, T. Hänke, M. Getzlaff, I. Opahle, M. Richter, and R. Wiesendanger: *Observation of 5f-states on U/W(110) films by means of STS*, Frühjahrstagung der Deutschen Physikalischen Gesellschaft, Dresden, Germany, 2003 (talk).

- S. Kremmer, E. Abram, L. Berbil-Bautista, V. Yeh, K. Budde, M. C. Tringides: *Height selection in self-organized structures observed during the growth of Pb/Si(111) at low temperature*, American Physical Society march meeting, Minneapolis, 2000 (talk).

- V. Yeh, S. Kremmer, E. Abram, L. Berbil-Bautista, K. Budde, M. C. Tringides: *Comparison of the different kinetic pathways to form the self-organized structure of 7-step Pb(111) islands on Si(111) at low temperature*, American Physical Society march meeting, Minneapolis, 2000 (talk).

Acknowledgements

It is a pleasure to thank the many people who made this thesis possible.

First of all, I would like to express my sincere thanks to Prof. R. Wiesendanger for giving me the opportunity to spend four marvellous years doing research in his group.

This thesis would have not been possible without supervision of Matthias Bode. His experience, guidance, and patience were vital to overcome the big and small difficulties that I found during my doctoral research.

I would like to express my sincere thanks to my colleagues Stefan Krause, Toben Hänke, and François Vonau. We have shared much more that long hours in our laboratory. It has been a pleasure to work with them.

I would like to thanks to Oswald Pietzsch, Kirsten von Bergmann, and André Kubetzka who were always there with useful tips and fruitful discusions.

I would like to thanks to Fiona McLay for carefully reading my manuscript and helping to bring some clarity to my English.

I would like to thank to Miren for being like she is. We began this adventure together; it had been sometimes hard but always beautiful. Thank you for constantly reminding me that "Itaca está en el camino".

I would like to thank to my siblings, Marisa, Amor, and Pedro, because family is one of the most important things in live.

Last but not the least, I would like to thank my mother, Soledad, for her unconditional love and support.

Erklärung

Hiermit erkläre ich, daß ich die vorliegende Promotionsarbeit selbständig und ohne fremde Hilfe verfaßt habe. Andere als die von mir angegebenen Quellen und Hilfsmittel sind nicht verwendet worden. Den benutzten Werken wörtlich oder inhaltlich entnommenen Stellen sind als solche kenntlich gemacht.

Hamburg, im März 2006